Real-Time 3D Surface-Shape Measurement Using Fringe Projection and System-Geometry Constraints

by

Xinran Liu

A thesis
presented to the University of Waterloo
in fulfillment of the
thesis requirement for the degree of
Doctor of Philosophy
in
Systems Design Engineering

Waterloo, Ontario, Canada, 2019

Examining Committee Membership

The following served on the Examining Committee for this thesis. The decision of the Examining Committee is by majority vote.

External Examiner	Daniel Lau Professor, Electrical and Computer Engineering University of Kentucky
Supervisor	Jonathan Kofman Associate Professor, Systems Design Engineering University of Waterloo
Internal Member	Hamid Tizhoosh Professor, Systems Design Engineering University of Waterloo
Internal-external Member	Carl Haas Professor, Civil and Environmental Engineering University of Waterloo
Internal-external Member	Zhou Wang Professor, Electrical and Computer Engineering University of Waterloo

Author's Declaration

This thesis consists of material all of which I authored or co-authored: see Statement of Contributions included in the thesis. This is a true copy of the thesis, including any required final revisions, as accepted by my examiners.

I understand that my thesis may be made electronically available to the public.

Statement of Contributions

Based on detailed literature review by Xinran Liu, and through discussions of existing 3D optical metrology techniques, research directions, and experimental techniques with supervisor Dr. Jonathan Kofman, Xinran Liu determined the specific research directions and developed the new techniques with contribution and guidance of Dr. Jonathan Kofman. Xinran Liu carried out all experiments and data analysis. Dr. Jonathan Kofman edited published work derived from this research as well as this thesis following first drafts written by Xinran Liu.

Abstract

Optical three-dimensional (3D) surface-shape measurement has diverse applications in engineering, computer vision and medical science. Fringe projection profilometry (FPP), uses a camera-projector system to permit high-accuracy full-field 3D surface-shape measurement by projecting fringe patterns onto an object surface, capturing images of the deformed patterns, and computing the 3D surface geometry. A wrapped phase map can be computed from the camera images by phase analysis techniques. Phase-unwrapping can solve the phase ambiguity of the wrapped phase map and permit determination of camera-projector correspondences. The object surface geometry can then be reconstructed by stereovision techniques after system calibration.

For real-time 3D measurement, geometry-constraint based methods may be a preferred technique over other phase-unwrapping methods, since geometry-constraint methods can handle surface discontinuities, which are problematic for spatial phase unwrapping, and they do not require additional patterns, which are needed in temporal phase unwrapping. However, the fringe patterns used in geometry-constraint based methods are usually designed with a low frequency in order to maximize the reliability of correspondence determination. Although using high-frequency fringe patterns have proven to be effective in increasing the measurement accuracy by suppressing the phase error, high-frequency fringe patterns may reduce the reliability and thus are not commonly used.

To address the limitations of current geometry-constraint based methods, a new fringe projection method for surface-shape measurement was developed using modulation of background and amplitude intensities of the fringe patterns to permit identification of the fringe order, and thus unwrap the phase, for high-frequency fringe patterns. Another method was developed with background modulation only, using four high-frequency phase-shifted fringe patterns. The pattern frequency is determined using a new fringe-wavelength geometry-constraint model that allows only two point candidates in the measurement volume. The correct corresponding point is selected with high reliability using a binary

pattern computed from the background intensity. Equations of geometry-constraint parameters permit parameter calculation prior to measurement, thus reducing computational cost during measurement. In a further development, a new real-time 3D measurement method was devised using new background-modulated modified Fourier transform profilometry (FTP) fringe patterns and geometry constraints. The new method reduced the number of fringe patterns required for 3D surface reconstruction to two. A short camera-projector baseline allows reliable corresponding-point selection, even with high-frequency fringe patterns, and a new calibration approach reduces error induced by the short baseline. Experiments demonstrated the ability of the methods to perform real-time 3D measurement for a surface with geometric discontinuity, and for spatially isolated objects.

Although multi-image FPP techniques can achieve higher accuracy than single-image methods, they suffer from motion artifacts when measuring dynamic object surfaces that are either moving or deforming. To reduce the motion-induced measurement error for multi-image FPP techniques, a new method was developed to first estimate the motion-induced phase shift errors by computing the differences between phase maps over a multiple measurement sequence. Then, a phase map with reduced motion-induced error is computed using the estimated phase shift errors. This motion-induced error compensation is computed pixel-wise for non-homogeneous surface motion. Experiments demonstrated the ability of the method to reduce motion-induced error in real-time, for real-time shape measurement of surfaces with high depth variation, and moving and deforming surfaces.

Acknowledgements

I would like to express my great appreciation to Prof. Jonathan Kofman, my research supervisor, for his professional and patient guidance and valuable support of this research work. I would also like to thank my family and my friends for their support and encouragement.

This research has been funded by the Natural Sciences and Engineering Research Council of Canada (NSERC), the University of Waterloo, and the China Scholarship Council (CSC).

Table of Contents

List of Figures

List of Tables

Chapter 1
Introduction

Optical-based non-contact three-dimensional (3D) surface-shape measurement has become increasingly important in mechanical engineering [1,2], biomedical engineering [3,4], computer vision [3–5], and entertainment [5]. A variety of optical 3D surface-shape measurement techniques and systems have been developed to meet different demands of measurement accuracy, measurement speed, spatial resolution, system size, and cost. This research focuses on high-accuracy, high-resolution (full-field), real-time 3D surface-shape measurement with off-the-shelf commercial devices, to make this technology more accessible to everyday users.

1.1 Passive 3D Surface-Shape Measurement Techniques

Passive 3D surface-shape measurement techniques do not project light onto an object surface. Depth information of an object surface is determined from two-dimensional (2D) digital images or video acquired from one or more cameras.

Monocular methods, which use one or more images from one camera for 3D construction of an object surface, analyze the effects of lighting in the formation of images to determine surface shape. Binocular stereovision obtains the 3D geometric information from images acquired by two cameras from different perspectives, where depth information is calculated based on disparity (separation distance) between two images. The 2D image acquisition for stereovision can be fast. However, correspondences between the two images at numerous pixels are required, commonly by some form of feature extraction, and this is often difficult for freeform textureless surfaces.

Although the hardware setup for passive 3D surface-shape measurement methods is usually simple, the complexity of image processing and the sensitivity to the object surface reflectivity and lighting conditions limit system performance on poorly-textured objects [6].

1.2 Laser Scanning Techniques

Laser scanning techniques use a laser light source to project a spot or stripe pattern onto the object surface, and a camera to acquire the reflected light from another direction [7]. The 3D coordinates of points on the object surface at the laser spot or stripe can be calculated by triangulation [8], based on known geometry of the optical setup, or based on a 2D laser plane to 3D space mapping determined by calibration [9]. To obtain full surface-geometry information, the laser spot or stripe must be moved across the surface, which is time-consuming and requires a scanning mechanism unless done by hand [9]. Projection of multiple stripes can speed up data acquisition, but stripe identification can be difficult when measuring objects with surface discontinuities [10], and resolution is limited to the spacing between stripes. In contrast to these methods, moiré contouring and digital fringe projection methods are full-field measuring techniques that measure 3D coordinates of the object surface at every camera pixel.

1.3 Structured Light Projection Techniques

As an advancement over passive binocular stereo vision, structured-light projection techniques replace one camera with an active light source, and project structured light onto the object surface to mitigate the main limitation of passive techniques, the difficulty in finding image correspondences for poorly-textured objects. Simpler structured-light projection techniques project a single spot, line or stripe pattern, multiple stripes, grid patterns, or speckle pattern [11].

Full-field structured-light techniques typically project continuous full-field patterns, that do not repeat themselves within some local neighborhood and have either grayscale or colour intensities at every projector pixel, and consequently, in the images captured by the camera. (Fringe projection techniques are discussed in Section 1.4.2). Projection of binary patterns (black and white stripes) can also produce continuous grayscale patterns in the camera image by either defocusing the projector [12] or by Moiré techniques, which use interference of

binary grid patterns. For all of the above methods, a set of 3D coordinates on the object surface can be computed for every camera pixel.

1.3.1 Moiré Contouring Techniques

Moiré techniques are based on the moiré effect that occurs when one periodic grid overlaps another one that has a close frequency [13]. In shadow moiré, light is projected through a grating (grid) and viewed by a camera through the same grating, thus using the interference on the object surface between the light through the grating and its projected shadow [14] (Figure 1.1a). In projection moiré, light is projected through a grating and an image is captured by viewing through a separate reference grating (Figure 1.1b). The full surface-geometry information of the object can be obtained through analysis of moiré contour patterns formed on the object surface. To increase measurement resolution, phase shifting is usually applied by translating the grating; however, this requires a complicated optical setup and translating devices.

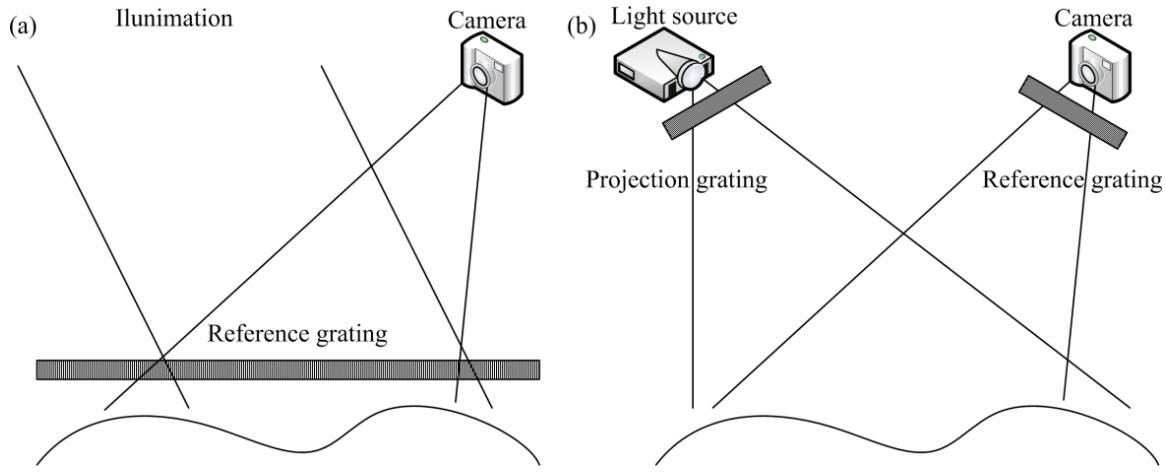

Figure 1.1. Moiré contouring techniques: (a) shadow moiré, and (b) projection moiré.

Digital moiré requires projection of only a single grid pattern and capture of only a single image without using an optical reference grating. Phase-shifted moiré patterns, which contain the grid (considered as unwanted noise), are generated in a digital post-process, and pure moiré patterns can be extracted by removing the high-frequency grid in the captured images

[15,16], also done as a post process. For objects with surface discontinuities, two-image and three-image digital moiré techniques have been developed [17]. Although the digital moiré technique is suitable for measurement of deforming surfaces, by performing the 2D image acquisition component of the measurement process in real time with surface deformation, the 3D reconstruction still requires computationally expensive post-processing, making the entire 3D reconstruction not real-time.

1.3.2 Fringe Projection Techniques

Fringe projection profilometry (FPP) uses one or more spatially-continuous fringe patterns projected onto an object surface (Figure 1.2). Typically, phase-shifted sinusoidal fringe patterns are projected, and the resulting captured images are:

$$I_n(x, y) = A(x, y) + B(x, y)\cos\left[\phi(x, y) - \theta_n\right], n = 1, 2, ..., N\ , \tag{1.1}$$

where (x, y) are the image coordinates, $I_n(x, y)$ represents the image intensity at every image pixel, for $n = 1, 2, \ldots, N$ captured images, and $A(x, y)$ and $B(x, y)$ represent the background intensity and amplitude of modulation, respectively. $\theta_n = 2\pi(n-1)/N$ is the phase shift between fringe patterns, and N is the number of projected phase-shifted patterns and thus number of captured images. The phase map $\phi(x, y)$ contains object surface height information at every pixel. A wrapped phase map can be determined by phase analysis techniques (described in more detail below), and an unwrapped phase map can be computed by phase unwrapping techniques. Then the object surface height map $h(x, y)$ can be obtained from the unwrapped phase map (Figure 1.3).

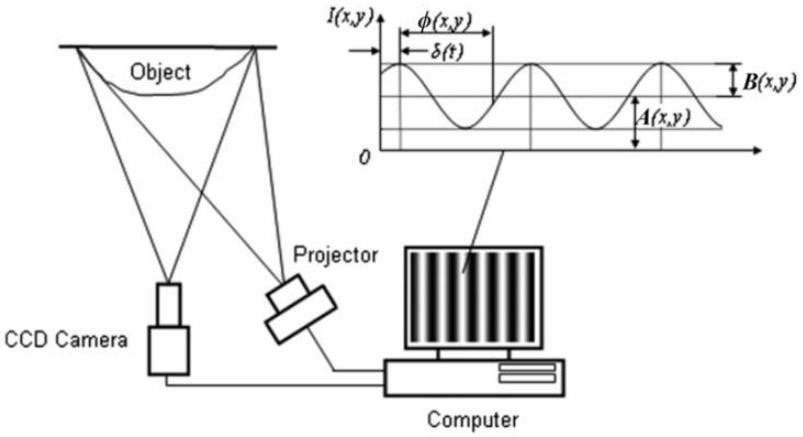

Figure 1.2. Schematic diagram of the 3D surface measurement system based on FPP [18].

Figure 1.4 shows the relation between phase $\phi(x, y)$ and height of object $h(x, y)$. d is the distance between the centres of pupils of the projector (P) and camera (E). Points P and E are assumed to be in a plane parallel and at a distance H to the reference plane. If there is no object, a ray of a fringe pattern strikes the reference plane at point A. However, for an object with height (depth) $h(x, y)$, the same ray strikes the object surface at point D, which is observed to be point C on the reference plane by the camera. Thus, the object surface height map $h(x, y)$ can be obtained by the following equation:

$$h(x, y) = \frac{\overline{AC}\left(H/d\right)}{1+\overline{AC}/d}, \tag{1.2}$$

where distance $\overline{AC}$ can be computed by the phase change between point A and C. H and d are system parameters that can be determined by system calibration (explained in Section 2.1).

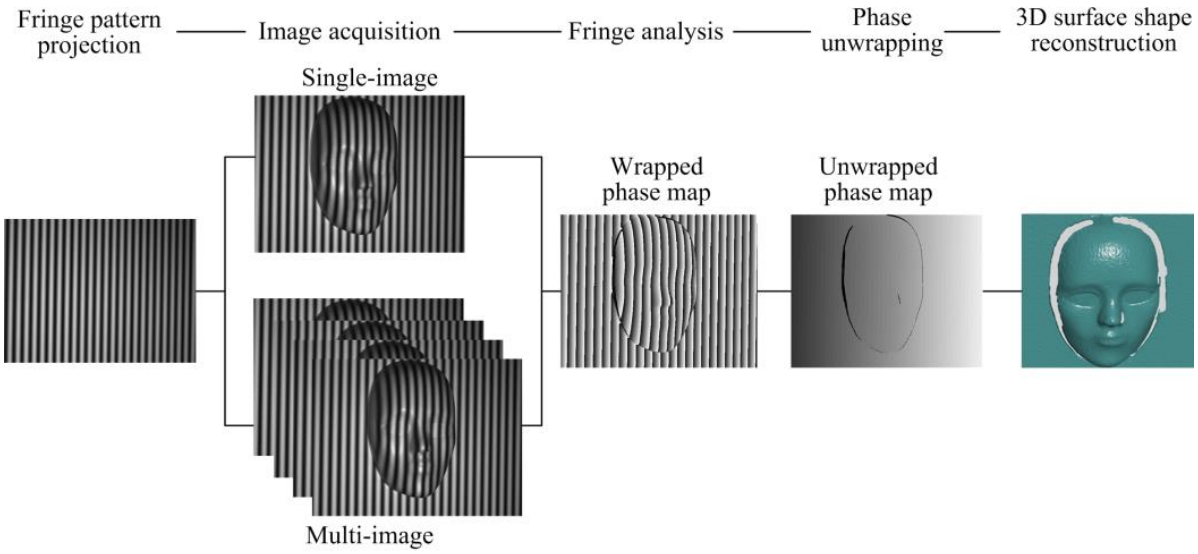

Figure 1.3. Work-flow in fringe projection profilometry.

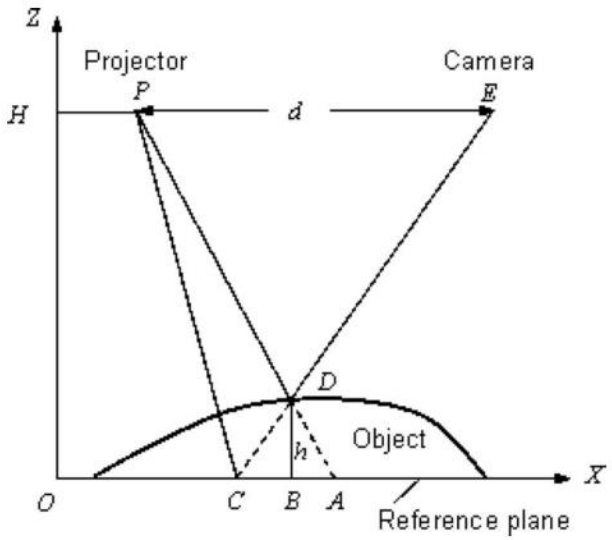

Figure 1.4. Relation between phase and height of object [19].

1.3.2.1 Fringe Analysis Techniques

The various fringe analysis techniques can be broadly classified into two categories: (1) single-shot spatial methods and (2) multi-shot phase-shifting methods [20].

Fourier transform profilometry (FTP) [21] is a well-known single-shot spatial method that uses a standard sinusoidal grayscale fringe projection for object surface measurement. The

deformed pattern is processed to determine the object shape from the fundamental frequency component in the Fourier spectra. However, this technique is limited to a finite maximum slope of depth variation, beyond which the fundamental frequency component would overlap other components and cannot be retrieved unambiguously, and the accuracy of the computed phase map would be compromised. To improve the measurement accuracy, Windowed FTP [22,23] divides the entire fringe pattern into a limited set of local fringe regions by using a moving window, which can suppress the effect of fringe noise and reduce the spectral leakage caused by local discontinuities. Wavelet transform [24,25] uses variable window sizes based on the frequencies, which can better detect the local characteristics of the fringe pattern. Although these approaches are "single-shot" (single image) techniques, the extensive digital signal processing to extract high-quality full-field height maps makes them unsuitable for real-time measurement. A modified FTP method was developed to remove the unwanted image background by using two fringe patterns with a π phase shift difference [26]. As a result, the modified FTP has a larger measurement range than the standard FTP method and has less computational cost than windowed FTP and wavelet transform methods, and thus may be suitable for implementation in real-time high-accuracy 3D measurement.

Multi-image phase-shifting profilometry (PSP) techniques, using grayscale sinusoidal [27], triangular [19], or trapezoidal fringe patterns [28], usually achieve higher accuracy and simpler computation than the FTP methods. The phase or intensity-ratio is calculated from several phase-shifted fringe patterns at each pixel, and then used to reconstruct the 3D surface shape of the object. Although the triangular or trapezoidal intensity-profile-pattern phase-shifting techniques could require fewer images and computations than other phase-shifting methods, the accuracy using these patterns is sensitive to projector focus [29]. The standard sinusoidal pattern phase-shifting technique is thus preferred.

For a standard three-step sinusoidal pattern phase-shifting algorithm with equal phase shifts, the camera-captured image intensities of the three phase-shifted fringe patterns are:

$$
\begin{aligned}
I_1(x,y) &= A(x,y) + B(x,y)\cos\left[\phi(x,y) - 2\pi/3\right], \\
I_2(x,y) &= A(x,y) + B(x,y)\cos\left[\phi(x,y)\right], \\
I_3(x,y) &= A(x,y) + B(x,y)\cos\left[\phi(x,y) + 2\pi/3\right],
\end{aligned} \tag{1.3}
$$

The phase map $\phi(x, y)$ can be computed by

$$
\phi(x,y) = \tan^{-1}\left[\frac{\sqrt{3}\left(I_1 - I_3\right)}{2I_2 - I_1 - I_3}\right]. \tag{1.4}
$$

Theoretically, three fringe patterns are the minimum requirement to completely solve for the three unknowns $A(x, y)$, $B(x, y)$ and $\phi(x, y)$ in Eq. (1.3). Phase-shifting can be extended more steps to reduce the measurement error [30] when the acquisition speed is not critical. For a sequence of N fringe patterns with equal phase shifts, the intensities of captured images are shown in Eq. (1.1). The phase map can be computed by:

$$
\phi(x,y) = \tan^{-1}\left[\frac{\sum_{n=1}^{N} I_n(x,y)\sin\left(\theta_n\right)}{\sum_{n=1}^{N} I_n(x,y)\cos\left(\theta_n\right)}\right]. \tag{1.5}
$$

The phase map calculated from Eq. (1.5) is wrapped in the range of the principal value ($-\pi$, π) with 2π discontinuities, due to the arctangent function [31]. This uncertainty of the phase value is known as the phase ambiguity problem. The wrapped phase map $\phi(x, y)$ needs to be unwrapped to a continuous phase map $\Phi(x, y)$ by phase unwrapping techniques (Figure 1.5) by adding or subtracting the integer multiplier $k(x, y)$ of 2π:

$$
\Phi(x,y) = \phi(x,y) + k(x,y)2\pi\,. \tag{1.6}
$$

Then the height at each pixel can be computed from the unwrapped phase $\Phi(x, y)$ to reconstruct the surface shape, either based on a phase-to-height mapping, determined in a system calibration (described in Section 2.1.1), or by using stereovision methods aided by the unwrapped-phase information (described in Section 2.1.2) .

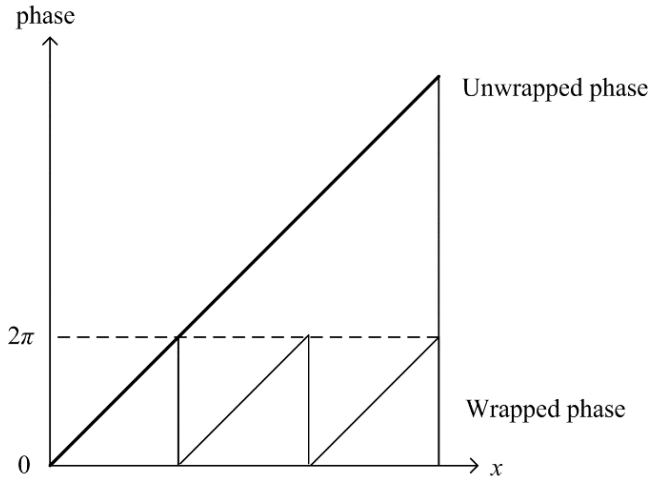

Figure 1.5. Phase unwrapping.

1.3.2.2 Phase Unwrapping Techniques

Approaches to solve the phase ambiguity problem in phase-shifting methods include spatial phase unwrapping, temporal phase unwrapping, and geometry-constraint based methods.

In spatial phase unwrapping methods, the true phase is retrieved by comparing the phase at neighboring pixels and adjusting phase discontinuities of 2π by following a continuous path on the wrapped phase map [32]. Although no extra images are needed for phase retrieval, the calculated phase is relative to a point on the phase map, and phase errors will propagate through the path, thus limiting spatial phase unwrapping to the measurement of objects without surface-geometry discontinuities that cause fringe shifting over 2π radians [33].

Temporal phase unwrapping methods avoid this problem by projecting an additional sequence of patterns and unwrapping the phase at each pixel independently. Gray-code patterns and multi-frequency fringe patterns are commonly used approaches that are easy to implement and have high reliability [31]. The gray-code method uses a series of gray-code patterns to identify the fringe order at each pixel, and yields a continuous absolute phase map by adding the phase order to the wrapped phase [34]. Figure 1.6 shows a series of four gray-code patterns which can uniquely denote 16 phase periods. For example, the gray codes for phase period P=1, P=2, P=3 are 0000, 0001, and 0011, respectively, where 0 and 1 represent

black and white, respectively, and codes are in order from top row to bottom, and the gray code for period P=16 is 1000. However, the binarization of camera-captured gray-code patterns is sensitive to the object surface reflectivity, especially at the period boundaries.

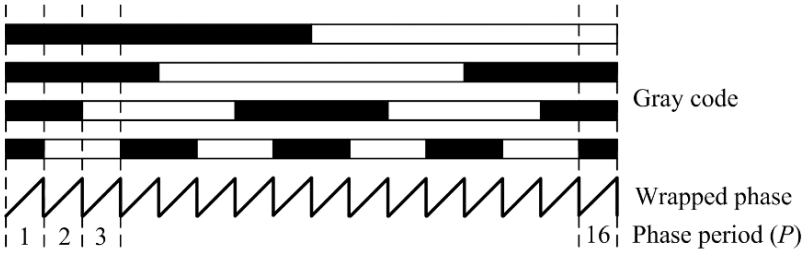

Figure 1.6. Gray-code phase unwrapping method.

Multi-frequency (multi-wavelength) phase unwrapping methods use multiple phase-shifted fringe patterns of different frequencies and unwrap the phase based on the heterodyne principle [35]. The heterodyne method consists of generating two different phase maps with two different wavelengths of fringe, λ_1 and λ_2. The phase-correct subtraction of these two phase maps has the desired synthetic (beat) wavelength λ_{12}, which can be used to determine the fringe order and unwrap the phase map. The beat wavelength can be computed by:

$$\lambda_{12} = \frac{\lambda_1 \lambda_2}{|\lambda_1 - \lambda_2|}. \tag{1.7}$$

An unambiguous measurement range can be increased to the synthetic wavelength at the beat frequency. Multi-frequency phase unwrapping using three frequencies (wavelengths) has been developed (Figure 1.7). The high-frequency phase maps $\phi_1(x)$, $\phi_2(x)$ and $\phi_3(x)$ are computed by the standard phase-shifting method, and the low frequency phase maps $\phi_{12}(x)$, $\phi_{23}(x)$ are obtained from $\phi_1(x)$ and $\phi_2(x)$, and $\phi_2(x)$ and $\phi_3(x)$, respectively, using the heterodyne principle. Then phase map $\phi_{123}(x)$ without phase ambiguity is obtained from $\phi_{12}(x)$ and $\phi_{23}(x)$. In total, three unambiguous phase maps can be generated by unwrapping each of the three initial phase maps. The noise of the absolute phase map can be further reduced by averaging the three unwrapped phase maps. Multi-frequency phase unwrapping using two frequencies was developed [36–38]. The phase map can be unwrapped using two

phases with co-prime frequencies. The major advantage of multi-frequency phase unwrapping methods is that high-frequency fringe patterns can suppress the phase error and the problem of unwrapping highly ambiguous phase maps is reduced to calculation of additional phase maps based on the standard phase-shifting technique. However, the method requires at least six fringe patterns for phase unwrapping; therefore, measurement of dynamic object surfaces (either moving or deforming) is difficult to achieve without motion artifacts.

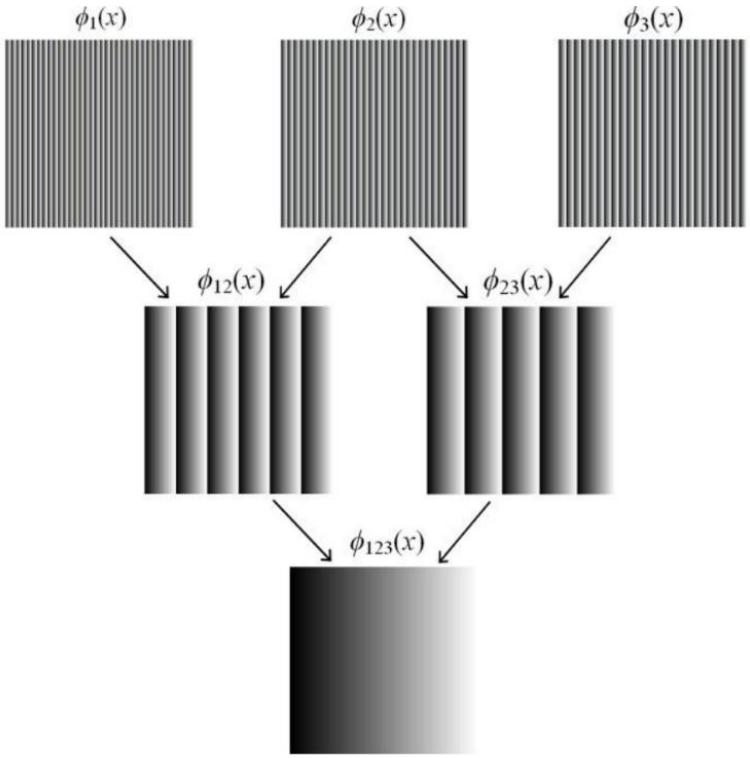

Figure 1.7. Multiple-frequency phase unwrapping method using three frequencies.

Geometry-constraint based methods can solve the phase ambiguity problem for discontinuous object surfaces without the need of additional patterns as in temporal phase unwrapping. Geometry-constraint based methods typically require one projector and two cameras, whereby phase maps can be obtained from two different perspectives (two camera viewpoints). Figure 1.8 shows epipolar geometry of a two-camera one-projector system [39]. O_{LC}, O_P, and O_{RC}, represent the left camera, projector, and right camera centres, respectively.

Q represents the point of interest on an object surface. Points p_{LC} and p_{RC} are the projections of point Q on the left and right camera image planes. The epipolar plane formed by Q, O_{LC} and O_{RC} intersects the left camera image plane at epipolar line e_{LC}, and the right camera image plane at epipolar line e_{RC}. For a point in one camera image, the corresponding point in the other camera image should be located on the epipolar line and have the same wrapped phase value. If the correspondences between the two camera images can be found for all points [6], the object surface can then be reconstructed directly by stereovision techniques.

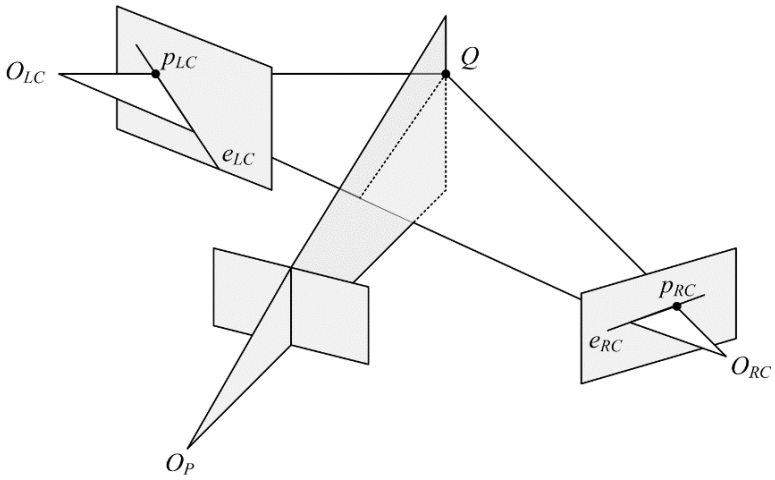

Figure 1.8. Epipolar geometry of a two-camera one-projector system.

The epipolar line is commonly used to reduce the search for the corresponding point. However, based on the wrapped phase value alone, there may be several corresponding-point candidates that can be found along the epipolar line. To reduce the number of candidates, the fringe patterns used in geometry-constraint based methods are usually designed with a relatively low frequency [39]. On the other hand, high-frequency fringe patterns lead to lower phase errors [40] and are therefore preferred for high-accuracy 3D measurement.

1.4 Motivation

In recent years, fringe projection profilometry has become a common method to achieve high-resolution and high-accuracy 3D surface-shape measurement, and there has been a

growing interest in implementing FPP in real-time 3D measurement systems, such as robotic vision, face recognition, and online 3D inspection systems [41].

Although temporal phase unwrapping method can solve the phase ambiguity problem for object surfaces with discontinuities, the additional required patterns, beyond the standard set of phase-shifted fringe patterns, make temporal phase unwrapping unsuitable for real-time applications. Geometry-constraint based methods that do not need additional patterns to the standard set of grayscale sinusoidal phase-shifted patterns are favorable for real-time applications. However, geometry-constraint methods suffer from the high computational cost and high complexity in selecting correct corresponding points between optical devices (projector and cameras), when high-frequency fringe patterns are used, and low accuracy when low-frequency fringe patterns are used. High-accuracy, high-resolution, real-time 3D shape measurement of complex objects with a minimal number of projected patterns is therefore still a challenge.

1.4.1 Limitations of Current Geometry-Constraint Based Methods Using Low-Frequency Fringe Patterns

In the commonly used phase-shifting technique, at least three phase-shifted fringe patterns are required for the phase computation to determine the object height (depth, shape). To solve the phase ambiguity problem without requiring additional projected patterns, the geometry-constraint based technique has demonstrated some success. However, the current geometry-constraint based methods are usually designed with low-frequency fringe patterns or a small measurement volume (short measurement range of depth) in order to minimize the number of object-surface candidate points in the measurement volume (Figure 1.9), and maximize the reliability of selecting the correct corresponding point during point correspondence search. Although in phase-shifting fringe-pattern profilometry, the use of high-frequency fringe patterns has been shown to be effective in increasing the measurement accuracy by suppressing the phase error [42], high-frequency fringe patterns may increase the number of corresponding-point candidates and reduce the effectiveness of geometry-

constraint based methods. Therefore, there is a trade-off in selecting the frequency of fringe patterns (low frequency for reduced number of candidates or high frequency for high accuracy). Furthermore, the frequency of fringe patterns used in current geometry-constraint based methods is usually determined empirically. Developing a method of theoretically determining the maximum fringe frequency that can be used in geometry-constraint based methods is still a problem that needs to be addressed. A theoretical mathematical model that relates the fringe frequency and geometry constraints is needed.

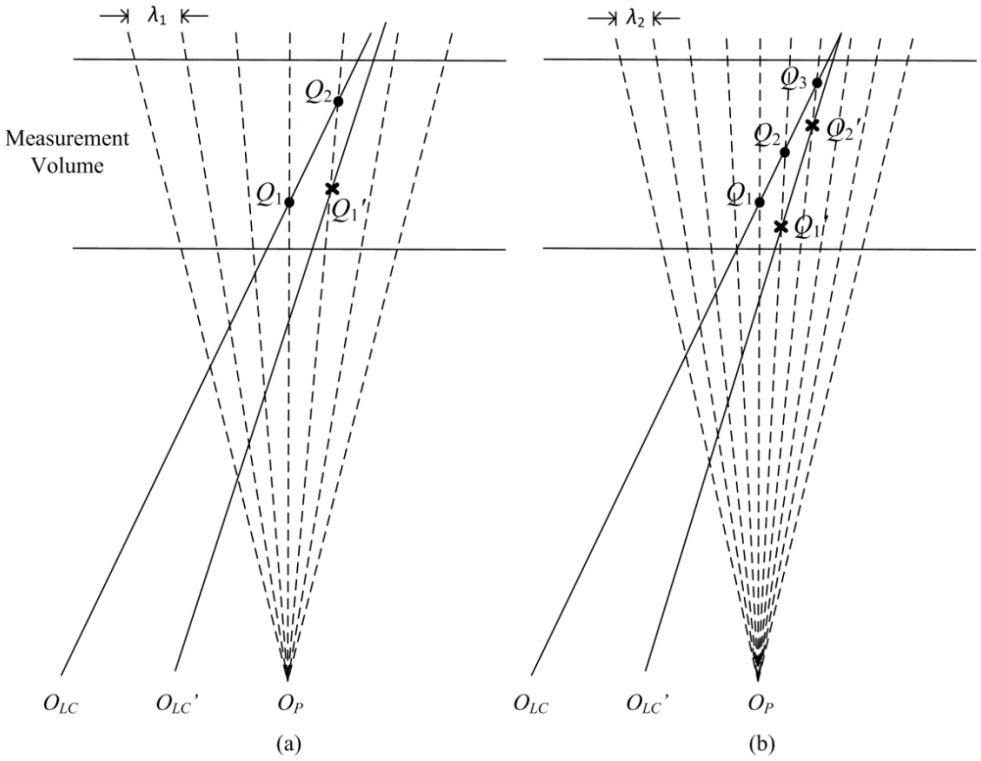

Figure 1.9. Relationship between fringe pattern wavelength, measurement volume, projector-camera baseline, and number of candidate-points: (a) few candidate points with longer fringe pattern wavelength λ_1 (low frequency), and (b) more candidate points with shorter wavelength λ_2 (high frequency).

1.4.2 Limitations of Current Geometry-Constraint Based Methods Using High-Frequency Composite Patterns

In geometry-constraint based methods, the use of high-frequency fringe patterns increases the number of object-surface candidate points of in the measurement volume (Figure 1.9) and thus the number of corresponding-point candidates on the epipolar line, To employ high-frequency fringe patterns while maintaining the reliability of geometry-constraint based methods, composite patterns have been used, where a speckle pattern [43][44] and triangular waves [45] are embedded with the sinusoidal fringe pattern, to provide extra information for selection of the correct corresponding point from a large number of candidates. However, the image correlation processing in the speckle-embedded scheme is time-consuming, and the triangular wave method is sensitive to the noise in the triangular wave intensity. The amplitude of the fringe pattern needs to be adjusted to embed the extra signals, and this decreases the signal-to-noise ratio (SNR) of the phase-shifted patterns. Other types of high-frequency composite patterns that are reliable in corresponding-point selection and have less effect on the SNR of phase-shifted patterns need to be developed.

Another challenge of geometry-constraint based methods using high-frequency fringe patterns is that they are computationally expensive. The extra computation in geometry-constraint based methods mainly lies in the calculation of epipolar-geometry parameters and coordinates of a large number of corresponding-point candidates, as well as the search and refinement of the correct corresponding point. Although parallel computing techniques can be employed to accelerate the whole process [39], a method that uses both high-frequency fringe patterns toward lower phase errors, and less computation toward faster measurement would be ideal. Furthermore, it is important to distribute the processing evenly to all available processor cores to achieve good performance on graphic processors [46]. Optimization of geometry-constraint based methods is thus necessary to minimize and evenly distribute the processing on Graphics Processing Unit (GPU) cores, and increase the processing speed for real-time applications.

1.4.3 Limitations of Current Real-Time 3D Measurement Methods

Ultimately, the speed of 3D measurement using FPP is limited by the image projection and acquisition speed of the projector and the camera, and the number of patterns required for a single measurement [47]. A consumer-grade digital projection system can project patterns at 60-120 frames per second (fps), which gives a maximum obtainable 3D measurement rate of 20-40 fps if the standard 3-step phase-shifting method is used. The 3D measurement rate will be further compromised if additional patterns are used for phase unwrapping. Increasing image projection and acquisition speed, and reduction of the number of projected patterns are two common ways to achieve real-time measurement at a higher rate. However, in practice, the speed of 3D measurement is also limited by computational cost and processing speed, which makes time-consuming methods, such as windowed-FTP and wavelet transform, not desirable in real-time 3D measurement. The computation should therefore be minimized for real-time low-cost applications. For measurement of dynamic surfaces, either moving or deforming, the use of fewer projected patterns and captured images in the 3D surface reconstruction is still preferred in order to reduce motion artifacts (errors due to surface motion between the capture of multiple images), especially for low-cost systems employing off-the-shelf hardware. Further reduction of motion-induced measurement error would be desirable to achieve high accuracy measurement of dynamic surfaces. Development of real-time motion-induced error compensation methods would be needed for real-time measurement.

1.5 Research Objectives

Geometry-constraint based techniques have high potential to achieve high resolution and accuracy using only few projected patterns, which would be advantageous for real-time 3D measurement. The main purpose of this research was to develop a 3D surface-shape measurement system with off-the-shelf devices, for real-time measurement of objects with surface discontinuities. The focus of the research was to develop new fringe-projection geometry-constraint based methods to address the limitations mentioned above (Section 1.5)

for high-accuracy, high-resolution 3D surface-shape measurement. The detailed objectives of this research were as follows:

1) Develop new geometry-constraint based techniques that use four background and amplitude encoded high-frequency fringe patterns, employing a single camera and projector. Investigate the geometry constraints of the single-camera single-projector system for reliable correspondence determination.

2) Develop new geometry-constraint based techniques that use four and two high-frequency composite patterns, respectively, employing two cameras and one projector. Investigate the geometry constraints of the two-camera one-projector system for reliable correspondence determination.

3) Investigate the mathematical relation between the fringe pattern wavelength (frequency) and the system geometry constraints for a two-camera one-projector system. Determine the best system setup and best wavelength of fringe patterns.

4) Develop theoretical improvements and investigate mathematical expressions of geometry-constraint parameters to address the problem of high computational cost in geometry-constraint based methods.

5) Investigate the measurement error due to object surface motion and develop a new method to compensate for motion-induced error for real-time 3D measurement.

6) Develop a real-time 3D surface-shape measurement system with off-the-shelf devices using parallel computing, and evaluate the developed system based on measurement accuracy and speed.

1.6 Thesis Outline

Chapter 1 introduced the main techniques of 3D surface-shape measurement and some challenges which provide motivation for the research directions, and the objectives of this research. Chapter 2 reviews the fundamental concepts and some of the common approaches of fringe projection profilometry. Chapter 3 presents a new background and amplitude coded

high-frequency fringe pattern method as part of a novel geometry-constraint based technique using a single camera and single projector. Chapter 4 presents a new fringe projection method that uses four high-frequency background modulation fringe patterns, using two cameras and one projector, and a new model that relates the fringe wavelength and system-geometry constraints. Chapter 5 details a new real-time 3D measurement method that uses only two fringe patterns for 3D surface reconstruction utilizing a modified FTP approach. Chapter 6 presents a new motion-induced-error compensation method for real-time 3D measurement of dynamic surfaces. Chapter 7 provides contributions of this research and discusses future work.

Chapter 2
Background and Literature Review

This chapter reviews the fundamental concepts and some of the common approaches of fringe projection profilometry, which can be potentially employed with geometry-constraint based techniques. The concepts include the system calibration, binary and grayscale coding, composite pattern techniques, geometry-constraint based methods, real-time measurement techniques, and motion-induced error compensation methods.

2.1 System Calibration

System calibration is required to determine the system parameters that relate the phase distribution (either wrapped phase map $\phi(x, y)$ or unwrapped continuous phase map $\Phi(x, y)$) to the 3D coordinates of points of an object surface. This relationship is dependent on the positions and orientations of the camera and projector.

2.1.1 Relative Phase-to-Height Mapping Model

A relative phase-to-height mapping model (Figure 1.4) can be used to describe the mapping between the phase difference and object out-off-plane height, where the phase difference is between the measured phase of the object and the reference plane [48]. The relative phase-to-height mapping model is usually related to the system parameters based on the system setup, such as the camera to projector baseline d (related to the angle between the projector and camera optical axes), the distance between the camera and reference plane H, and the pattern pitch p (related to fringe frequency) [49]. As mentioned in Section 1.3.2, the relative phase-to-height mapping can be generally described as:

$$h(x, y) = \frac{H}{1 + \frac{2\pi d}{p\Delta\phi}} \ , \tag{2.1}$$

where p is the pattern pitch (period width), and $\Delta\phi$ is the phase difference.

In practice, it is difficult to precisely measure the system parameters, such as H and d. System calibration is often performed by projecting phase shifted patterns onto a flat plate at multiple known positions (known object height map $h(x, y)$ at each position), computing phase maps for the different plate positions and a reference-plane position, computing the phase differences $\Delta\phi(x, y)$ between phase maps, and solving the non-linear relationship between $\Delta\phi(x, y)$ and $h(x, y)$ using a least-squares method [50,51]. Alternatively, a linear model $h(x, y) = K(x, y)\Delta\phi(x, y)$ can also be used to describe the phase-to-height mapping [49]. The above calibrations can be performed without explicitly determining the system parameters.

2.1.2 Stereovision Model

To determine 3D coordinates of points on an object surface from 2D camera image coordinates, a camera-based stereovision system needs to be calibrated to relate the image coordinates to 3D world coordinates, and the correspondences between images captured by two cameras from two perspectives are required. Correspondences between images are also required to calibrate the camera-based stereovision system.

In structured-light techniques, phase information can be used to determine correspondences between camera images of a two- or multi-camera system. In a single-camera single-projector stereovision system, one of the two cameras is replaced by a projector; and the projector can be calibrated as an inverse camera [52]. In both cases, phase information can be used to determined correspondences between camera and projector images, as explained in Section 2.1.3. Below, the general pinhole camera model, applicable to a camera and projector, is described.

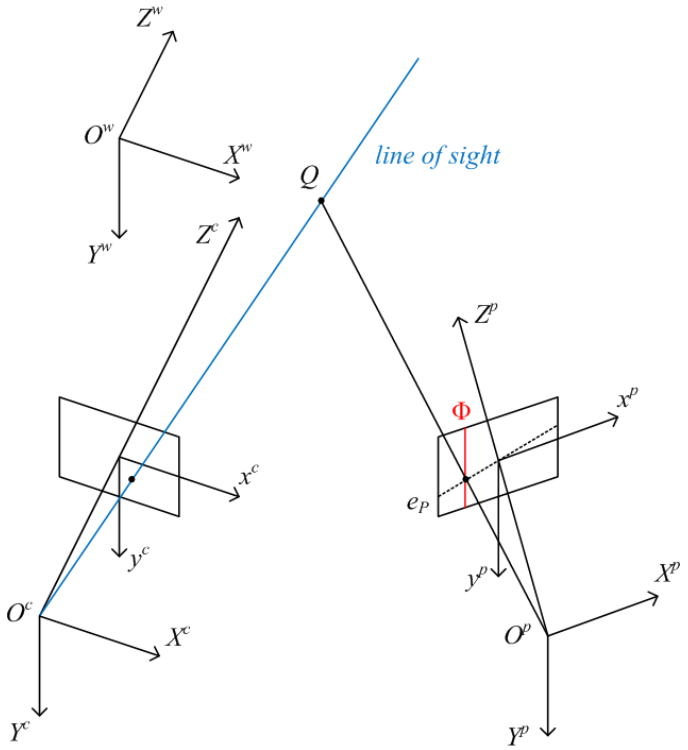

Figure 2.1. Stereovision model for a single-camera single-projector system.

For a single-camera single-projector system, the camera and projector lenses follow the well-known pinhole model [53]. O^w-$X^wY^wZ^w$, O^c-$X^cY^cZ^c$, and O^p-$X^pY^pZ^p$ are the world, camera, and projector coordinate systems, respectively. For a point Q on the object surface, the transformation of 3D world coordinates (X^w, Y^w, Z^w) to 3D camera coordinates (X^c, Y^c, Z^c) can be performed by:

$$\begin{bmatrix} X^c \\ Y^c \\ Z^c \end{bmatrix} = \begin{bmatrix} L & T_L \end{bmatrix} \begin{bmatrix} X^w \\ Y^w \\ Z^w \\ 1 \end{bmatrix} = \begin{bmatrix} l_{11} & l_{12} & l_{13} & t_1 \\ l_{21} & l_{22} & l_{23} & t_2 \\ l_{31} & l_{32} & l_{33} & t_3 \end{bmatrix} \begin{bmatrix} X^w \\ Y^w \\ Z^w \\ 1 \end{bmatrix}, \tag{2.2}$$

where L and T_L are the camera extrinsic-parameter matrices for rotation and translation with l and t matrix elements, respectively. The projection of 3D camera coordinates (X^c, Y^c, Z^c) to the camera normalized image plane is expressed as:

$$\begin{bmatrix} x_n^c \\ y_n^c \end{bmatrix} = \begin{bmatrix} X^c / Z^c \\ Y^c / Z^c \end{bmatrix}. \tag{2.3}$$

All the points imaged to this normalized projection (x_n^c, y_n^c) lie on a straight line, usually called the line of sight. The model for the camera is applicable to the projector since the projector can be treated as an inverse camera. The transformation of 3D world coordinates (X^w, Y^w, Z^w) to 3D projector coordinates (X^p, Y^p, Z^p) can be performed by:

$$\begin{bmatrix} X^p \\ Y^p \\ Z^p \end{bmatrix} = \begin{bmatrix} M & T_M \end{bmatrix} \begin{bmatrix} X^w \\ Y^w \\ Z^w \\ 1 \end{bmatrix} = \begin{bmatrix} m_{11} & m_{12} & m_{13} & t_4 \\ m_{21} & m_{22} & m_{23} & t_5 \\ m_{31} & m_{32} & m_{33} & t_6 \end{bmatrix} \begin{bmatrix} X^w \\ Y^w \\ Z^w \\ 1 \end{bmatrix}, \tag{2.4}$$

where M and T_M are projector extrinsic-parameter matrices for rotation and translation with m and t elements, respectively. Thus, the normalized projection on the projector image plane can be computed by:

$$\begin{bmatrix} x_n^p \\ y_n^p \end{bmatrix} = \begin{bmatrix} X^p / Z^p \\ Y^p / Z^p \end{bmatrix}. \tag{2.5}$$

According to epipolar geometry, the projection (x_n^p, y_n^p) must lie on the projector epipolar line e_P (Figure 2.1). Therefore, by solving the two sets of equations, Eq. (2.3) and (2.5), the 3D world coordinates (X^w, Y^w, Z^w) can be computed for every camera pixel, and the object surface reconstructed. The L and T_L parameters in Eq. (2.2), and the M and T_M parameters in Eq. (2.4) are the extrinsic parameters for rotation and translation, for the camera and projector, respectively. These extrinsic parameters can be determined together with the system intrinsic parameters, which are related to the system optics, by system calibration.

The general relation between the 2D image coordinates (u, v) and the normalized projection (x_n, y_n), which applies to the camera and projector, can be represented as:

$$\begin{bmatrix} u \\ v \\ 1 \end{bmatrix} = \begin{bmatrix} f_u & s & u_0 \\ 0 & f_v & v_0 \\ 0 & 0 & 1 \end{bmatrix} \begin{bmatrix} x_n \\ y_n \\ 1 \end{bmatrix}, \tag{2.6}$$

where f_u and f_v respectively, describe the effective focal lengths; s is the skew factor of u and v axes, which is usually assumed to be zero. (u_0, v_0) is the principal point. A nonlinear lens distortion model (up to five coefficients) is usually adopted for radial and tangential lens distortion [54], which can be described as:

$$\begin{aligned} \breve{x}_n &= x_n + x_n\left(k_1 r^2 + k_2 r^4 + k_3 r^6\right) + p_1\left(r^2 + 2x_n^{\,2}\right) + 2p_2 x_n y_n, \\ \breve{y}_n &= y_n + y_n\left(k_1 r^2 + k_2 r^4 + k_3 r^6\right) + 2p_1 x_n y_n + p_2\left(r^2 + 2y_n^{\,2}\right), \end{aligned} \tag{2.7}$$

where $r = \sqrt{x_n^{\,2} + y_n^{\,2}}$ denotes the radius from the centre of the image plane to the image point. k_1, k_2, k_3, p_1, and p_2 are distortion coefficients. $(\breve{x}_n, \breve{y}_n)$ is the normalized projection after distortion. To calibrate the camera, images of a planar pattern from a few (at least two) different orientations are captured, and the intrinsic parameters (f_u , f_v , u_0, v_0 , k_1, k_2, k_3, p_1, and p_2), and extrinsic parameters can be determined using a least-mean-squares method [55].

2.1.3 Projector Calibration

Since the projector cannot capture images, to calibrate the projector in a similar way as the camera, a virtual image is created as if captured directly by the projection chip. In fringe projection profilometry, the correspondences between camera pixels and projector pixels can be established based on the phase maps, since a projection (x_n^p, y_n^p) on the projector image plane should have the same phase value as its corresponding point (x_n^c, y_n^c) on the camera image plane. By projecting fringe patterns in vertical and horizontal orientations, the phase value for each camera pixel, on the vertical unwrapped phase map $\Phi_v(u, v)$ and horizontal unwrapped phase map $\Phi_u(u, v)$ can be used to find two lines of corresponding pixels on the projector virtual image plane, $u = u^p$ and $v = v^p$, respectively (Figure 2.2). The two lines can be computed by:

$$u^p = \Phi_u \lambda_u / 2\pi,$$
$$v^p = \Phi_v \lambda_v / 2\pi, \tag{2.8}$$

where λ_u and λ_v are the wavelengths of the vertical and horizontal fringe patterns, respectively. The intersection of the two lines on the projector virtual image plane $P^p(u^p, v^p)$ is the corresponding point to camera pixel $P^c(u^c, v^c)$ [52]. Thus, a one-to-one mapping of the camera image and the virtual projector image is obtained.

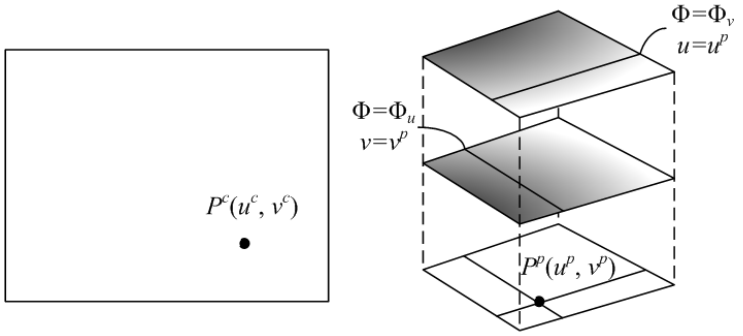

Figure 2.2. Corresponding point to a camera pixel on the projector virtual image plane.

The camera and projector can be placed arbitrarily, and the calibration of this system model is easy to implement in practice. A final calibration refinement is usually implemented by minimizing the reprojection error between the image locations of observed and predicted image points using nonlinear least-squares algorithms [56]. However, the projector calibration is error prone, because the location of the projector principal point is outside the projector chip [57,58], and the projector lens distortion thus cannot be well described by a distortion function. A sub-pixel projector calibration method can improve the accuracy of projector calibration [59]. A second camera can be added to form a two-camera, single-projector system, when system size and cost are of secondary importance to measurement accuracy. Calibration can then be carried out on the two cameras, to provide more accurate system parameters, and the correspondence between two cameras is obtained using phase. Therefore, higher measurement accuracy can be achieved in 3D measurement with a two-camera single-projector system than for a single-camera single-projector system.

2.2 Binary Coding and Grayscale Coding Techniques

Binary coding [60] methods use black and white stripes to form a sequence of projection patterns to generate a binary code for every image pixel. The code word varies across the whole image, segmenting the image into several unique regions. In general, N binary patterns can code 2^N stripes, such that 2^N unique regions are coded. A gray-code binary pattern (Figure 1.6) is commonly used in binary coding techniques. Since patterns are black or white, not grayscale, the binary coding technique is not sensitive to projector gamma nonlinearity, and is thus reliable. The technique can be used solely or together with phase-shifted patterns to uniquely determine the fringe order for phase unwrapping. When binary patterns are used alone, at least 8 sequential patterns are required to code 256 stripes [61]. Even more patterns are needed to achieve higher spatial resolution.

To effectively reduce the number of patterns, grayscale patterns are developed, where a code with K intensity levels is applied, such that N patterns code K^N stripes. This greatly increases the capacity of identifying unique regions [62]. When grayscale patterns are used together with phase-shifting fringe patterns, fewer grayscale patterns are required to determine the order of the wrapped phase than binary patterns. However, it would be difficult to distinguish adjacent intensity levels, if a large number of codewords were used to determine fringe order, or if the object surface reflectivity was not uniform. An amplitude-modulation fringe pattern method can encode the fringe order information into the amplitude of fringe patterns [63]. Codewords can also be embedded into the phase by phase-coding methods [64,65]. Since phase-coding is less sensitive to the influence of sensor noise, ambient light, and object surface reflectivity, phase is more reliable to carry information than intensity. A large number of codewords can be used in phase-coding by adding more phase-coded patterns [66]. However, at least six patterns are still required for the phase-coding method. The aperiodic sinusoidal fringe method [67] uses grayscale sine-shaped fringes with spatially and temporally varying offset, amplitude, period length, and phase shift to avoid the phase ambiguity problem. However, nine patterns are required for a good compromise between measurement accuracy and computation time.

2.3 Composite Pattern and Colour Pattern Techniques

To reduce the number of projected images, composite patterns are developed, where multiple binary or grayscale patterns are embedded into the phase-shifted fringe patterns (commonly sinusoidal), thus modulating the amplitude or background intensity of the phase-shifted fringe patterns [68–70]. The embedded binary or grayscale patterns usually can be extracted independently from the phase map computation, and then used to unwrap the phase. In practice, however, the amplitude of the phase-shifted fringe patterns needs to be adjusted to embed the extra patterns, and this decreases the signal-to-noise ratio (SNR) of the phase-shifted patterns. It is preferred that the embedded patterns are designed to be simple for high phase-analysis reliability and to lower the computational cost.

Some other grayscale composite pattern techniques combine sinusoidal fringe patterns with different frequencies or different directions [71–74], where each fringe pattern is extracted by Fourier analysis. These techniques aim to reduce the number of projected patterns to only one, for real-time measurement. However, some information at the object edges or low modulation zones may be lost due to the Fourier analysis.

Similar to composite pattern methods, colour pattern methods use a colour projector and camera and embed phase-shifted fringe patterns or binary/grayscale coded patterns into three RGB channels [75–78]. However, the crosstalk among three channels makes it difficult to split three primary colour components correctly from a colour fringe pattern. The measurement accuracy will be reduced significantly [79]. Although many methods [80] are proposed to address the crosstalk, the colour patterns are sensitive to the object surface colour and ambient light, which would introduce unexpected phase error. Therefore, grayscale patterns are still preferred for high-accuracy 3D measurement.

2.4 Geometry-Constraint Based Techniques

Geometry-constraint based techniques permit reconstruction of the object surface directly from the wrapped phase map without requiring additional patterns. Apart from the embedded speckle pattern [43][44] and triangular wave [45] methods mentioned earlier, one single-

image geometry-constraint based technique uses Fourier analysis to obtain the wrapped phase maps for both cameras of a two-camera single-projector system [81]. However, the additional image processing to obtain the disparity map to determine correspondences would reduce the processing speed in real-time applications. One composite pattern method uses multi-frequency and four-step phase-shifted sinusoidal fringes to measure relative depth, and then employs geometric analysis to obtain absolute object depth [82]. A disadvantage of the method is that a large number of images were still required for 3D measurement. A correspondence finding method, based on space conversion, performs a search for corresponding points between two camera images in the projector image coordinate system [83]. However, additional computations were needed for space conversion. Recently, geometry-constraint based methods with a single-camera, single-projector system were developed without requiring correspondence search. The phase map was unwrapped based on artificial absolute phase maps generated by geometry constraints [84–86]. A limitation of the method is that prior-knowledge of the approximate surface geometry, or a known object was required. A bi-frequency phase-shifting method was also applied in a geometry-constraint based system, which uses three high-frequency phase-shifted patterns to obtain a high-accuracy phase map and two low-frequency phase-shifted patterns to unwrap the phase map [87]. However, five images were still required. Another method uses three-step phase-shifted fringe patterns and computes the absolute phase using one additional coded pattern and system geometry constraints [88]. However, the grayscale coded pattern would be sensitive to ambient light and object surface reflectivity. A quad-camera system was developed by using four cameras to provide additional geometric information to solve severe phase ambiguities caused by high frequency fringe patterns [89]. The system cost would be high since four cameras were used. Later, an adaptive depth constraint approach was proposed for high-accuracy real-time 3D measurement, where the measurement depth volume for geometric constraints was adaptively updated according to the current reconstructed geometry [90]. The accuracy of geometry-constraint based techniques is discussed in [91], which shows that measurement errors made in a two-camera single-projector system can be

considerably smaller than for a single-camera single-projector system, since phase errors would occur similarly in both camera images. A model of the measurement volume and system geometry is described with relations between triangulation angles, fringe frequency, and measurement volume depth [92,93]. However, this model is simple and only based on the phase-to-height mapping model.

2.5 Real-Time 3D Surface-Shape Measurement Techniques

For real-time 3D surface-shape measurement, fast projection techniques, single-image techniques using a composite or colour pattern, and multi-image techniques with reduced number of projected patterns are common approaches that permit phase analysis to be applied for dynamic (moving or deforming) surfaces.

Increasing image acquisition speed to reduce the effect of object motion during measurement has been achieved using high-speed projectors and cameras [94]. For example, Goes Before Optics (GOBO) projection can achieve high pattern-switching speeds with a high-speed spinning wheel [95,96]. However, high speed pattern projection and image capture is achieved at a higher system cost. High projection speed has also been achieved using defocused binary patterns to generate sinusoidal fringe patterns [97,98]. However, the projector needs to be properly defocused to generate good-quality sinusoidal fringe patterns. Otherwise, measurements will have large errors due to the non-sinusoidal waveform of the fringe patterns, and would require error compensation, such as using a pre-calibrated look-up table (LUT) method, to reduce the error.

The single-image method is ideal for dynamic measurement of fast-moving objects. Many real-time 3D measurement systems were developed using a single-shot colour pattern [99,100], single-shot composite pattern [101], or single-shot sinusoidal pattern, where phase is analyzed using FTP [102]. However, as mentioned above, single-image composite pattern and colour pattern methods have complex image demodulation and high sensitivity to object surface colour, respectively, which leads to phase error, and the single-image FTP method is limited to a finite maximum slope of depth variation.

Multi-image methods with reduced number of projected patterns have also been used to achieve real-time measurement. A multi-image composite pattern method, where each pattern contains fringes at two frequencies, achieved a fast processing rate by using a look-up table (LUT) method [103]. However, the accuracy is compromised due to low frequency fringe patterns. A two-frequency two-image FTP approach has been combined with geometry-constraint based techniques to perform dynamic measurement [104]; however, there remains a challenge in separating different frequency components, which would affect measurement accuracy. A method that can achieve real-time without compromising measurement accuracy is still needed.

2.6 Motion-Induced Error Compensation Techniques

Due to the advantage of the high accuracy of multi-image phase-shifting methods, multi-image methods may be preferred even for real-time 3D surface measurement if some computation processes can be eliminated and the errors caused by motion can be reduced. There has been a growing interest in developing methods to compensate for errors caused by object motion between the successive images captured during measurement.

Marker based [105,106] and Scale Invariant Feature Transform (SIFT) [107] methods can compensate for measurement error due to planar object motion without handling motion in the depth direction. Filtering in the frequency domain can reduce errors on the object edges caused by object motion [108]. In PSP, fringe patterns are projected with known phase shift, and PSP phase-analysis algorithms can solve for the phase shift due to the object surface geometry. In the captured images, object surface motion will cause an additional unknown phase-shift, resulting in motion-induced phase error and thus depth measurement error. Several error compensation methods can handle errors due to motion in the depth direction. One phase error compensation method for dynamic 3D measurement is based on the assumption that the motion-induced phase-shift error is homogeneous within a single object [109]. The estimation of phase-shift error may not be accurate if the object is deforming and the motion-induced phase-shift error is non-homogeneous (non-uniform across the object

surface). One pixel-independent phase-shift error estimation method using FTP computed phase map differences of successive captured fringe images [110]. Another method fused FTP and PSP surface reconstruction, guided by phase-based pixel-wise motion detection [111]. Although the latter two methods work well to handle object motion, the measurement accuracy would be limited where there is high depth variation due to the use of FTP. Another method used the Hilbert transform to generate an additional set of fringe images and additional phase map, which can substantially compensate motion-induced error by averaging the original and additional phase maps [112]. However, use of the Hilbert transform requires additional processing to suppress errors at fringe edges [113].

Iterative methods [114,115] can estimate non-homogeneous phase-shift error and then compute phase using the generic phase-shifting algorithm while considering the phase-shift error. The method can achieve very high accuracy with little motion-induced error after several iterations. While these motion-induced-error compensation methods work well for fast moving or deforming surfaces, they are computationally expensive and not suitable for real-time applications. A method that can perform pixel-wise motion-induced-error compensation in real-time measurement and also handle objects with large depth variation would be ideal.

2.7 Discussion

Different techniques have been developed to achieve the goal of high-accuracy, high-resolution, 3D surface-shape measurement. Two main system calibration models have been developed. Generally, stereovision has more flexibility in system calibration than phase-to-height mapping, and it can be further extended to a multi-camera single-projector system.

Regarding pattern projection techniques, single-shot fringe projection has the fastest image acquisition speed but suffers from high computational cost and errors occurring with object surface colour and high surface-geometry gradient. Multi-image grayscale phase-shifting techniques can handle objects with colour and high depth variation and are thus preferred. Multi-frequency phase-shifting techniques can solve the phase ambiguity problem and

achieve high accuracy. However, a large number of fringe patterns are required for one measurement, which is not suitable for moving or deforming objects. Fast projection techniques solve this problem, but require expensive devices and high illumination. Geometry-constraint based techniques use fewer patterns and are thus more suitable for dynamic measurement of objects with surface discontinuities, without the drawbacks of the aforementioned techniques. A method based on geometry-constraints that uses high-frequency grayscale phase-shifting patterns toward higher phase accuracy, and a minimal number of projected patterns toward fast measurement, would be preferred for full-field real-time 3D surface-shape measurement. To reduce motion-induced measurement error, a non-iterative, pixel-wise motion-induced-error compensation method that can handle surfaces with large depth variation is needed.

Chapter 3
High-Frequency Background and Amplitude Encoded Fringe Pattern Method

The grayscale composite pattern method, where binary or grayscale patterns are embedded in phase-shifted patterns, can reduce the total number of projected patterns for 3D measurement. In this chapter, a new background and amplitude coded high-frequency fringe pattern method is developed as part of a novel geometry-constraint based technique using a single camera and single projector. The background and amplitude are combined as a codeword to identify the wrapped phase fringe order to partially unwrap the high-frequency phase map to a low frequency wrapped phase map. The low-frequency wrapped phase map is then directly used to reconstruct the surface based on system geometric constraints without using additional images as in other temporal phase-unwrapping methods, and without the limitations of spatial phase-unwrapping methods, which cannot handle surface discontinuities.

3.1 Principle and Method

3.1.1 Background and Amplitude Modulation Fringe Patterns

For 3D surface-shape measurement in high-speed, high-accuracy applications, a four-step phase-shifting method is desirable. The phase-shifted patterns are encoded with different background and amplitude values for different periods across the pattern. The projected fringe images I_n (n = 1, 2, 3, 4) for four phase-shifted patterns, are given by the following equations:

$$\begin{aligned} I_1(x,y) &= A_1(x,y) + B_1(x,y)\sin\phi(x,y), \\ I_2(x,y) &= A_2(x,y) + B_2(x,y)\sin\left[\phi(x,y) + \pi/2\right], \\ I_3(x,y) &= A_1(x,y) + B_3(x,y)\sin\left[\phi(x,y) + \pi\right], \\ I_4(x,y) &= A_2(x,y) + B_4(x,y)\sin\left[\phi(x,y) + 3\pi/2\right], \end{aligned} \tag{3.1}$$

where A_1, A_2 represent two different background intensity values, and B_1, $B_{2....}$ B_4 represent four different amplitudes. The intensity of the camera-captured image of the projected fringe pattern would be affected by the object surface reflectivity and ambient light. However, as long as the camera sensor is not saturated [18], the phase ϕ can be computed independently of the object surface reflectivity and ambient light as well as the designed background intensity:

$$\phi(x, y) = \tan^{-1}\left(\frac{I_1 - I_3}{I_2 - I_4}\right). \tag{3.2}$$

A code pattern could therefore be embedded into the projected image using varying background, without affecting the wrapped phase. Similarly, a code pattern could also be embedded into the projected image by varying the amplitude. As long as $B_1 + B_3 = B_2 + B_4$, the phase can be obtained by:

$$\phi(x, y) = \tan^{-1}\left[\frac{(B_1 + B_3)\sin\phi}{(B_2 + B_4)\cos\phi}\right]. \tag{3.3}$$

To distinguish phase order, both background and amplitude are modulated for each phase period. The background and amplitude assignments to the projected pattern, in order to uniquely denote the order of the 12 phase periods *P*, are specified in detail in Table 3.1 and Table 3.2, respectively, where a_1, a_2 (a_1>a_2) are the different background values for specific periods, and *b* is an amplitude value.

Table 3.1. Background assignments for intensities I_1, I_2, I_3, I_4, for specific periods *P*.

		P		
I_i		1-4	5-8	9-12
I_1	A_1	a_1	a_1	a_2
I_2	A_2	a_1	a_2	a_1
I_3	A_1	a_1	a_1	a_2
I_4	A_2	a_1	a_2	a_1

Table 3.2. Amplitude assignments for intensities I_1, I_2, I_3, I_4, for specific periods P.

		P											
I_i		1	2	3	4	5	6	7	8	9	10	11	12
I_1	B_1	$2b$	b	b	$2b$	$2b$	b	b	$2b$	$2b$	b	b	$2b$
I_2	B_2	$2b$	b	$2b$	b	$2b$	b	$2b$	b	$2b$	b	$2b$	b
I_3	B_3	b	$2b$	$2b$	b	b	$2b$	$2b$	b	b	$2b$	$2b$	b
I_4	B_4	b	$2b$	b	$2b$	b	$2b$	b	$2b$	b	$2b$	b	$2b$

Eq. (3.4) shows an example, I_1, with modulated background and amplitude for 12 phase periods P, while the normalized modulated intensities for all four encoded fringe patterns (I_1, I_2, I_3, I_4), are shown in Figure 3.1, and the normalized intensity of I_1 for periods 7–10 (dashed rectangle in Figure 3.1a) is shown in detail in Figure 3.2.

$$I_1 = \begin{cases} a_1 + 2b\sin\phi, & P = 1,4,5,8, \\ a_1 + b\sin\phi, & P = 2,3,6,7, \\ a_2 + 2b\sin\phi, & P = 9,12, \\ a_2 + b\sin\phi, & P = 10,11. \end{cases} \tag{3.4}$$

To identify the phase order, the encoded background and amplitude pattern must be extracted correctly at each phase period. For both background and amplitude code assignments, only two codewords are used, thus benefitting the reliability and success rate of code extraction. If more codewords were used, ideally more phase periods could be denoted uniquely; however in practice, it would be more difficult to determine the threshold for reliable code extraction. Therefore, instead of applying more codewords, geometric constraints are used to further expand the number of phase periods to 48. The higher fringe pattern frequency aims to reduce sensitivity to image noise.

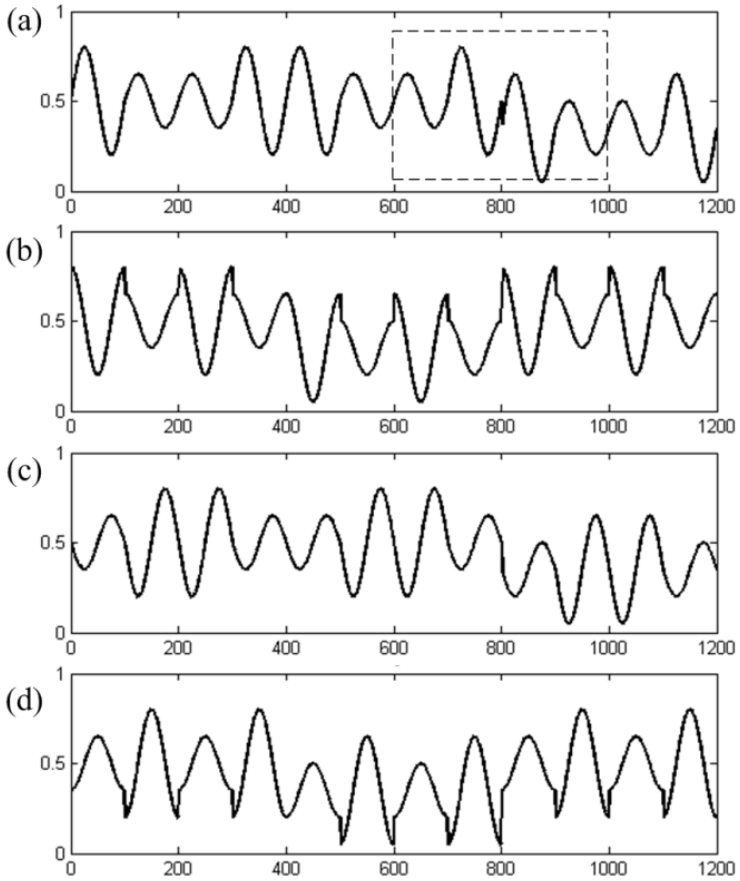

Figure 3.1. Normalized modulated intensities for all four encoded fringe patterns for the 12 periods P: (a) I_1, (b) I_2, (c) I_3, and (d) I_4.

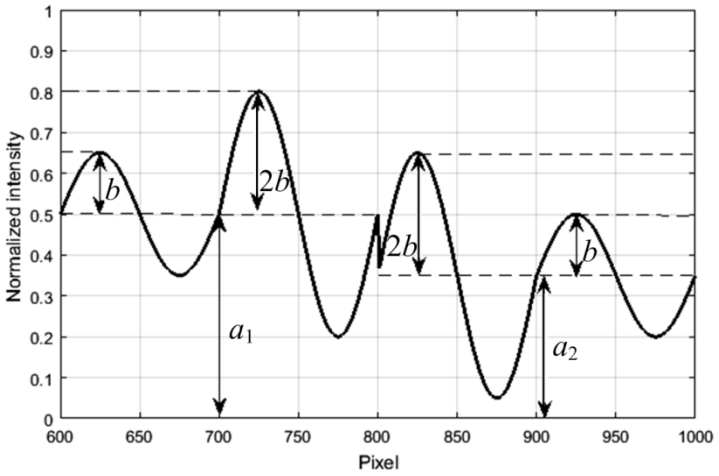

Figure 3.2. Normalized modulated intensities for I_1 periods 7–10 (dashed rectangle region in Fig. 3.1).

3.1.2 Overview of Background and Amplitude Extraction and Phase-Order Determination

The extraction of the background and amplitude from the captured images is carried out as follows. The background code divides the whole pattern into three sections, periods 1 to 4, 5 to 8, and 9 to 12, as seen in Table 3.1, and the amplitude code pattern further segments each section into the four respective periods (Table 3.2). For each pixel (x, y) of image $I(x, y)$, the background intensity is extracted first, to identify in which of the three sections the pixel coordinate x lies. The amplitude is then extracted to identify in which of the four periods (within the section) the pixel belongs to. In this way, any phase period order (P = 1, 2, ... 12) can be identified uniquely. When the number of periods is greater than twelve, such as 48 periods (a multiple of 12 is needed), geometry constraints are required to determine which multiple of 12 periods the pixel belongs to. The application of background and amplitude extraction, and geometry constraints can thus uniquely determine the phase period order (P = 1, 2, … 48).

3.1.3 Background Code Extraction

According to Eq. (3.1), the sinusoidal component of I_1 and I_3 can cancel each other at each phase period. As an example, the calculation of the background for P = 5, 6, 7, 8 is detailed in Table 3.3. If the period orders were known, background A_1 could be extracted directly from $\left(I_1 + 2I_3\right)/3$ at periods 5 and 8, and from $\left(2I_1 + I_3\right)/3$ at periods 6 and 7, as follows:

$$A_1 = \left(I_1 + 2I_3\right)/3, \quad P = 5,8 \tag{3.5}$$

$$A_1 = \left(2I_1 + I_3\right)/3, \quad P = 6,7 \tag{3.6}$$

and similarly, background A_2 can be extracted as:

$$A_2 = \left(I_2 + 2I_4\right)/3, \quad P = 5,7 \tag{3.7}$$

$$A_2 = \left(2I_2 + I_4\right)/3, \quad P = 6,8 \tag{3.8}$$

Since the period order is unknown, it is necessary to determine which equations are applicable, either Eq. (3.5) or (3.6) and either Eq. (3.7) or (3.8), to extract the correct background for each phase period.

Table 3.3. Background extraction for period P: 5–8.

P	5	6	7	8
$(I_1+2I_3)/3$	a_1	$a_1 - b\sin\phi$	$a_1 - b\sin\phi$	a_1
$(2I_1+I_3)/3$	$a_1 + b\sin\phi$	a_1	a_1	$a_1 + b\sin\phi$
$(I_2+2I_4)/3$	a_2	$a_2 - b\cos\phi$	a_2	$a_2 - b\cos\phi$
$(2I_2+I_4)/3$	$a_2 + b\cos\phi$	a_2	$a_2 + b\cos\phi$	a_2

The background extraction is performed as follows:

1) Calculate the wrapped phase map, which has a range of $(-\pi, \pi)$, using the captured images. For each row of the wrapped phase map, compare neighboring pixels and detect phase jumps of 2π to localize each phase period.

2) Segment the phase period into two parts: $(-\pi, 0]$, $[0, \pi)$. For each part, calculate A_1 at each pixel using both Eqs. (3.5) and (3.6). The smaller range of A_1 indicates that the correct background has been calculated, and the A_1 values are used for further processing of the image. A similar procedure is used to calculate the correct A_2 using Eqs. (3.7) and (3.8).

3) Apply a median filter to the extracted background.

The phase is segmented into two parts (in Step 2 above) because for objects with varying reflectivity, the range of the background intensity for the entire period would be large, making it difficult to determine the correct background. After extraction of A_1 and A_2, the three sections can be identified according to the background assignments. To take the surface reflectivity into account, a background intensity threshold τ is calculated:

$$\tau = C\left(a_1 - a_2\right)/2, \tag{3.9}$$

where C is related to the object surface reflectivity and estimated by:

$$C \approx \left(A_1 + A_2\right)/255 . \tag{3.10}$$

The threshold τ is then used to identify the three sections as follows: if $(A_1 - A_2) > \tau$, then $P = [5, 8]$; if $(A_1 - A_2) < -\tau$, $P = [9, 12]$; and if $-\tau \le (A_1 - A_2) \le \tau$, $P = [1, 4]$. The threshold value is thus adapted to the reflectivity of a surface region.

3.1.4 Amplitude Code Extraction

After background extraction, amplitude ratios B_1/B_3 and B_2/B_4 can be calculated easily by removing the background intensity (A_1 and A_2) from captured images:

$$\begin{aligned} B_1/B_3 &= \left|\frac{I_1 - A_1}{I_3 - A_1}\right|, \\ B_2/B_4 &= \left|\frac{I_2 - A_2}{I_4 - A_2}\right|. \end{aligned} \tag{3.11}$$

Since the background intensity can be removed in Eq. (3.11), the object surface reflectivity and ambient light will not affect the amplitude ratio. The amplitude ratio B_1/B_3 and B_2/B_4 only have two possible values 0.5 or 2. As an example, Table 3.4 shows the ideal calculation result of the amplitude ratios for periods 5 to 8.

Table 3.4. Amplitude ratio extraction for periods P: 5–8.

	P			
Ratio	5	6	7	8
B_1/B_3	2	0.5	0.5	2
B_2/B_4	2	0.5	2	0.5

A threshold of 1 is used to binarize the result of Eq. (3.11). If amplitude ratio $B_1/B_3 > 1$ and $B_2/B_4 > 1$, then $P = 5$; if $B_1/B_3 < 1$ and $B_2/B_4 < 1$, then $P = 6$. The amplitude ratio for other periods can be extracted in a similar way. Thus, any phase order ($P = 1, 2, \ldots 12$) is identified uniquely. However, the identified phase order could be error prone due to high-reflectivity

regions of an object, at low-contrast or defocused regions, and at edges of sinusoidal fringes (edge points). Furthermore, if an incorrect background is extracted in these regions, the error would propagate to the extraction of the amplitude ratio, resulting in an incorrect phase order. Therefore, after extracting the background and amplitude ratio and preliminarily identifying the phase order (P = 1, 2, ... 12), as above, a phase order correction is necessary.

3.1.5 Phase-Order Correction

The way fringe background and amplitude are coded is independent of the wrapped phase calculation. The wrapped phase map thus still has high resolution and accuracy. The task of phase order correction is to assign the correct phase order to each phase period of the wrapped phase. Although the phase order in one phase period may have error at high-reflectivity regions of an object, at low-contrast or defocused regions, and at edge points, the preliminarily identified phase orders at most remaining regions are still reliable, and can be used to correct the phase order error.

The phase order correction is performed as follows:

1) Apply a region growing algorithm on the wrapped phase map and segment all phase periods. All pixels in one region should have the same phase order.
2) In each region, generate a histogram based on the preliminarily identified phase order. Assign the phase order which has largest frequency (count) to all pixels in that region.

After phase order correction, the corrected phase order is assigned to generate the unwrapped phase map.

3.1.6 Geometric Constraints

If the number of periods in the fringe pattern is twelve, the unwrapped phase without any phase ambiguity can be obtained by the aforementioned method. To suppress the phase error, the number of periods is first extended to 48 by performing the designed background and amplitude code assignments four times. Since this approach can only unwrap the phase to a low frequency that still has four periods, geometric constraints are required to uniquely

identify the period, P = 1, 2, ... 48. Considering a single-camera single-projector setup, each "line of sight" from a camera pixel would intersect with four equiphase planes (from the projector). The four intersection points are considered as four candidate positions for a point on the object surface. Only one candidate is true, the one on the object surface, while the other three candidates are false. Geometric constraints are then used to eliminate false candidates. With a properly designed camera-projector system, the false candidates would be located outside the measurement volume.

As shown in Figure 3.3, a triangulation model of a camera-projector system, P and C denote the centres of the projector and camera, respectively; d is the length of the camera-projector baseline; and $z_{\min}$ and $z_{\max}$ are the minimum and maximum depth of the measurement volume, respectively. The width of the projector field of view (FOV) at maximum measurement depth is w. Assuming point A is the true candidate on the object surface, which is also at maximum measurement depth, Point B (the nearest false candidate) is the intersection of the same "line of sight" and a neighbouring equiphase plane. The depth difference between A and B is:

$$z_{AB} = \frac{wz_{\max}}{w + 4d}. \tag{3.12}$$

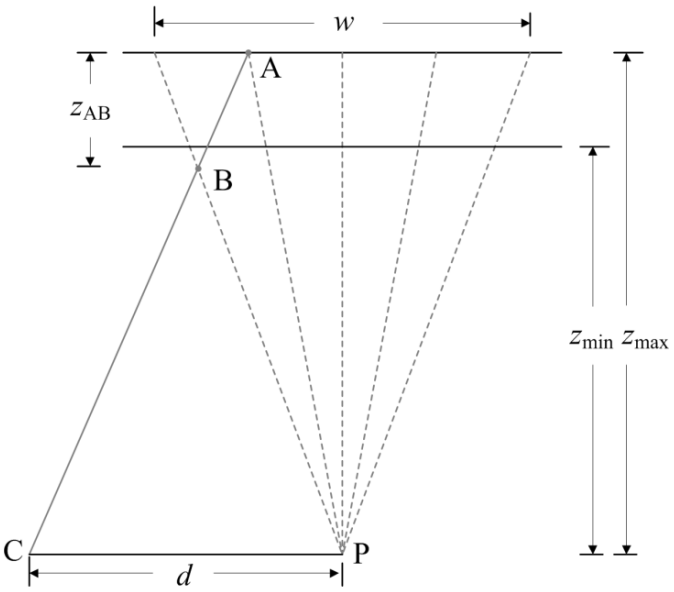

Figure 3.3. Diagram of geometric constraint for a single-camera single-projector setup.

Only the depth z_{AB} needs to be considered because B is the nearest candidate to A. If $z_{max} - z_{min} < z_{AB}$ is satisfied, the other candidates would be out of the measurement volume, and therefore be considered false. Thus, depth z_{AB} can be used to roughly determine the valid measurement volume. In this way, during measurement, for each "line of sight", there is only one valid candidate inside the measurement volume, and the true candidate is thus selected.

3.2 Experiments and Results

To test the new method, an experimental system was developed consisting of one monochrome camera (Point Grey FL3-U3-13S2M) and one DLP projector (Optoma PK301), with resolutions 1280×960 and 848×480, respectively. After gamma correction prior to fringe pattern projection [30], the camera-projector response was linear in the normalized intensity range [0.05, 0.80]. Since it was desired that the normalized intensities of the projected fringe patterns be in this range (Figure 3.2), the background and amplitude parameters were assigned as follows: $a_1 = 0.50$, $a_2 = 0.35$, and $b = 0.15$ (Table 3.1), so that the maximum normalized intensity was $a_1 + 2b = 0.50 + 2(0.15) = 0.80$, and the minimum

normalized intensity was $a_2 - 2b = 0.35 - 2(0.15) = 0.05$. The projected fringe pattern had 48 periods. The system was calibrated based on a stereovision model [116].

The measurement accuracy of the method was first evaluated by measurement of a double hemisphere, which had true radii of 50.800 ± 0.015 mm, based on manufacturing specification and precision. One of the four captured images encoded with the modulated background and amplitude is shown in Figure 3.4a. The extracted background intensity A_1 and the amplitude intensity after background removal are shown in Figure 3.4b and c, respectively. The wrapped phase map obtained by Eq. (3.3) is shown in Figure 3.4d. The identified phase orders, before and after applying phase-order correction, are shown in Figure 3.4e and f, respectively. The phase orders in most regions were assigned correctly, although some errors may remain in low-contrast or shadow regions. While the projected fringe pattern had 48 periods, the maximum identified phase order was 12. The wrapped phase map is then partially unwrapped from forty-eight periods to four wrapped periods, as shown in Figure 3.4g. The geometric constraints were therefore used to solve the remaining phase-order ambiguity. The depth of the system measurement volume was estimated based on the distance between the camera and projector (approximately 220 mm), maximum depth (1000 mm), and the width of the projector FOV at maximum measurement depth (600 mm). According to Eq. (3.12), the minimum measurement depth should be larger than 600 mm. The depth of the measurement volume was therefore approximately 400 mm. After removing all false candidates of points on the object surface, the final 3D reconstructed point cloud was obtained for the double hemisphere (Figure 3.4h).

The measurement accuracy of the new method was determined by least-square fitting of a sphere to each point-cloud hemisphere. The calculated radii of the two hemispheres was 50.723 mm and 50.797 mm, compared to the true radius 50.8 mm. The sphere-fitting standard deviations were 0.083 mm and 0.086 mm, respectively. The root mean square (RMS) errors based on differences between a measured point on the hemisphere and the true radius were 0.136 mm and 0.143 mm, respectively. The accuracy was largely dependent on the wrapped phase calculation, system calibration, and gamma correction. Ideally, the

modulated background and amplitude in the method would not influence the accuracy of the wrapped phase. However, sensitivity of the method to projector and camera focus may lead to phase error in the wrapped phase.

Measurement was also performed on a plastic mask and manikin head using the new method. One of the captured mask images is shown in Figure 3.5a, with the 3D reconstructed point cloud in Figure 3.5b, and 3D shaded polygonized mesh in Figure 3.5c without smoothing. The manikin head (Figure 3.6a) was measured from two different viewpoints, and the raw 3D reconstruction results without smoothing are shown in Figure 3.6b and c from the two viewpoints. These results demonstrate the ability of the new method to perform 3D shape measurement with only four projected patterns and captured images.

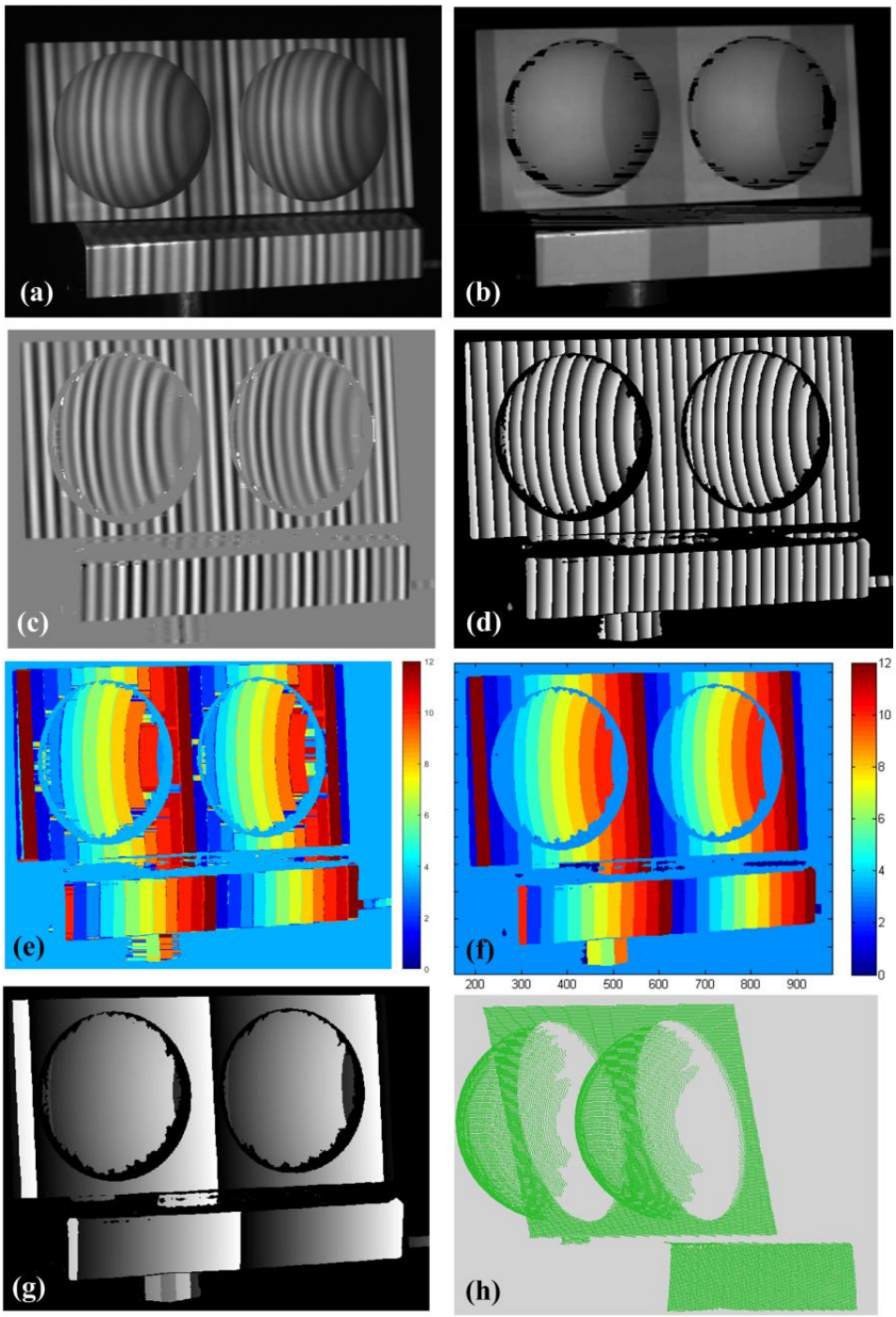

Figure 3.4. Experimental result of measurement of double-hemisphere object: (a) one of the captured images, (b) extracted background intensity, (c) amplitude intensity after background removal, (d) wrapped phase map, (e) identified phase orders before correction, (f) identified phase orders after correction, (g) partially unwrapped phase map, and (h) 3D reconstructed point cloud.

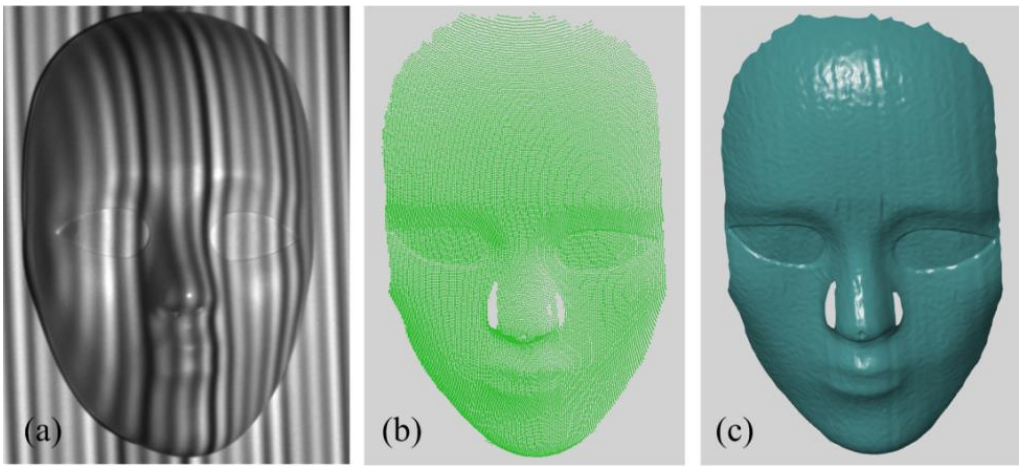

Figure 3.5. 3D measurement result of plastic mask: (a) one of the captured images, (b) 3D reconstructed point cloud, and (c) 3D shaded polygonized mesh.

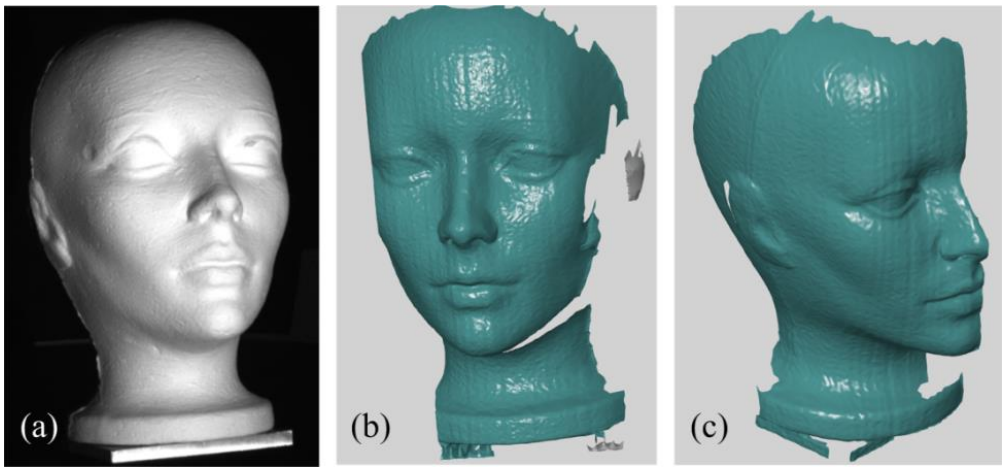

Figure 3.6. 3D measurement result of manikin head: (a) manikin head, and (b)-(c) 3D shaded polygonized meshes measured from two different viewpoints.

3.3 Discussion

A novel method for 3D shape measurement using background and amplitude encoded fringe patterns was developed. In this method, only four high-frequency fringe patterns are required for performing a 3D surface-shape measurement, using a single camera and projector. Although the phase orders of high-frequency fringe patterns were assigned correctly in most regions, using the new background and amplitude assignment and extraction method and application of geometry constraints, some errors occur in low-contrast and shadow regions,

resulting in incorrect selection of the corresponding point. These errors can be corrected using the phase order correction method based on a region growing algorithm. Some limitations of the method are that the phase order correction is time-consuming and would limit the ability of this method in real-time measurement, and the amplitude of the phase-shifted fringe patterns in some periods is adjusted to a low value ($b = 0.15$), which reduces the signal-to-noise ratio (SNR) of the phase-shifted patterns. An alternative approach that avoids the time-consuming post-processing of fringe order determination would be preferable for real-time measurement.

Chapter 4
High-Frequency Background Modulation Fringe Pattern Method

To improve the measurement accuracy and reliability of corresponding-point selection, and to simplify fringe encoding, a new fringe projection method that modulates background alone and uses four high-frequency fringe patterns is developed in this chapter. An optical system using two cameras and one projector is used. A novel model that relates the fringe wavelength to system-geometry constraints is developed to determine the highest pattern frequency that allows only two candidate points in the measurement volume, in order to ensure high reliability in corresponding-point selection. Newly developed mathematical expressions of geometry-constraint parameters permit calculation of the parameters immediately after system calibration prior to measurement, thus permitting use of a stored look-up table (LUT) to reduce computational cost during the measurement. In this method, 3D reconstruction can be performed pixel-wise, to enable measurement of objects with surface discontinuities.

4.1 Principle and Method

4.1.1 Background Modulation Fringe Patterns

In this method, the four-step phase-shifting method is used, and the phase-shifted patterns are encoded with different background values for different phase periods. The intensities of four phase-shifted fringe patterns I_n (n = 1, 2, 3, 4) are given by the following equations:

$$\begin{aligned} I_1(x,y) &= A(x,y) + B(x,y)\cos\phi(x,y) + A_0(x,y), \\ I_2(x,y) &= A(x,y) + B(x,y)\cos\left[\phi(x,y) - \pi/2\right], \\ I_3(x,y) &= A(x,y) + B(x,y)\cos\left[\phi(x,y) - \pi\right] + A_0(x,y), \\ I_4(x,y) &= A(x,y) + B(x,y)\cos\left[\phi(x,y) - 3\pi/2\right], \end{aligned} \tag{4.1}$$

where $A(x, y)$ and $B(x, y)$ represent the background intensity and amplitude of modulation, respectively. $A_0(x, y)$ represents a background offset which changes values for different phase

periods. $A_0 = 0.2A$ when the phase period is odd, and $A_0 = -0.2A$ when the phase period is even. $\phi(x, y)$ represents the phase distribution (phase map) and can be computed by:

$$\phi(x,y) = \tan^{-1}\left[\frac{I_2(x,y) - I_4(x,y)}{I_1(x,y) - I_3(x,y)}\right]. \tag{4.2}$$

The wrapped phase map $\phi(x, y)$ in Eq. (4.2) is independent of the background offset. The background offset can be extracted by:

$$A_0(x,y) = \frac{I_1(x,y) + I_3(x,y) - I_2(x,y) - I_4(x,y)}{2}. \tag{4.3}$$

The background offset $A_0(x, y)$ is then binarized by using a threshold value of 0, generating a binary pattern $C(x, y)$, where $C(x, y) = 1$ when $A_0(x, y) \geq 0$, and $C(x, y) = 0$ when $A_0(x, y) < 0$. The binary pattern $C(x, y)$ can thus denote each neighbouring odd and even phase period for every camera pixel. The extraction of the binary pattern is simple; however, the binarization may have error at edges of sinusoidal fringes (edge points) since the extracted background offset $A_0(x, y)$ does not usually have a sharp cut-off, resulting in a mismatch between phase map and binary pattern. Therefore, a binary pattern correction is necessary.

4.1.2 Binary Pattern Correction

Since the wrapped-phase analysis is independent of the background offset, the wrapped phase map still has high accuracy and reliability and can be used to guide the binary pattern correction. The mismatch between wrapped phase map and binary pattern tends to occur at edge points and their neighbouring pixels within a 1-pixel distance. Three examples of phase map values and their corresponding binary pattern values when C changes from 0 to 1 are shown in Figure 4.1. The phase value ϕ jumps between (x, y) and $(x, y+1)$; however, the binary pattern C jumps between $(x, y-1)$ and (x, y) in Case 1 and between $(x, y+1)$ and $(x, y+2)$ in Case 3, resulting in mismatch between the phase map and binary pattern. Case 2 is

correct since the edges of the phase map and binary pattern are matched between (x, y) and (x, y+1). Similarly, the mismatch can happen when the binary pattern C changes from 1 to 0.

The correction of the binary pattern error is given as follows:

For each pixel (x, y):

1) IF $\phi(x, y) - \phi(x, y-1) < \pi$ AND $\phi(x, y+1) - \phi(x, y) < -\pi$ AND $\phi(x, y+2) - \phi(x, y+1) < \pi$:
   THEN the pixel is an edge point.

2) IF the pixel is an edge point:
   THEN $C(x, y) = C(x, y-1)$ and $C(x, y+1) = C(x, y+2)$.

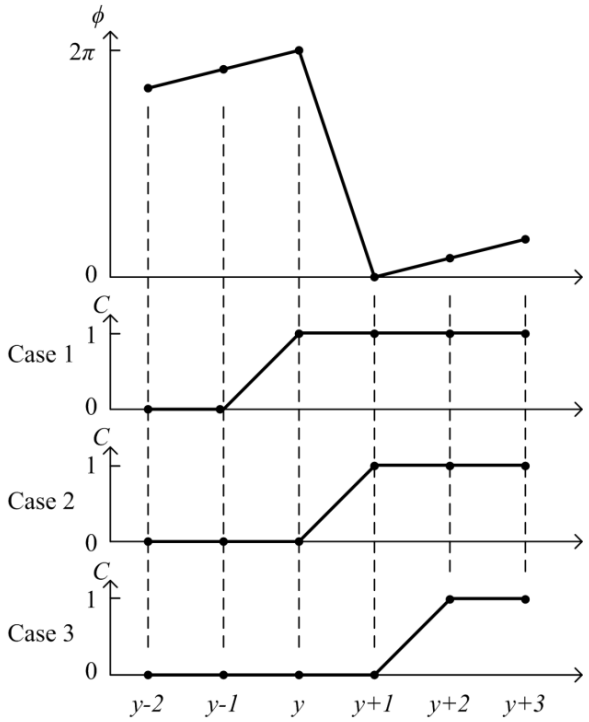

Figure 4.1. Examples of phase map values and their corresponding binary pattern values.

4.1.3 Geometry-Constraint Parameters

The method in this chapter was developed for a two-camera single-projector system (projector between cameras), as shown in Figure 4.2, where any two of the three devices form a standard stereovision system, since the projector can be regarded as an inverse

camera. Eq. (2.2) and (2.3) give the projection of any 3D world point coordinates (X^w, Y^w, Z^w) to the left-camera 3D camera coordinates (X^c, Y^c, Z^c), and from the left camera 3D coordinates to the left-camera normalized image-plane coordinates (x_n^c, y_n^c), respectively. All points imaged to the same left-camera normalized image-plane coordinates (x_n^c, y_n^c) lie on a straight line, the line of sight. The 3D world coordinates of points on the line of sight can be expressed by:

$$\begin{aligned} X^w &= \alpha_1 Z^w + \alpha_0, \\ Y^w &= \beta_1 Z^w + \beta_0, \end{aligned} \tag{4.4}$$

where:

$$\alpha_1 = \frac{\left(y_n^c l_{33} - l_{23}\right)\left(x_n^c l_{32} - l_{12}\right) - \left(y_n^c l_{32} - l_{22}\right)\left(x_n^c l_{33} - l_{13}\right)}{\left(y_n^c l_{32} - l_{22}\right)\left(x_n^c l_{31} - l_{11}\right) - \left(y_n^c l_{31} - l_{21}\right)\left(x_n^c l_{32} - l_{12}\right)}, \tag{4.5}$$

$$\alpha_0 = \frac{\left(y_n^c t_3 - t_2\right)\left(x_n^c l_{32} - l_{12}\right) - \left(y_n^c l_{32} - l_{22}\right)\left(x_n^c t_3 - t_1\right)}{\left(y_n^c l_{32} - l_{22}\right)\left(x_n^c l_{31} - l_{11}\right) - \left(y_n^c l_{31} - l_{21}\right)\left(x_n^c l_{32} - l_{12}\right)}, \tag{4.6}$$

$$\beta_1 = \frac{\left(y_n^c l_{33} - l_{23}\right)\left(x_n^c l_{31} - l_{11}\right) - \left(y_n^c l_{31} - l_{21}\right)\left(x_n^c l_{33} - l_{13}\right)}{\left(y_n^c l_{31} - l_{21}\right)\left(x_n^c l_{32} - l_{12}\right) - \left(y_n^c l_{32} - l_{22}\right)\left(x_n^c l_{31} - l_{11}\right)}, \tag{4.7}$$

$$\beta_0 = \frac{\left(y_n^c t_3 - t_2\right)\left(x_n^c l_{31} - l_{11}\right) - \left(y_n^c l_{31} - l_{21}\right)\left(x_n^c t_3 - t_1\right)}{\left(y_n^c l_{31} - l_{21}\right)\left(x_n^c l_{32} - l_{12}\right) - \left(y_n^c l_{32} - l_{22}\right)\left(x_n^c l_{31} - l_{11}\right)}, \tag{4.8}$$

Above, the *l* parameters are the elements of left camera rotation matrix in Eq. (2.2), and t_1, t_2 and t_3 are the elements of left camera translation matrix (vector), together comprising the left-camera extrinsic-parameter matrix. The projection of any 3D world point coordinates (X^w, Y^w, Z^w) to the projector normalized image plane can be computed by:

$$\begin{bmatrix} x_n^p \\ y_n^p \end{bmatrix} = \begin{bmatrix} X^p / Z^p \\ Y^p / Z^p \end{bmatrix} = \begin{bmatrix} \dfrac{p_1 Z^w + p_0}{s_1 Z^w + s_0} \\ \dfrac{q_1 Z^w + q_0}{s_1 Z^w + s_0} \end{bmatrix}, \tag{4.9}$$

where:

$$\begin{aligned} p_1 &= m_{11}\alpha_1 + m_{12}\beta_1 + m_{13}, \\ p_0 &= m_{11}\alpha_0 + m_{12}\beta_0 + t_4, \\ q_1 &= m_{21}\alpha_1 + m_{22}\beta_1 + m_{23}, \\ q_0 &= m_{21}\alpha_0 + m_{22}\beta_0 + t_5, \\ s_1 &= m_{31}\alpha_1 + m_{32}\beta_1 + m_{33}, \\ s_0 &= m_{31}\alpha_0 + m_{32}\beta_0 + t_6. \end{aligned} \tag{4.10}$$

Above, (x_n^p, y_n^p) are the projector normalized image plane coordinates. The *m* parameters are the elements of the projector rotation matrix in Eq. (2.4), and t_4, t_5 and t_6 are the elements of projector translation matrix (vector), together comprising the projector extrinsic-parameter matrix. For all points on the line of sight, the normalized projections on the projector image plane should lie on the projector epipolar line e_P. The equation of the projector epipolar line can be expressed by:

$$\left(q_1 s_0 - q_0 s_1\right) x_n^p + \left(p_0 s_1 - p_1 s_0\right) y_n^p + \left(p_1 q_0 - p_0 q_1\right) = 0\,. \tag{4.11}$$

After system calibration, the camera and projector extrinsic-parameter matrices are known. Thus, the parameters of the projector epipolar line can be pre-calculated using Eq. (4.11) (derivation explained in Appendix A), for each line of sight before measurement. Similarly, the parameters of the epipolar line on the right camera image plane e_{RC} can also be pre-calculated for every left-camera pixel. The pre-calculated parameters of the epipolar line on the projector and camera image planes are independent of phase map values and can be saved in LUTs. During object measurement, these parameters can be retrieved from the LUTs and used directly for the correspondence search on the epipolar line (see Appendix A), thus reducing the computational cost during the measurement.

4.1.4 Correct Corresponding Point Selection and Refinement using Geometry Constraint and Binary Pattern

For a fringe pattern with *K* phase periods, since the phase map obtained by Eq. (4.2) is wrapped, each line of sight will pierce through *K* equiphase planes, generating *K* candidate

points Q_i (i = 1, 2, … k, … K), as shown in Figure 4.2. (Candidate points for $i = k-1$, k, $k+1$, $k+2$ are explained further below). There is only one correct candidate located on the object surface; the other $K-1$ candidates are false. As the first step in selecting the correct candidate, a measurement volume (the region between two dashed lines, $Z_{\min} < Z^w < Z_{\max}$ in Figure 4.2) is used to exclude false candidates; all candidates outside the measurement volume are considered false. $Q_{\min}$ and $Q_{\max}$ are the intersections of the line of sight and the maximum and minimum measurement depth planes. If a high-frequency fringe pattern is used and the required capacity of measurement volume is large, there will still be several candidate points located in the measurement volume.

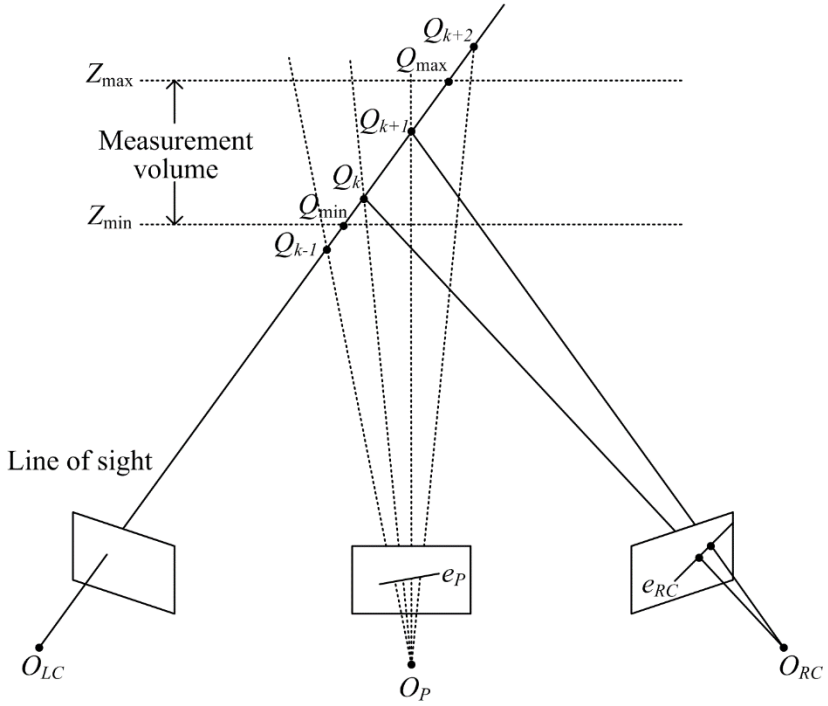

Figure 4.2. Diagram of geometry constraints and correspondence. (O_{LC}, O_P, and O_{RC}, represent the left camera, projector, and right camera centres; e_P and e_{RC} are the projector and right camera epipolar lines; and Q_{k-1},… Q_{k+2} represent points on the line of sight).

To further determine the correct candidate in the measurement volume, the binary pattern $C(x, y)$ is used. The method in this chapter allows only two candidates Q_k, Q_{k+1} to be located in the measurement volume by restricting the fringe-pattern wavelength (explained further in

Section 4.1.5). The binary pattern can uniquely denote each neighbouring odd and even phase period. If $C(x, y) = 1$, the correct phase period is odd; if $C(x, y) = 0$, the correct phase period is even. The correct candidate, either Q_k or Q_{k+1}, can thus be selected based on the value of $C(x, y)$ (note that $C(x, y)$ was based only on the encoded background intensity). The correct candidate is then projected onto the right-camera image plane. The ideal projection P_R onto the right-camera image plane, which is the corresponding point of the left-camera image point, should lie on the right-camera epipolar line e_{RC}. However, the computed corresponding-point P_R' may not lie on e_{RC} because of calibration errors of the left camera and projector, and phase errors (Figure 4.3).

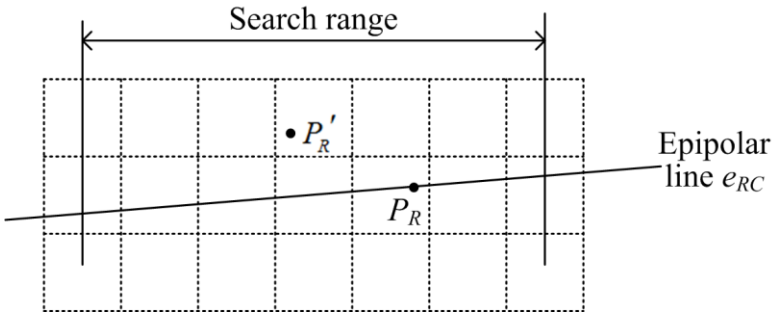

Figure 4.3. Corresponding-point refinement on the right-camera image plane (7×3 image region). P_R' represents the computed corresponding-point before refinement and P_R represents the refined corresponding-point.

Correspondence refinement is performed by searching for the corresponding point P_R on the right-camera epipolar line e_{RC}, which has the same phase value as the left-camera image point. To minimize computational cost, only a small segment of e_{RC} around the initially computed corresponding-point P_R' (within 3 pixels) is searched. Double linear interpolation is used to compute the refined corresponding-point at subpixel-level. The phase values at edge points need to be adjusted when searching the epipolar line. The method of edge-point adjustment is detailed in [39]. In the new method of this chapter, since the epipolar line e_{RC} is pre-calculated, and furthermore, only one candidate remains, the computational cost of correspondence refinement during measurement is reduced. After accurate corresponding points are found by the above correspondence refinement for every left-camera image point,

accurate 3D coordinates can be obtained, and the object surface reconstructed using stereovision 3D reconstruction techniques based on the left and right camera.

Corresponding-point selection and refinement can be summarized by the following steps:

1) Limit candidate points to within the measurement volume, *i.e.* $Z_{\min} < Z^w < Z_{\max}$.
2) Select correct candidate Q_k or Q_{k+1}, based on $C(x, y)$: Phase period is odd if $C(x, y) = 1$ or even if $C(x, y) = 0$. Compute the projection of the selected candidate onto the right-camera image plane.
3) Adjust phase values at edge points.
4) Search for the corresponding point on epipolar line e_{RC}.

4.1.5 Fringe-Pattern Wavelength Selection

High-frequency fringe patterns are desired to avoid phase error. However, high-frequency patterns generate more candidate points in the measurement volume than low frequency patterns (Figure 1.9), tending to make the correct candidate selection unreliable and computationally expensive. As mentioned earlier, to ensure high reliability of the corresponding-point candidate selection (with the further benefit of minimal computational cost in finding the correct candidate), the maximum number of candidates allowed in the measurement volume is two. This limits the highest fringe-pattern frequency that can be used. The highest fringe-pattern frequency (smallest wavelength) that can be used is now theoretically determined. Let the maximum measurement depth $Z_{\max} = z$ and minimum measurement depth $Z_{\min} = -z$, with vertical fringe-pattern wavelength λ.

By Eq. (2.6), the projector-image pixel coordinates (u^p, v^p) can be expressed as:

$$\begin{bmatrix} u^p \\ v^p \\ 1 \end{bmatrix} = \begin{bmatrix} f_u^p & s^p & u_0^p \\ 0 & f_v^p & v_0^p \\ 0 & 0 & 1 \end{bmatrix} \begin{bmatrix} x_n^p \\ y_n^p \\ 1 \end{bmatrix}, \tag{4.12}$$

where f_u^p and f_v^p are the effective focal lengths of the projector; s^p is the skew factor of the projector; and (u_0^p, v_0^p) is the projector principal point. Since $Q_{\max}$ and $Q_{\min}$ are on the maximum and minimum measurement depth planes, respectively, the u (horizontal) axis pixel coordinate difference between the projections of $Q_{\min}$ and $Q_{\max}$ on the projector image can be expressed as:

$$u_{\max}^p - u_{\min}^p = f_u^p \left(\frac{p_1 Z_{\max} + p_0}{s_1 Z_{\max} + s_0} - \frac{p_1 Z_{\min} + p_0}{s_1 Z_{\min} + s_0} \right) = 2 f_u^p \frac{(p_1 s_0 - p_0 s_1) z}{s_0^2 - s_1^2 z^2} . \tag{4.13}$$

To ensure that only two candidate points are located in the measurement volume, the pixel coordinate difference is constrained by:

$$u_{\max}^p - u_{\min}^p < 2\lambda . \tag{4.14}$$

The smallest wavelength that can be used for the fringe patterns is thus:

$$\lambda_{\min} = f_u^p \frac{(p_1 s_0 - p_0 s_1) z}{s_0^2 - s_1^2 z^2} . \tag{4.15}$$

The smallest wavelength $\lambda_{\min}$ can be calculated at every camera pixel. In this new method developed here, the maximum value over all pixels of the smallest wavelength, $\max\{ceil[\lambda_{\min}(x, y)]\}$ is used to generate the smallest wavelength, and thus highest frequency, permitted for the fringe patterns that satisfies the coordinate-difference constraint of Eq. (4.14) for all pixels. (*ceil*[ ] is the ceiling operator that gives the nearest upper integer number; and max{ } yields the maximum value over all pixels (x, y)).

4.1.6 Calibration of Two-Camera Single-Projector System

A two-camera single-projector system with geometry-constraint based techniques was developed as part of this method. The 3D measurement accuracy depends on the quality of the phase maps and the accuracy of the calibration of the two cameras performed with correspondence refinement. Projector calibration is only required to determine the candidate points Q_i (Figure 4.2). After the correct candidate is determined, its 3D coordinates are back-

projected onto the right-camera image plane and refined based on epipolar geometry using the right-camera phase map (Section 4.1.4). The distance between the computed corresponding-point P_R' and the true corresponding-point P_R on the epipolar line e_{RC} depends on the projector calibration accuracy (Figure 4.3). A distance of a few pixels will permit fast and correct correspondence refinement. However, the calibration of the projector is error prone in a camera-projector stereo system with a short baseline [58]. Therefore, the camera calibration parameters can be used to calibrate and optimize the projector calibration parameters.

The system calibration procedure is given as follows:

1) Determine the intrinsic parameters of each camera (left and right) and projector individually [55].
2) Determine the extrinsic parameters of the two cameras. Re-optimize the intrinsic and extrinsic parameters of the two cameras by minimizing the reprojection error for both cameras [53].
3) Determine the extrinsic parameters of the projector, based on the left-camera projector stereo system using the optimized left-camera parameters.
4) Re-optimize the projector intrinsic and extrinsic parameters, based on the left-camera projector stereo system, by minimizing the projector reprojection error.

4.1.7 Summary of Method

The 3D surface-shape measurement using high-frequency background-modulation fringe patterns is summarized as follows:

1. Prior to measurement:

a) Perform system gamma calibration and correction [30] and stereovision system calibration (Section 4.1.6).
b) Determine the smallest fringe wavelength (Section 4.1.5).

c) For every camera pixel (usually left camera), compute the corresponding epipolar lines on projector and right camera image planes (Section 4.1.3).

2. During measurement:

a) Project the four background modulation fringe patterns onto the surface. Capture fringe pattern images and perform lens distortion correction (Section 4.1.1).

b) Compute the wrapped phase maps.

c) Compute the binary patterns after fringe analysis for both cameras (Sections 4.1.1, 4.1.2).

3. 3D surface-shape reconstruction:

a) For every pixel in one camera, compute the corresponding-point candidates using the wrapped phase map and pre-calculated epipolar line (Section 4.1.4).

b) Eliminate false corresponding-point candidates using the binary pattern (Section 4.1.4).

c) Perform correspondence refinement (Section 4.1.4).

d) Compute 3D coordinates at all camera pixels based on stereovision techniques.

4.2 Experiments and Results

An experimental system was developed consisting of two monochrome cameras (Basler acA1300-200um) and one DLP projector (Optoma PK301), with resolutions 640×480 and 848×480, respectively. The extrinsic and intrinsic parameters of the projector and cameras were obtained by system calibration (Section 4.1.6). The measurement volume depth was set to 200 mm (z = 100 mm). By first calculating the smallest wavelength of the fringe pattern at every camera pixel using Eq. (4.15), the maximum smallest wavelength over all pixels and thus resulting wavelength to use for the fringe patterns was determined to be 21 pixels. Four high-frequency phase-shifted background modulation fringe patterns were generated with a 21-pixel wavelength (approximately 40 periods per pattern).

The measurement accuracy of the method was first evaluated by measurement of a double hemisphere object. One of the four high-frequency phase-shifted background modulation fringe patterns is shown in Figure 4.4a. The wrapped phase map obtained by Eq. (4.2) is shown in Figure 4.4b. The computed binary pattern $C(x, y)$ is shown in Figure 4.4c. The correspondence search and refinement were then performed directly along the pre-calculated epipolar lines for each pixel. Finally, the 3D reconstructed point cloud was obtained, as shown in Figure 4.4d.

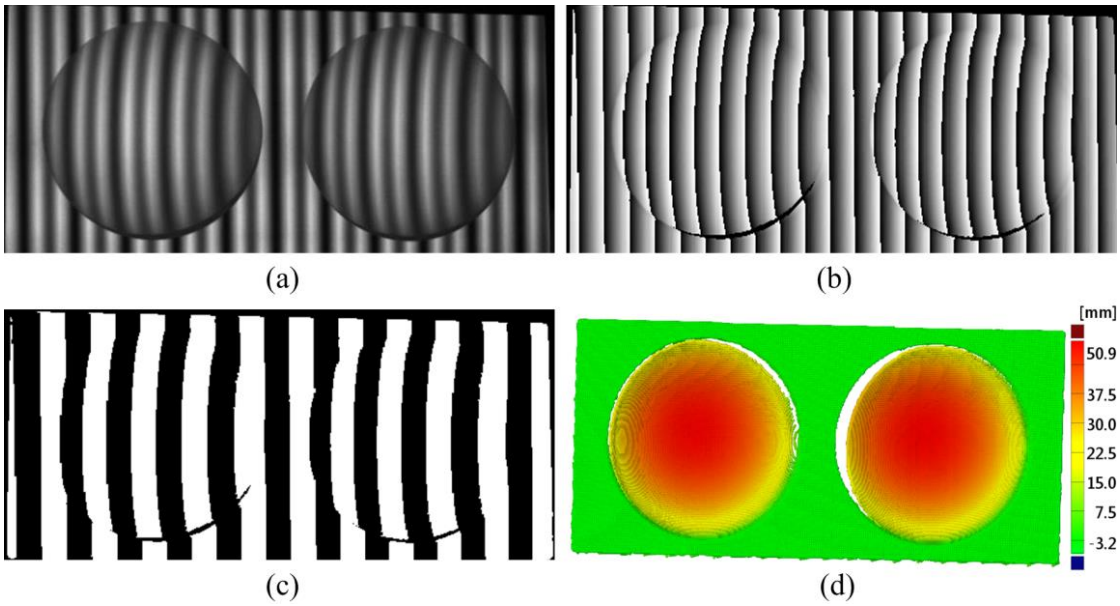

Figure 4.4. Experimental result of measurement of double-hemisphere object: (a) one of the captured images, (b) wrapped phase map, (c) computed binary pattern, and (d) 3D reconstructed point cloud.

The measurement accuracy of the new method was determined by least-square fitting of a sphere to each hemisphere point cloud. The calculated radii of the two hemispheres were 50.741 mm and 50.775 mm, compared to the true radius 50.800 ± 0.015 mm. The sphere-fitting standard deviations (SD) were 0.045 mm and 0.041 mm, respectively. The RMS errors based on differences between measured points on the hemisphere and the true radius were 0.063 mm and 0.060 mm, respectively. The distance between the two calculated sphere centres was 120.073 mm, compared to the true distance 120.000 ± 0.005 mm. The

measurement accuracy was quite excellent because of the high-frequency fringe patterns and high SNR of the wrapped phase map. The measurement accuracy of the new two-camera single-projector geometry constraint method (this chapter) even using cameras with lower resolution, was generally higher than that for the single-camera single-projector geometry constraint method (Chapter 3) (measured radii 50.723 mm and 50.797 mm, sphere-fitting SD 0.083 mm and 0.086 mm, respectively, RMS errors 0.136 mm and 0.143 mm, respectively). This may largely be because the measurement accuracy depends on the calibration accuracy of two cameras, but not on the projector calibration accuracy, in the new method of this chapter. In the single-camera single-projector method of Chapter 3, the measurement accuracy depends on both camera and projector calibration accuracies, and the projector calibration accuracy is generally lower than camera calibration accuracy.

The new method was also compared to measurement by a conventional three-frequency phase-shifting method, performed on the double hemisphere object using 12-, 13-, and 14-pixel pitch, and a total of twelve projected and captured fringe patterns. The conventional multi-wavelength 12-pattern method had nearly identical calculated radii 50.741 mm and 50.760 mm, lower sphere-fitting standard deviations 0.024 mm and 0.027 mm, lower RMS errors 0.039 mm and 0.040 mm, and identical sphere centre distance 120.073 mm. The measurement accuracies of the new method and conventional multi-wavelength phase-shifting method were both excellent. The new method had slightly higher RMS error and standard deviation, likely because of the limitation on the highest fringe-pattern frequency (smallest wavelength) that can be used. The new method has the advantage of using only four fringe patterns compared to the 12 patterns of the three-wavelength method. This advantage would be desirable when acquisition speed is important, such as for real-time measurement and measurement of moving or deforming surfaces, considering that the measurement accuracy is still excellent.

Measurement with the new method was also performed on an object with surface discontinuity, a curling stone handle. One of the four high-frequency phase-shifted background modulation fringe patterns is shown in Figure 4.5a, the wrapped phase map and

binary pattern in Figure 4.5b and c, and the 3D reconstructed point cloud in Figure 4.5d. The measurement results show that the new method, which performs all calculations pixel-wise, can handle objects with surface discontinuities.

A further measurement with the new method was performed on spatially isolated objects, a mask and cylinder, shown in Figure 4.6a. The 3D reconstructed point cloud in Figure 4.6b shows that the new method can handle measurement of separate object surfaces. Some small regions on the reconstructed mask were missing due to occlusion from one camera, which is a common problem for geometry-constraint based systems using two cameras [85].

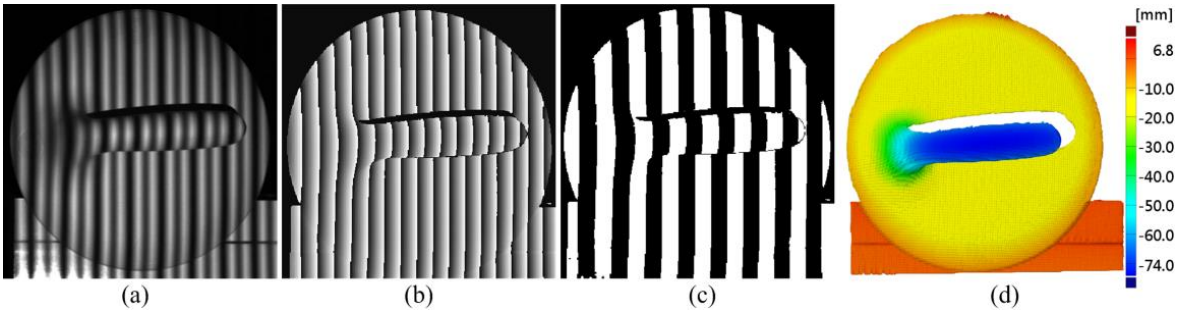

Figure 4.5. 3D measurement of curling-stone handle: (a) one of the captured images, (b) computed wrapped phase map, (c) computed binary pattern, and (d) 3D reconstructed point cloud.

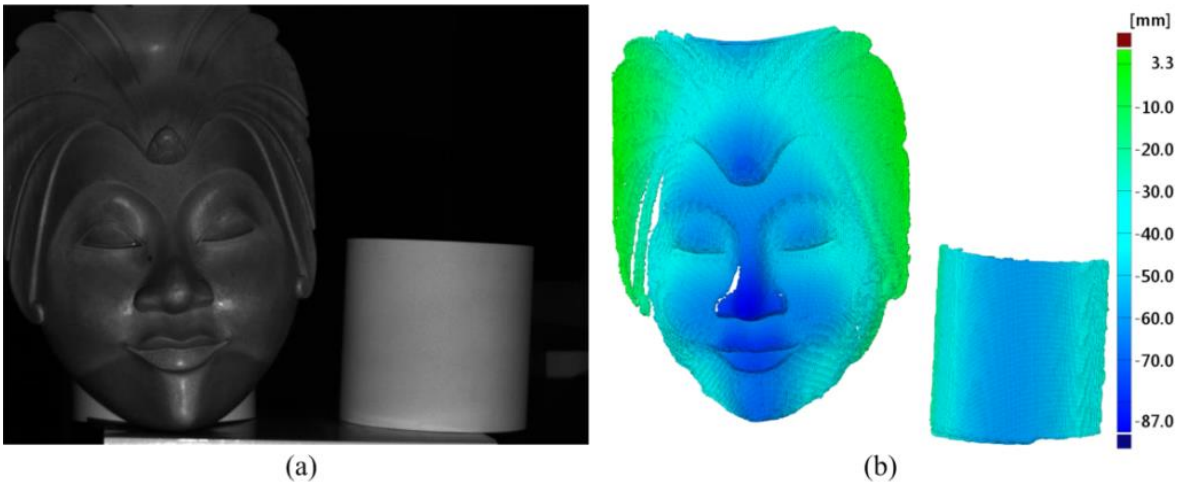

Figure 4.6. 3D measurement of spatially isolated objects: (a) mask and cylinder, and (b) 3D reconstructed point cloud.

To evaluate the performance of the new method on objects of varying surface reflectivity, a flat board with discontinuously varying gray levels (Figure 4.7a) and a flat board with continuously varying gray levels (Figure 4.7d) were measured using the new method and the standard 4-step phase-shifting method. The plane fitting residual errors of the 3D reconstructed point cloud for measurement of the discontinuous gray level surface (Figure 4.7a), are shown for the new method in Figure 4.7b, and for the 4-step PSP in Figure 4.7c, and for measurement of the continuous gray level surface (Figure 4.7d) for the new method in Figure 4.7e and PSP in Figure 4.7f. Periodic errors can be seen for both the new method and PSP in Figure 4.7b and c, respectively, at abrupt changes in surface reflectivity, which cause sudden contrast changes in captured images. Similar errors have been found at boundaries of high surface-reflectivity gradient in [117,118], possibly due to blending of light at the light-dark interfaces in the sampling of image-pixel intensities during image capture. Higher errors occur in darker regions, where image contrast in the captured fringes pattern images is low, as typical in 3D measurement systems. The new method works well in lighter high-contrast regions for the continuous gray level surface, where fewer errors are seen in left half region of Figure 4.7e. Higher errors can be seen in the darker region (right side) for both new and PSP methods (Figure 4.7e and f), which is typical for 3D measurement systems [117,119,120]. The measurement accuracy of the new method is more sensitive to surface-reflectivity gradient, likely due to the background modulation, where the errors appear in low contrast dark regions.

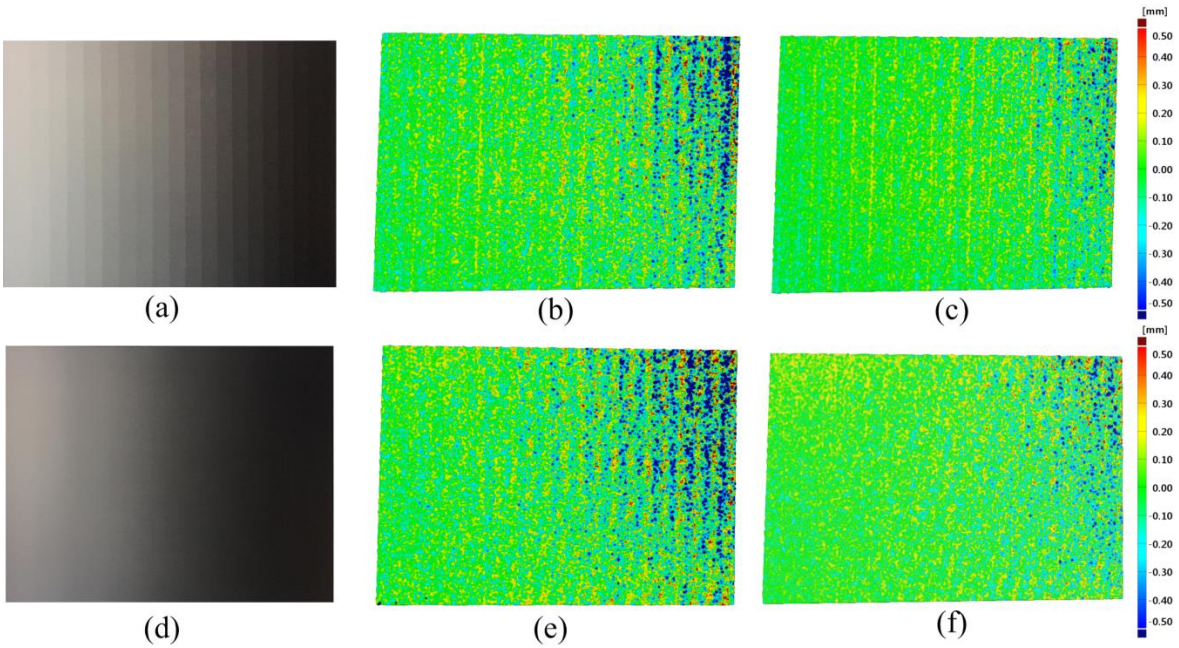

Figure 4.7. 3D measurement of objects of varying surface reflectivity: (a) flat board with discontinuously varying gray levels; (b-c) plane fitting residual errors of 3D reconstructed point cloud of (a) using (b) the new method, and (c) standard 4-step phase-shifting method; (d) flat board with continuously varying gray levels, (e-f) plane fitting residual error of (d) using (e) the new method, and (f) standard 4-step phase-shifting method.

4.3 Discussion

A novel method of 3D surface-shape measurement that uses high-frequency background-modulation fringe patterns generated based on a new fringe-wavelength geometry-constraint model was developed. The model determines the highest pattern frequency that can be used for the measurement and limits the number of candidate-points located in the measurement volume to two, thus permitting reliable corresponding-point selection, and minimal computational cost. Calculation of the epipolar line prior to measurement further reduces the computational cost of the measurement. Experiments demonstrated the ability of the method to perform full-field static 3D shape measurement with high-accuracy, for a surface with geometric discontinuity, and for spatially isolated objects. Computation is performed pixel-wise and is thus promising for parallel computing and real-time measurement. Since four fringe patterns are still required, the effect of object surface motion would need to be

considered for dynamic measurement and real-time applications. Methods that can further reduce the number of fringe patterns required for 3D reconstruction would be useful for real-time measurement, and techniques to compensate for motion artifacts would be useful if object surface motion were introduced.

Chapter 5
Real-Time 3D Surface-Shape Measurement using Background-Modulated Modified Fourier Transform Profilometry

This chapter presents a new real-time 3D measurement method that uses new background-modulated modified FTP fringe patterns and geometry constraints. Compared to the previous method using four background-modulated phase-shifted fringe patterns (Chapter 4), the background-modulated modified FTP reduces the required number of fringe patterns to two for 3D surface reconstruction. A short camera-projector baseline is used to allow only two candidate points in the measurement volume for reliable corresponding-point selection, even with high-frequency fringe patterns.

5.1 Principle and Method

5.1.1 Modified FTP

The modified FTP method uses two sinusoidal fringe patterns with a π phase-shift difference to remove the background intensity component [26]. The fringe patterns are given by the following equations:

$$I_1(x,y) = A(x,y) + B(x,y)\cos\phi(x,y), \tag{5.1}$$

$$I_2(x,y) = A(x,y) + B(x,y)\cos\left[\phi(x,y) - \pi\right], \tag{5.2}$$

where $A(x, y)$ and $B(x, y)$ represent the background intensity and amplitude of modulation, respectively, and $\phi(x, y)$ is the phase map. Subtracting two fringe patterns leads to

$$I_1 - I_2 = 2B(x,y)\cos\phi(x,y). \tag{5.3}$$

Similar to the standard FTP, a bandpass filter can be applied in the frequency domain to retrieve the wrapped phase map. For the modified FTP, the process is applied as follows:

$$\phi(x,y) = \tan^{-1}\left[\frac{\Im\left(F^{-1}\left\{\bar{F}\left[F\left(I_1 - I_2\right)\right]\right\}\right)}{\Re\left(F^{-1}\left\{\bar{F}\left[F\left(I_1 - I_2\right)\right]\right\}\right)}\right]. \tag{5.4}$$

where $\Im()$ and $\Re()$ denote the imaginary and real part of a complex variable, respectively; $F()$ and $F^{-1}()$ represent the 2D Fourier transform and inverse Fourier transform, respectively; and $\bar{F}$ denotes the filtering process. Since the background component is eliminated in the modified FTP, the retrieved phase map has better quality than the standard single-shot FTP method.

5.1.2 Background-Modulated Modified FTP

In Chapter 4, background modulation was developed for four high-frequency phase-shifted fringe patterns. In this chapter, a novel approach is used, where the modified FTP equations, Eqs. (5.1) and (5.2), form an odd set of fringe patterns, and background-modulated modified FTP equations, Eqs. (5.5) and (5.6), form an even set of fringe patterns using a similar background offset as in Chapter 4:

$$I_1'(x,y) = A(x,y) + B(x,y)\cos\phi(x,y) + A_0(x,y), \tag{5.5}$$

$$I_2'(x,y) = A(x,y) + B(x,y)\cos\left[\phi(x,y) - \pi\right] + A_0(x,y), \tag{5.6}$$

where the background offset A_0 has different values for different phase periods. $A_0 = 0.3A$ when the phase period is odd, and $A_0 = -0.3A$ when the phase period is even (Figure 5.1). The background offset can provide additional information for selection of the correct corresponding-point during correspondence matching, without affecting the extracted phase map. The bandpass filter used to obtain the fundamental frequency component in this method is designed by a 2D asymmetric window.

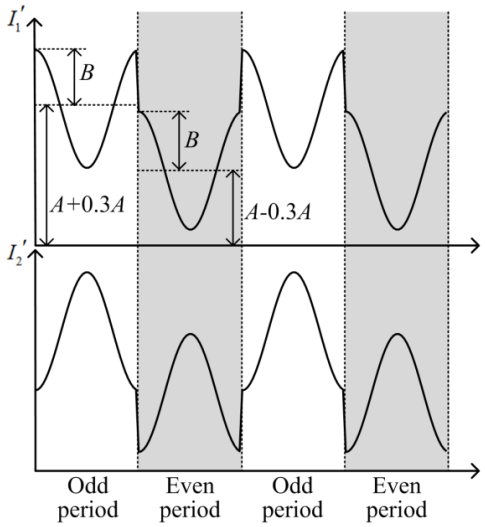

Figure 5.1. Normalized intensities of two background-modulated modified FTP fringe patterns, I_1', I_2', for four phase periods.

5.1.3 Continuous-Measurement Framework of Background-Modulated Modified FTP Method

For continuous real-time measurement (Figure 5.2), the even set (background-modulated modified FTP and odd set (modified FTP) of fringe patterns are projected alternately (Figure 5.2a). Left camera images (Figure 5.2a) and right camera images (Figure 5.2e) are simultaneously captured, and a wrapped phase map can be extracted from each set of left-camera fringe images (Figure 5.2b) and right-camera fringe images (Figure 5.2d). Only the left camera images are used for background offset computation.

The background offset can be extracted by using two sequential (current and previous) sets of fringe images (four images total):

$$A_0(x,y) = \frac{I_1'(x,y) + I_2'(x,y) - I_1(x,y) - I_2(x,y)}{2}. \tag{5.7}$$

The background offset $A_0(x, y)$ is binarized using a threshold value of 0, thus generating a binary pattern (Figure 5.2b). Since the extracted background offset does not usually have a sharp cut-off, the binarization could have some error at edge points (between neighboring phase periods, shown in Figure 5.1), resulting in a mismatch between the wrapped phase map

and binary pattern. A binary pattern correction can be applied to eliminate mismatches, by adjusting the binary pattern value at edge points based on the wrapped phase map, using the method in Section 4.1.2. After correction, the binary pattern can denote each neighboring odd and even phase period for every camera pixel, to enable correct selection of the corresponding point (detailed in Section 4.1.4) (Figure 5.2b). Although two sets of fringe images are required for background offset extraction, for continuous 3D surface measurement, one of the sets would already be acquired in a previous surface measurement. Therefore, only one newly acquired set of fringe images (two images) is required for background offset extraction in continuous real-time 3D measurement. Note that background offset binary patterns do not affect measurement accuracy, since they are only used in corresponding point selection, and not in 3D reconstruction.

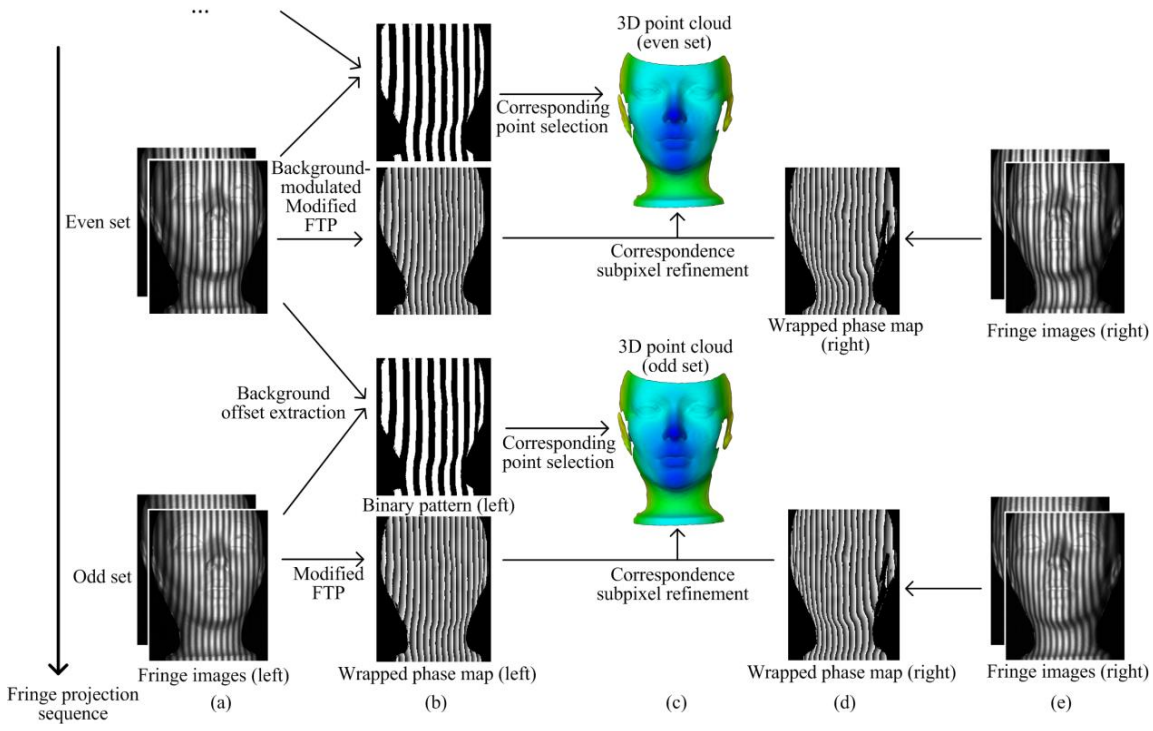

Figure 5.2. Fringe projection framework for the background-modulated modified FTP method, showing: (a) even set and odd set fringe images captured by left camera; (b) corresponding calculated phase map and binarized background offset pattern; (e) even set and odd set fringe images captured by right camera, captured simultaneously with images in (a); (d) calculated phase map (for right camera); and (c) reconstructed 3D point cloud.

For continuous 3D surface measurement, the 3D reconstruction requires only an even set or only an odd set of fringe images. 3D reconstruction is performed on each image set as follows. Once system calibration is performed, for each set of fringe images, either background-modulated modified FTP (even set) or modified FTP (odd set), the left-camera phase map and computed binary pattern can be used to determine left-camera to projector correspondence; a selected corresponding point can then be refined (Figure 5.2c) using the right-camera phase map (Figure 5.2d); and the resulting 3D point cloud can be computed (Figure 5.2c) using stereovision 3D reconstruction techniques. Therefore, only one newly acquired set of fringe images is required for surface reconstruction for continuous real-time 3D measurement. Compared to the method in Chapter 4, the number of images required to compute the phase map and 3D surface reconstruction is reduced by half, which is important for dynamic measurement.

In this new method, the left-camera-projector baseline is reduced by placing the camera as close as physically possible beside the projector. The model that relates fringe wavelength to system-geometry constraints (Eq. (4.15)), developed in Chapter 4, is then used to determine the smallest fringe-pattern wavelength that will allow only two neighboring candidate points (Q_k and Q_{k+1}) in the measurement volume. The utilization of the small left-camera projector baseline avoids the use of a greater fringe-pattern wavelength and smaller size of measurement volume, which would be alternative methods to achieve only two neighboring candidate points in the measurement volume. For the two candidate points (Q_k and Q_{k+1}) in the measurement volume, each has one corresponding-point candidate on the projector epipolar line. One of these corresponding-point candidates would be located in an odd phase period, with the other corresponding-point candidate in an even phase period. The selection of the correct corresponding-point for the left-camera pixel is determined as follows. The corresponding-point in an odd phase period is selected when the binarized background offset A_0 at the left-camera pixel is 1; and the corresponding-point in an even phase period is selected when the binarized background offset is 0.

5.2 Experiments and Results

To verify the performance of the new background-modulated modified-FTP geometry-constraint method, an experimental system was developed consisting of two monochrome cameras (Basler acA1300-200um) using 720×540 images and a DLP projector (Wintech PRO4500) with 912×1140 resolution. The left camera was positioned as close as possible beside the projector, with a short baseline distance of 57.3 mm. The baseline distance between the left and right cameras was 163.7 mm. The working distance of the system from the object was approximately 700 mm. The system was calibrated using the method described in Section 4.1.6. The range of depth of the measurement volume was set to 200 mm, and the smallest fringe pattern wavelength that allowed two candidate points was calculated to be 20 pixels using the method in Section 4.1.5.

5.2.1 Measurement of Static Objects

The measurement accuracy of the new method was first evaluated by measurement of the same double hemisphere object used in Chapter 3 and Chapter 4. Four fringe patterns were projected onto the object, first an even set of two background-modulated modified FTP fringe patterns, and then an odd set of two modified FTP fringe patterns, as in Figure 5.2. The even sets of the background-modulated modified FTP fringe patterns are shown in Figure 5.3a and b. The computed binary pattern is shown in Figure 5.3c. Wrapped phase maps were computed using the even set, then the odd set. The wrapped phase map computed using the two background-modulated modified FTP fringe patterns (even set) is shown in Figure 5.3d. Then 3D reconstructions were performed on both the even set and odd set, and also using the PSP method of Chapter 4, for comparison with the same optico-geometrical setup. The measurement accuracy was determined by least-square fitting of a sphere to each hemisphere point cloud. For the new method, the 3D reconstructed point cloud using the even set phase map is shown in Figure 5.4a, and sphere-fitting residual error in Figure 5.4b.

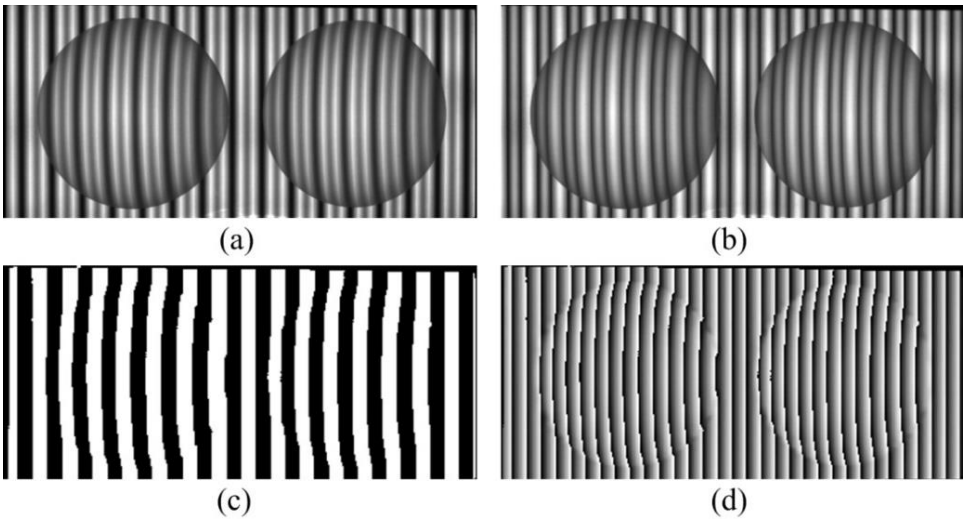

Figure 5.3. Experimental results of measurement of a static double-hemisphere object using the new method: (a)-(b) two captured background-modulated modified-FTP images (even set), (c) computed binary pattern, and (d) wrapped phase map.

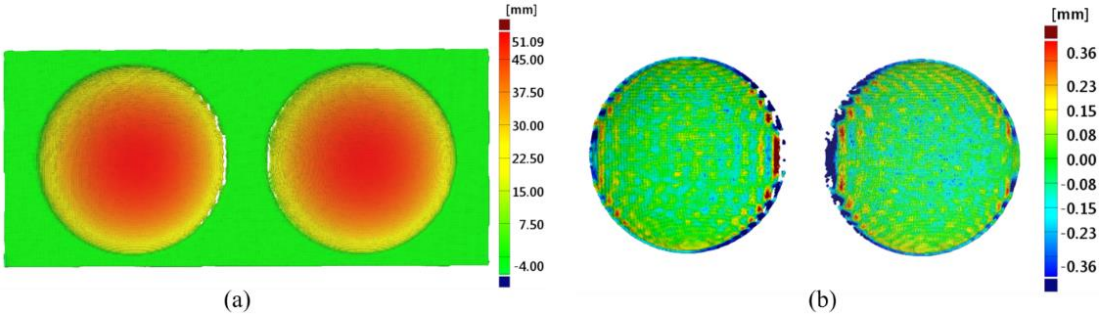

Figure 5.4. 3D reconstruction result of static double-hemisphere object measurement using the new method: (a) 3D reconstructed point cloud, and (b) sphere-fitting residual error.

The measurement accuracy for 3D reconstruction was computed for the new background-modulated modified-FTP method for the even set, odd set, and previous background-modulation PSP method (Chapter 4) for comparison. The calculated radii of the two hemispheres, distance between two sphere centres, RMS error based on differences between measured points on the hemisphere and the true radius, and sphere-fitting standard deviation (SD), are shown in Table 5.1. The reconstructed point clouds for both the even and odd sets using the background-modulated modified-FTP method had high measurement accuracy. Since the errors were similar for the even and odd sets for the new method, the embedded

background offset seems to have little negative effect on the phase map quality. However, as expected, the new method had slightly higher RMS error and sphere-fitting SD than the background-modulated PSP method for a static measurement, because the phase map quality obtained from FTP is generally worse than for PSP [87]. The sphere-fitting residual error on the hemisphere edge is larger than in the central region (Figure 5.4), because the object has a high slope on the edge, which exceeds the finite measurement range (slope) of the modified FTP, as commonly occurring [26].

Table 5.1. Static measurement results for the new background-modulated modified FTP method and background-modulated PSP method (Chapter 4).

	Background-modulated modified-FTP (Even set)	Background-modulated modified-FTP (Odd set)	Background-modulated PSP
Radii of two spheres (mm)	[50.756, 50.678]	[50.749, 50.681]	[50.813, 50.741]
Distance between sphere centres (mm)	120.104	120.105	120.125
RMS error (mm)	[0.116, 0.111]	[0.113, 0.110]	[0.061, 0.061]
Sphere-fitting SD (mm)	[0.078, 0.076]	[0.076, 0.076]	[0.043, 0.044]

5.2.2 Measurement of moving objects

For measurement of moving objects, the new background-modulated modified-FTP method, which used two image frames for 3D reconstruction was expected to have an advantage over the PSP-based method, which used four images. The measurement accuracy was evaluated by measurement of a double hemisphere object moving horizontally with an approximately speed of 25 cm/s, using both methods. For direct comparison between the two methods, four fringe patterns (consisting of one even set and one odd set) with $\pi/2$ phase shift added to the odd set, were projected onto the moving double hemisphere object, for the background-modulated PSP method. For the new method, a 3D point cloud was reconstructed using only two images (even set); and for the background-modulated PSP method, a 3D point cloud was reconstructed using all four images. The 3D polygonised mesh results in Figure 5.5, show

motion artifacts in the form of ripples for the four-image PSP-based method (Figure 5.5b) with a smoother surface for the new method (Figure 5.5a). The measurement accuracy for the dynamic measurement of the moving object, determined in the same manner as for the static object (Section 5.2.1), was better for the new method compared to the PSP-based method (Table 5.2). RMS errors for the new method (0.125 mm) were approximate half of the error for the PSP-based method, 0.25 mm. The smaller surface errors of the new method are seen in the smaller sphere-fitting residual error for the new method (Figure 5.5c) compared to the higher errors and ripples shown for the background-modulated PSP method (Figure 5.5d).

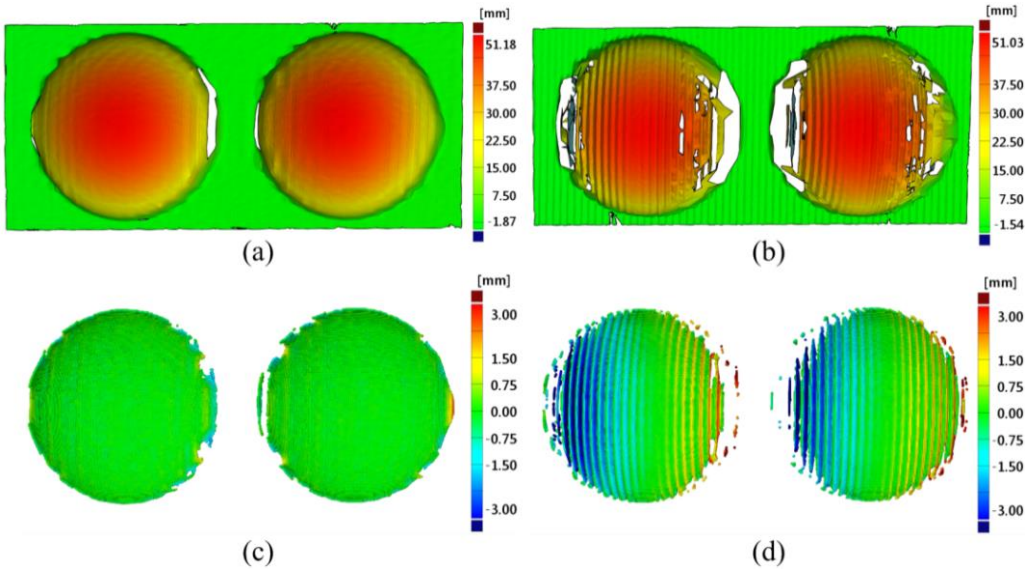

Figure 5.5. Experimental results of measurement of moving double-hemisphere object: 3D polygonized meshes from (a) new method and (b) background-modulated PSP method; sphere-fitting residual from (c) new method and (d) background-modulated PSP method.

Table 5.2. Dynamic measurement results for the new and background-modulated PSP methods.

	New background-modulated modified-FTP	Background-modulated PSP
Radii of two spheres (mm)	[50.814, 50.755]	[50.759, 50.631]
Distance between sphere centres (mm)	120.131	120.169
RMS error (mm)	[0.125, 0.124]	[0.252, 0.250]
Sphere-fitting SD (mm)	[0.084, 0.077]	[0.144, 0.144]

5.2.3 Real-time measurement

To verify the real-time performance of the system using the new method, measurements were performed on a desktop computer with a NVIDIA GeForce GTX1080ti graphic card and an Intel i7-3820 processor with the two-camera single-projector system. Four fringe patterns were pre-stored in the projector and then projected sequentially as in Figure 5.2 with an exposure time of 8.33 ms for each pattern. Both cameras were synchronized with the projector. To minimize the computation by the GPU, system calibration and geometric parameters were pre-calculated and stored on the GPU.

A moving and deforming hand was measured by the system. The 3D reconstruction of a point cloud and display were performed in real-time with image capture. The display includes lighting and rendering, with colour display blue to red representing near to far, as shown in Figure 5.6. The average number of reconstructed points was 100K. The mean GPU runtime of a single 3D reconstruction including memory transfer between host and device was approximately 10 ms, which was less than the acquisition time (camera capture) of two fringe patterns. The total time for a single 3D reconstruction and rendering was approximately 20 ms, corresponding to a 3D display rate of 50 fps.

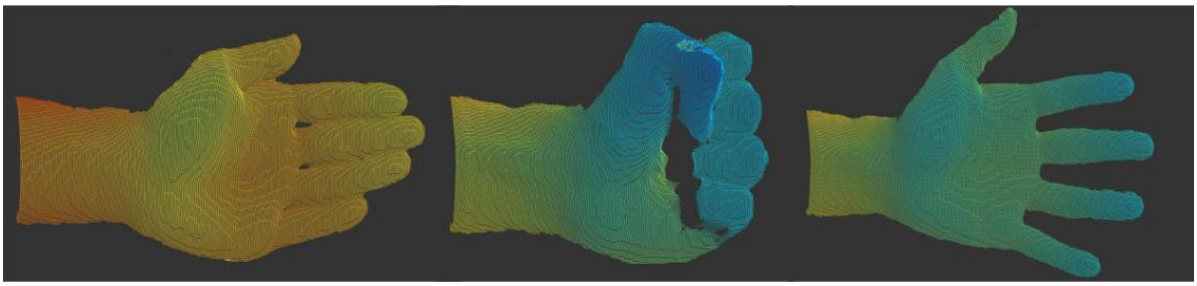

Figure 5.6. Dynamic measurement results of a moving and deforming hand.

5.3 Discussion

A new method of real-time 3D surface measurement was developed using background-modulated modified FTP fringe patterns and geometry-constraint techniques. The background-modulated modified FTP method uses only two high-frequency fringe patterns for a single 3D reconstruction from phase maps and achieved real-time measurement with

full 3D surface reconstruction and rendering at 50 fps. The new two image-frame background-modulated modified FTP method has less motion artifact (higher measurement accuracy) for dynamic measurement than the four-image PSP-based method. The four-image PSP-based method had higher accuracy for static measurement than the two-image modified FTP method. For static surfaces, the PSP-based method can handle high depth variation better than the modified FTP method. A measurement approach that can preserve the advantage of four-image PSP for static measurement, but also compensate for motion artifacts for dynamic measurements, may achieve high accuracy for both static and dynamic measurement in real-time measurement.

Chapter 6
Real-Time Motion-Induced-Error Compensation Method

In the previous chapter, the background-modulated modified FTP method achieved real-time measurement with full 3D surface reconstruction, and less motion artifact (higher measurement accuracy) than the four-image PSP-based method for dynamic measurement. For static measurement, the PSP-based method had higher accuracy and handled surfaces with high depth variation better than the modified FTP method. This chapter presents a new approach that uses four images to achieve high accuracy for static measurement, but also compensates for motion-induced error for dynamic measurement. The new motion-induced-error compensation method is non-iterative to achieve low computational cost for real-time 3D measurement. The method performs pixel-wise estimation of the phase-shift due to surface motion without the assumption of homogeneous motion across the surface. To permit real-time measurement, system geometry-constraints are used to solve the phase ambiguity of the wrapped phase map without requiring additional patterns as in temporal phase-unwrapping methods.

6.1 Principle and Method

6.1.1 Phase-Shifting Method

In a generic phase-shifting method [42] using N sinusoidal fringe patterns with any phase shifts, the intensity of each pixel of camera-captured phase-shifted fringe images can be modeled by:

$$I_n(x,y) = A(x,y) + B(x,y)\cos[\phi(x,y) - \theta_n], \tag{6.1}$$

where $A(x, y)$ and $B(x, y)$ represent the unknown background intensity and amplitude of modulation, respectively, and $\phi(x, y)$ is the unknown phase map. θ_n (n = 1, 2, … N) is the known phase shift for the n-th projected fringe pattern. Eq. (6.1) can be rewritten as:

$$I_n(x,y) = A(x,y) + B_1(x,y)\cos(\theta_n) + B_2(x,y)\sin(\theta_n), \tag{6.2}$$

where $B_1(x, y) = B(x, y)\cos[\phi(x, y)]$ and $B_2(x, y) = B(x, y)\sin[\phi(x, y)]$. The following equation can be obtained:

$$\mathbf{X}(x,y) = \left(\mathbf{M}^T\mathbf{M}\right)^{-1}\mathbf{M}^T\mathbf{I}(x,y), \tag{6.3}$$

where $\mathbf{X}(x, y) = [A(x, y), B_1(x, y), B_2(x, y)]^{\mathrm{T}}$, $\mathbf{I}(x, y) = [I_1(x, y), I_2(x, y), ..., I_N(x, y)]^{\mathrm{T}}$, and

$$\mathbf{M} = \begin{bmatrix} 1 & \cos(\theta_1) & \sin(\theta_1) \\ 1 & \cos(\theta_2) & \sin(\theta_2) \\ \vdots & \vdots & \vdots \\ 1 & \cos(\theta_N) & \sin(\theta_N) \end{bmatrix}. \tag{6.4}$$

The wrapped phase can then be computed by:

$$\phi(x,y) = \tan^{-1}\left[\frac{B_2(x,y)}{B_1(x,y)}\right]. \tag{6.5}$$

Recall that for a standard 4-step phase-shifting method with phase shift $\theta_n = 2\pi(n-1)/N$, the wrapped phase can be computed by:

$$\phi(x,y) = \tan^{-1}\left[\frac{I_2(x,y) - I_4(x,y)}{I_1(x,y) - I_3(x,y)}\right] \tag{6.6}$$

6.1.2 Motion-Induced Phase Error

If the object is moving or deforming between successive captured images, the phase shift at each pixel in the captured images will have an additional unknown phase-shift due to the object surface motion. This phase-shift error can be determined pixel by pixel using the system geometric and optical parameters and object motion, if the motion is known [114]. The object motion induced phase-shift error for the standard 4-step phase-shifting method, where the object surface is moving toward the camera at varying speed, is shown in Figure 6.1. When capturing fringe images with phase-shift error due to motion, $I_1'(x,y)$,

$I_2'(x,y)$, $I_3'(x,y)$ and $I_4'(x,y)$, the position of the object surface for any camera pixel is at $p_1(x, y)$, $p_2(x, y)$, $p_3(x, y)$ and $p_4(x, y)$, respectively. Three unknown phase-shift errors $\varepsilon_1(x, y)$, $\varepsilon_2(x, y)$ and $\varepsilon_3(x, y)$ are caused by the object motion from p_1 to p_2, p_2 to p_3, and p_3 to p_4, respectively. Similar phase-shift errors can be observed, for any direction the object is moving in [109]. Since the position of the object is unknown and changing during the measurement, an object position $P(x, y)$ (red dashed line) that has zero phase-shift error (i.e. no motion-induced error), can be defined as a reference to aid in determining the phase-shift error in each image $I_n'(x,y)$ (n = 1, 2, 3, 4).

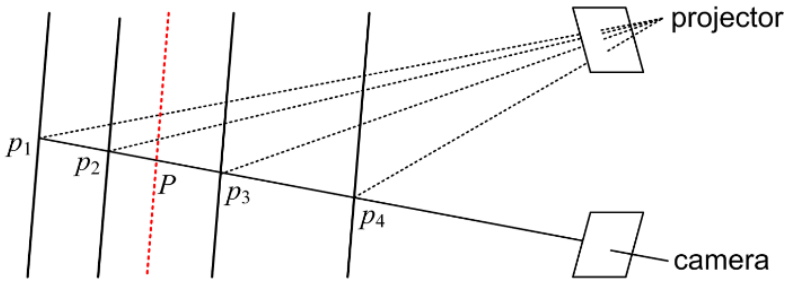

Figure 6.1. Object surface motion-induced phase-shift error.

It is assumed that the object moves in one direction during the image acquisition of four phase-shifted images, and that the position $P(x, y)$ is between the middle two positions p_2 and p_3, where the phase-shift error between positions p_2 and P is half the phase-shift error between p_2 and p_3, $\varepsilon_2(x, y)/2$. Note that P is not necessarily at mid-depth between p_2 and p_3.

The intensities of the 4-step phase-shifted fringe images considering object motion can be described by the following equations:

$$\begin{aligned}
I_1'(x,y) &= A(x,y) + B(x,y)\cos\left[\phi(x,y) - \varepsilon_2(x,y)/2 - \varepsilon_1(x,y)\right],\\
I_2'(x,y) &= A(x,y) + B(x,y)\cos\left[\phi(x,y) - \pi/2 - \varepsilon_2(x,y)/2\right],\\
I_3'(x,y) &= A(x,y) + B(x,y)\cos\left[\phi(x,y) - \pi + \varepsilon_2(x,y)/2\right],\\
I_4'(x,y) &= A(x,y) + B(x,y)\cos\left[\phi(x,y) - 3\pi/2 + \varepsilon_2(x,y)/2 + \varepsilon_3(x,y)\right].
\end{aligned} \tag{6.7}$$

$\phi(x, y)$ is the unknown phase related to the object surface geometry to be solved for. Since the motion-induced phase-shift errors are unknown, the wrapped phase $\phi'(x, y)$ given by the standard 4-step phase-shifting method:

$$\phi'(x, y) = \tan^{-1}\left[\frac{I_2'(x, y) - I_4'(x, y)}{I_1'(x, y) - I_3'(x, y)}\right], \tag{6.8}$$

will contain some motion-induced phase error $\Delta\phi(x, y)$:

$$\Delta\phi(x, y) = \phi'(x, y) - \phi(x, y). \tag{6.9}$$

Camera pixel coordinates (x, y) may be omitted hereinafter for brevity. Eq. (6.8) can be rewritten as:

$$\phi'(x, y) = \tan^{-1}\left[\frac{\sin\left(\phi - \varepsilon_2/2\right) + \sin\left(\phi + \varepsilon_2/2 + \varepsilon_3\right)}{\cos\left(\phi - \varepsilon_2/2 - \varepsilon_1\right) + \cos\left(\phi + \varepsilon_2/2\right)}\right]. \tag{6.10}$$

For a very small phase-shift error ε, $\sin(\varepsilon) \approx \varepsilon$ and $\cos(\varepsilon) \approx 1$. Then, Eq. (6.10) can be approximated as:

$$\phi'(x, y) \approx \tan^{-1}\left[\frac{2\sin\phi + \varepsilon_3\cos\phi}{2\cos\phi + \varepsilon_1\sin\phi}\right]. \tag{6.11}$$

The motion-induced phase error $\Delta\phi(x, y)$ (Eq. (6.9)) can be derived as:

$$\Delta\phi(x, y) = \tan^{-1}\left[\frac{\varepsilon_3\cos^2\phi - \varepsilon_1\sin^2\phi}{2 + \left(\varepsilon_1 + \varepsilon_3\right)\sin\phi\cos\phi}\right]. \tag{6.12}$$

By using Taylor series approximation, the motion-induced phase error can be further approximated as:

$$\Delta\phi(x, y) \approx \frac{\varepsilon_3 - \varepsilon_1}{4} + \frac{\varepsilon_3 + \varepsilon_1}{4}\cos 2\phi. \tag{6.13}$$

Full derivation of the motion-induced phase error for the 4-step phase-shifting method is detailed in Appendix B.

6.1.3 Simulation of Motion-Induced Phase Error

Eq. (6.13) shows that the motion-induced phase error approximately correlates to 2ϕ. The average phase error is close to zero if the object motion is at constant speed, where $\varepsilon_1(x, y) \approx \varepsilon_3(x, y)$. The phase error amplitude increases as phase-shift errors ε_1 and ε_3 increase. A phase measurement simulation was performed using a given phase-shift error between successive positions: $\varepsilon_1 = \varepsilon_2 = \varepsilon_3 = 0.2$ rad, and assuming constant speed motion. Four phase maps were simulated at four different positions p_1, p_2, p_3, p_4, based on Eq. (6.7). Note that the phase maps in this simulation are unwrapped. The phase map $\phi'(x, y)$ with motion-induced phase error, simulated using the standard 4-step phase-shifting method (Eq. (6.8)) (black curve), is shown with the simulated phase at the four positions p_1, p_2, p_3, p_4 (four coloured lines) in Figure 6.2a.

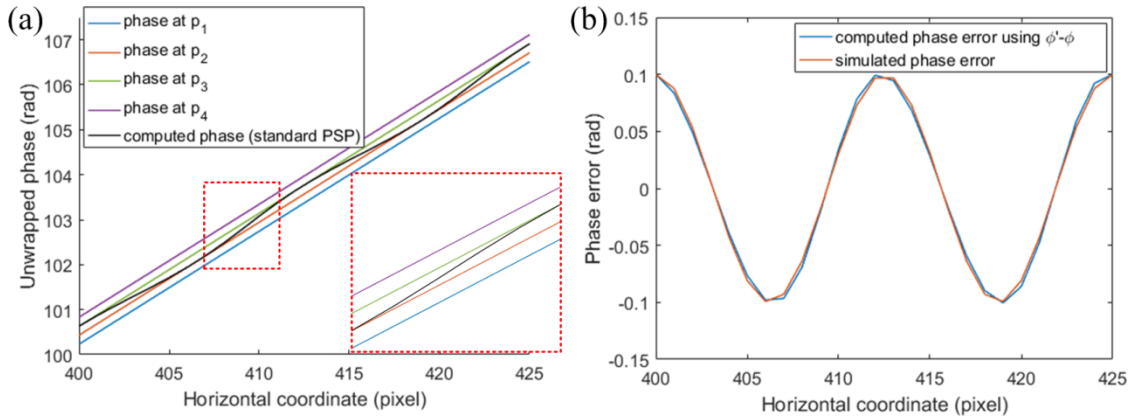

Figure 6.2. Phase measurement simulation with constant speed motion: (a) unwrapped phase computed by standard 4-step PSP (black) and phase at four positions p_1, p_2, p_3, p_4, (b) motion-induced phase error computed using $\phi'-\phi$ (blue) and simulated using Eq. (6.13) (red).

A phase map $\phi(x, y)$ without error is simulated by generating images using Eq. (6.7) and assuming that the object has no motion, thus using $\varepsilon_1 = \varepsilon_2 = \varepsilon_3 = 0$ rad. The computed motion-induced phase error using $\phi'-\phi$, and the simulated phase error using Eq. (6.13), are shown in Figure 6.2b.

A simulation of phase measurement with varying speed object motion was performed using a given phase-shift error between successive positions: ε_1 = 0.15 rad, ε_2 = 0.2 rad, and ε_3 = 0.25 rad. Four phase maps were simulated at four positions p_1, p_2, p_3, p_4, based on Eq. (6.7). The phase map $\phi'(x, y)$ with motion-induced phase error, simulated using the standard 4-step phase-shifting method (Eq. (6.8)) (black curve), is shown with the simulated phase at the four positions p_1, p_2, p_3, p_4 (four coloured lines) in Figure 6.3a. The computed motion-induced phase error (blue) using $\phi'-\phi$ and the simulated phase error (red) using Eq. (6.13) are shown in Figure 6.3b. The small difference between the computed and simulated phase curves in both Figure 6.2b and Figure 6.3b shows that the motion-induced phase error can be approximated by Eq. (6.13).

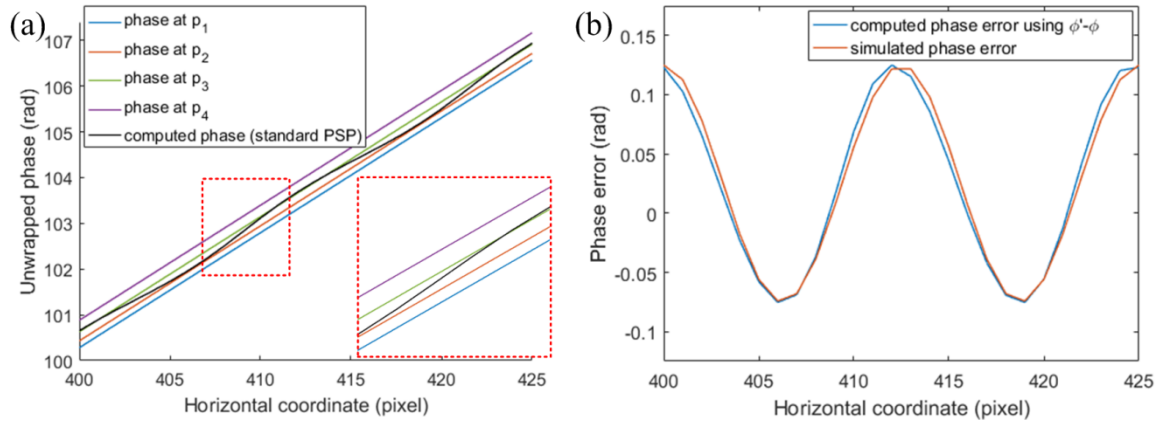

Figure 6.3. Phase measurement simulation with varying speed object motion: (a) unwrapped phase computed by standard 4-step PSP (black) and phase at four positions p_1, p_2, p_3, p_4, (b) motion-induced phase error computed using $\phi'-\phi$ (blue) and simulated using Eq. (6.13) (red).

6.1.4 Motion-Induced Phase-Shift Error Estimation

Although the wrapped phase can be obtained once the phase shift is known using the phase-shifting method (Section 6.1.1), the computed phase map will have unknown phase error (Section 6.1.2) from the additional unknown phase shift due to object surface motion. Determination of the unknown phase-shift error caused by object motion is key to retrieve the phase with no motion artifact. The approach in this new method is to compute three phase

maps at intervals over a multiple measurement sequence and estimate the phase-shift error by calculating the difference between the computed phase maps. To generate the three phase maps over the sequence, the standard 4-step phase-shifted images (frames) at p_1 to p_4 (Figure 6.1) are used together with the previous two frames at p_{-1} and p_0, and the subsequent two frames at p_5 and p_6, where the object is moving from position p_{-1} to position p_6 (Figure 6.4).

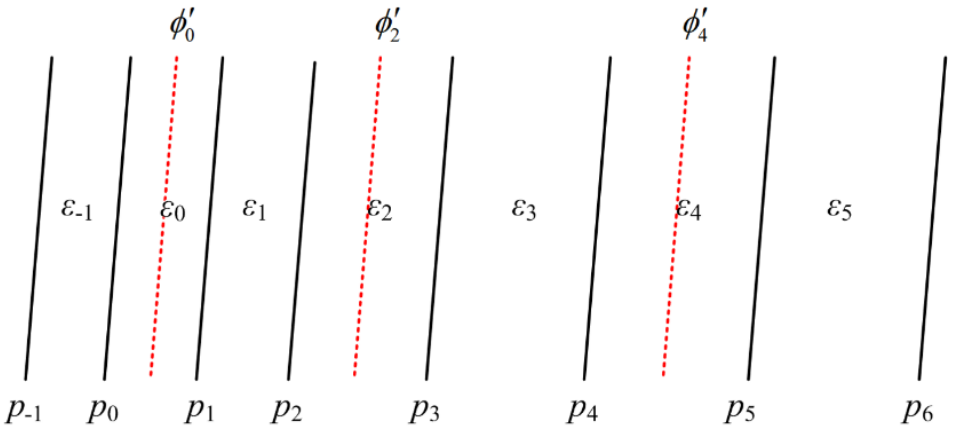

Figure 6.4. Object motion at eight successive frames and motion-induced phase-shift errors.

Consider a phase-shift error ε_i caused by object motion from any position p_i to the subsequent position p_{i+1} (Figure 6.4). While it is possible to compute five different phase maps ϕ'_k (k = 0, 1, 2, 3, 4), only ϕ'_0, ϕ'_2 and ϕ'_4 are used as discussed below. The phase maps ϕ'_0, ϕ'_2 and ϕ'_4 are each computed using four images captured at p_{-1}, p_0, p_1, p_2; p_1, p_2, p_3, p_4; and p_3, p_4, p_5, p_6; respectively, using the standard 4-step phase-shifting method for all three phase maps, and where ϕ'_2 is the phase map that is being corrected, for the current measurement. Referring to Figure 6.4, according to Eq. (6.13), the motion-induced phase error of phase map ϕ'_2 is:

$$\Delta\phi_2(x,y) \approx \frac{\varepsilon_3 - \varepsilon_1}{4} + \frac{\varepsilon_3 + \varepsilon_1}{4}\cos 2\phi_2 . \tag{6.14}$$

Similarly, the motion-induced phase error of phase map ϕ'_4 is:

$$\Delta\phi_4(x,y) \approx \frac{\varepsilon_5 - \varepsilon_3}{4} + \frac{\varepsilon_5 + \varepsilon_3}{4}\cos 2\phi_4 . \tag{6.15}$$

The difference of phase maps ϕ_2 and ϕ_4 consists of a default phase shift of $-\pi$ and a phase shift due to object motion:

$$\phi_4(x,y) - \phi_2(x,y) = -\pi + \varepsilon_3 + \left(\varepsilon_2 + \varepsilon_4\right)/2 . \tag{6.16}$$

For object motion at constant speed or constant acceleration, the following approximation holds for any successive three phase-shift errors:

$$\varepsilon_{i+2}(x,y) - \varepsilon_{i+1}(x,y) \approx \varepsilon_{i+1}(x,y) - \varepsilon_i(x,y) . \tag{6.17}$$

Although the computed phase maps ϕ_2' and ϕ_4' have phase error, the phase errors $\Delta\phi_2(x, y)$ and $\Delta\phi_4(x, y)$ will be similar according to Eq. (6.14) and (6.15), if the phase-shift errors are small. Calculating the difference of the two phase maps with similar phase error can partially cancel the effect of the phase error. Considering that there is a default phase shift of $-\pi$ between ϕ_2' and ϕ_4', computing the π offset phase difference $\phi_4' - \phi_2' + \pi$ gives:

$$\begin{aligned} \phi_4'(x,y) - \phi_2'(x,y) + \pi &= \left(\phi_4 + \Delta\phi_4\right) - \left(\phi_2 + \Delta\phi_2\right) + \pi \\ &\approx 2\varepsilon_3 + \frac{\varepsilon_4 - \varepsilon_2}{2}\cos\left(2\phi_2\right) - 2\varepsilon_3\varepsilon_4 \sin\left(2\phi_2\right). \end{aligned} \tag{6.18}$$

The average of $\phi_4' - \phi_2' + \pi$ (Eq. (6.18)) is approximately twice the phase-shift error ε_3. However, there is still a small additional sinusoidal error correlated to $2\phi_2$, which makes the estimation of the phase-shift error ε_3 inaccurate using $\phi_4' - \phi_2' + \pi$. A simulation of $\phi_4' - \phi_2' + \pi$ computed for different values of phase-shift error ε_3 = 0.1, 0.15 and 0.2 rad, is shown in Figure 6.5, for assumed constant speed object motion. As the phase-shift error ε_3 increases, the sinusoidal error increases, since the phase errors of phase maps ϕ_2' and ϕ_4' become more different.

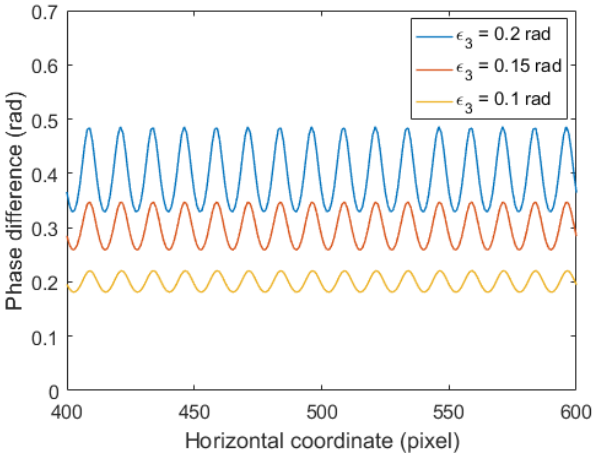

Figure 6.5. Simulation of the π offset phase difference of two phase maps with different phase-shift errors.

In this method, an averaging operation is further performed over a small region around each pixel after computing the offset phase difference $\phi_4' - \phi_2' + \pi$, to eliminate the additional sinusoidal error. Then, the phase-shift error $\varepsilon_3(x, y)$ can be estimated by:

$$\varepsilon_3(x, y) = \left\langle \frac{\phi_4' - \phi_2' + \pi}{2} \right\rangle_V . \tag{6.19}$$

Here $\langle \quad \rangle_V$ denotes an averaging operator over a small image region V around pixel (x, y). The window size of the small region is the wavelength of the projected fringe pattern. It would be computationally expensive if the above averaging operation were performed at each pixel. An integral image [121] is used to reduce the computational cost, making it suitable for parallel computing. Similarly, by computing the offset phase difference of phase maps ϕ_0' and ϕ_2', the phase-shift error $\varepsilon_1(x, y)$ can be estimated by:

$$\varepsilon_1(x, y) = \left\langle \frac{\phi_2' - \phi_0' + \pi}{2} \right\rangle_V . \tag{6.20}$$

Phase-shift error $\varepsilon_2(x, y)$ is estimated by $\varepsilon_2(x, y) = [\varepsilon_1(x, y) + \varepsilon_3(x, y)]/2$. After the estimates of ε_1, ε_2 and ε_3 are computed for each pixel, the wrapped phase $\phi(x, y)$, which has reduced

motion-induced phase error, can be obtained by the phase-shifting method Eqs. (6.1)-(6.5) (Section 6.1.1), where:

$$\begin{aligned}\theta_1(x,y) &= \varepsilon_2/2 + \varepsilon_1,\\ \theta_2(x,y) &= \pi/2 + \varepsilon_2/2,\\ \theta_3(x,y) &= \pi - \varepsilon_2/2,\\ \theta_4(x,y) &= 3\pi/2 - \varepsilon_2/2 - \varepsilon_3.\end{aligned} \tag{6.21}$$

It should be noted that a quality map [122] is used to determine a valid measurement region following computation of all phase maps above.

6.1.5 Unwrapped Phase Using Geometry-Constraints

The computed wrapped phase maps with reduced motion-induced phase error are used to determine the correspondence between a projector and a right and left camera, and geometry constraints are used to minimize the number of candidate points for correspondence, as described in Section 4.1.4. In this chapter, the number of candidate points in the measurement volume is reduced even further than in the earlier developed methods of Chapters 3-5. Here, the number of candidate points is minimized to only one by using a very short baseline between the left camera and projector. There is thus no need to embed additional information in the fringe patterns to achieve high correspondence reliability. The object surface shape can finally be reconstructed by stereovision techniques.

6.2 Experiments and Results

To verify the performance of the new motion-induced-error compensation method, an experimental system consisting of two monochrome cameras (Basler acA1300-200um) using 800×600 images and a DLP projector (Wintech PRO4500) with 912×1140 resolution was used. The left camera was placed beneath the projector to achieve a very short left-camera projector baseline (26.5 mm), while the camera-camera baseline was long (116.9 mm). The system was calibrated using the method described in Section 4.1.6. The working distance of the system from the object was approximately 700 mm. The image capture from the two

cameras was synchronized with the pattern projection, which had a speed of 120 Hz. The range of depth of the measurement volume used for geometry-constraint based phase unwrapping was set to 200 mm. The wavelength of the projected fringe patterns was set to 24 pixels.

6.2.1 Qualitative Evaluation

The performance of the motion-induced-error compensation method was first evaluated by measurement of a moving multi-step object (Figure 6.6a). The object was moved by hand during the measurement. The object motion consisted of both translation (in depth direction) and rotation. The first captured fringe image of the 4-step PSP method is shown in Figure 6.6b. The 3D measurement using the standard 4-step PSP method had large motion artifact in the form of ripples on the reconstructed surfaces on both the multi-step object and hand, as shown in Figure 6.6c. There was less motion artifact when using the new motion-induced-error compensation method (Figure 6.6d). The depth of points located on the red line segment (300th row) in Figure 6.6b without error compensation shows motion artifact in the form of ripples in Figure 6.7a. Using the new error compensation method, the motion artifact is again seen to be largely eliminated in the depth plot (Figure 6.7b).

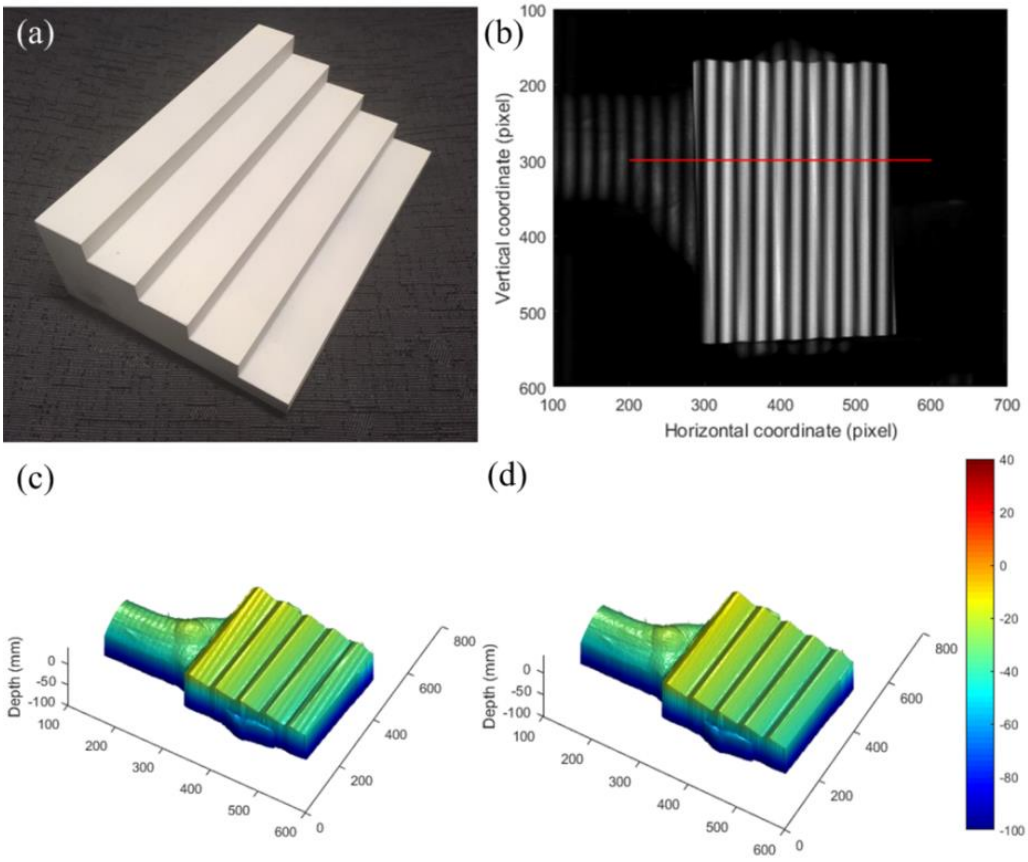

Figure 6.6. 3D measurement of moving multi-step object: (a) image of stepped object (b) one captured fringe image; (c) measurement result using standard 4-step PSP method; (d) measurement result using new motion-induced-error compensation method.

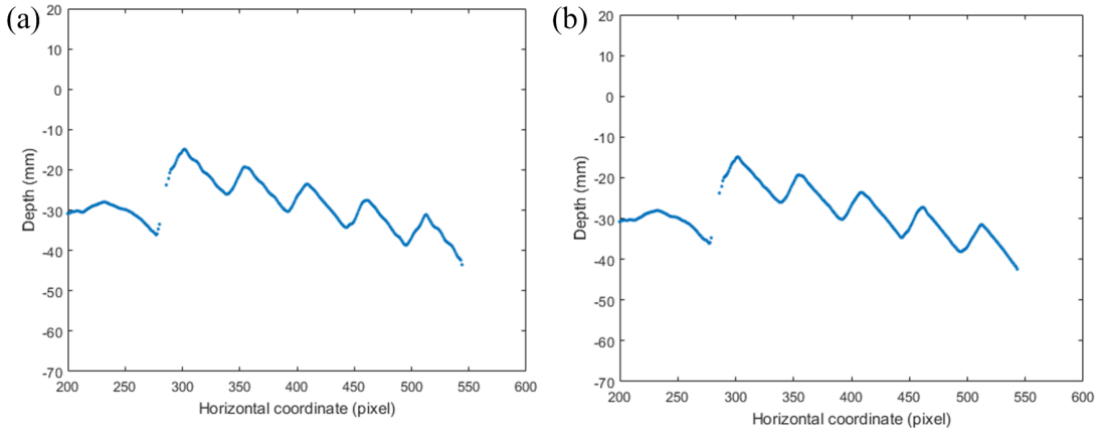

Figure 6.7. Depth of a row of points located on the red line segment in Figure 6.6b: (a) measurement result using standard 4-step PSP method; (b) measurement result using new motion-induced-error compensation method.

6.2.2 Quantitative Evaluation

To quantitatively evaluate the performance of the new motion-induced-error compensation method, the double hemisphere object was measured while it was moving with an approximate speed of 17 cm/s. The surface was reconstructed using the standard 4-step PSP method and the new error compensation method, respectively (Figure 6.8). The reconstructed surface had motion artifacts in the form of ripples for the standard measurement (Figure 6.8a), and less artifact when using the new error compensation method (Figure 6.8b).

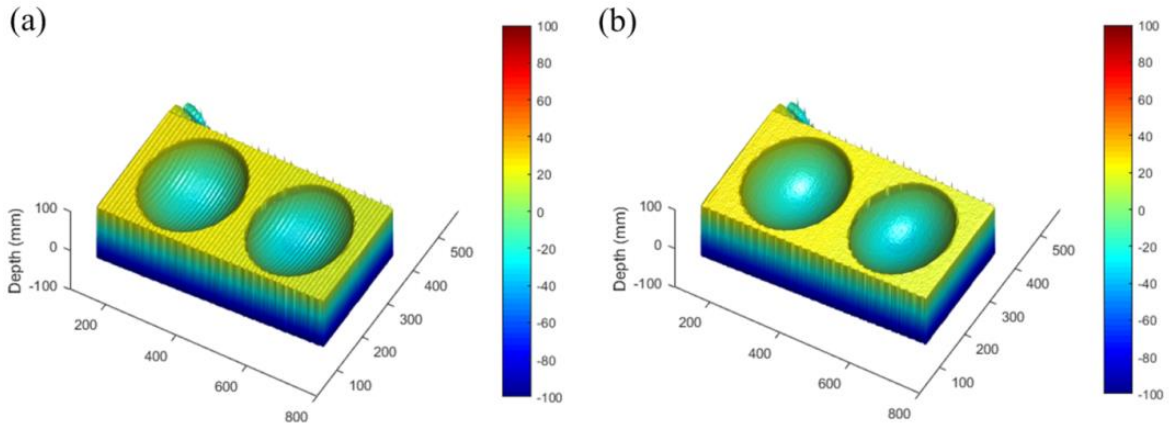

Figure 6.8. 3D measurement of moving double hemisphere object: (a) measurement result using standard 4-step PSP method; (b) measurement result using new motion-induced-error compensation method.

For comparison to the new error compensation method, in addition to measurement by the standard 4-step PSP method, a surface measurement was performed by a single-image real-time FTP method using only one of the four captured images. The measurement error for the three methods was determined by least-square fitting of a sphere to each 3D reconstructed hemisphere point cloud. The sphere-fitting residual errors (indicated by colour) for the new error compensation method were mostly under 0.1 mm (Figure 6.9c). These errors were lower than the errors for the standard 4-step PSP (Figure 6.9a), seen as ripples of multiple colours with errors as high as 0.5 mm, and lower than the errors for single-image FTP (Figure 6.9e), which were as high as 0.5 mm, mainly at the edges of the hemisphere. The measurement error distributions for the three methods in Figure 6.9b, d, and f, respectively,

show lower errors for the motion-induced-error compensation method (Figure 6.9d), compared to the other two methods (Figure 6.9b and f). Even with the use of multiple images in the new method, the error reduction is highly effective to bring the errors (Figure 6.9c and d) to a lower level than the errors for the single-image FTP (Figure 6.9e and f). As discussed earlier, measurement accuracy of the FTP method is limited where depth variation is large (Figure 6.9e), as seen at the outer edges, where errors are approximately 0.5 mm.

The calculated radii of the two hemispheres, distance between two sphere centres, RMS error based on differences between measured points on the hemisphere and the true radius, and sphere-fitting SD, are shown in Table 6.1 for the three measurement methods. The RMS errors and the sphere fitting SD were much lower using the new error compensation method compared to the standard PSP and single-image FTP methods. The uncorrected motion artifacts contribute to the higher RMS and SD errors of the standard PSP. The limited measurement accuracy at regions of large depth variation contributes to the higher error of the FTP method. The new error compensation method can reduce the motion-induced error and also handle the large depth variation of an object surface.

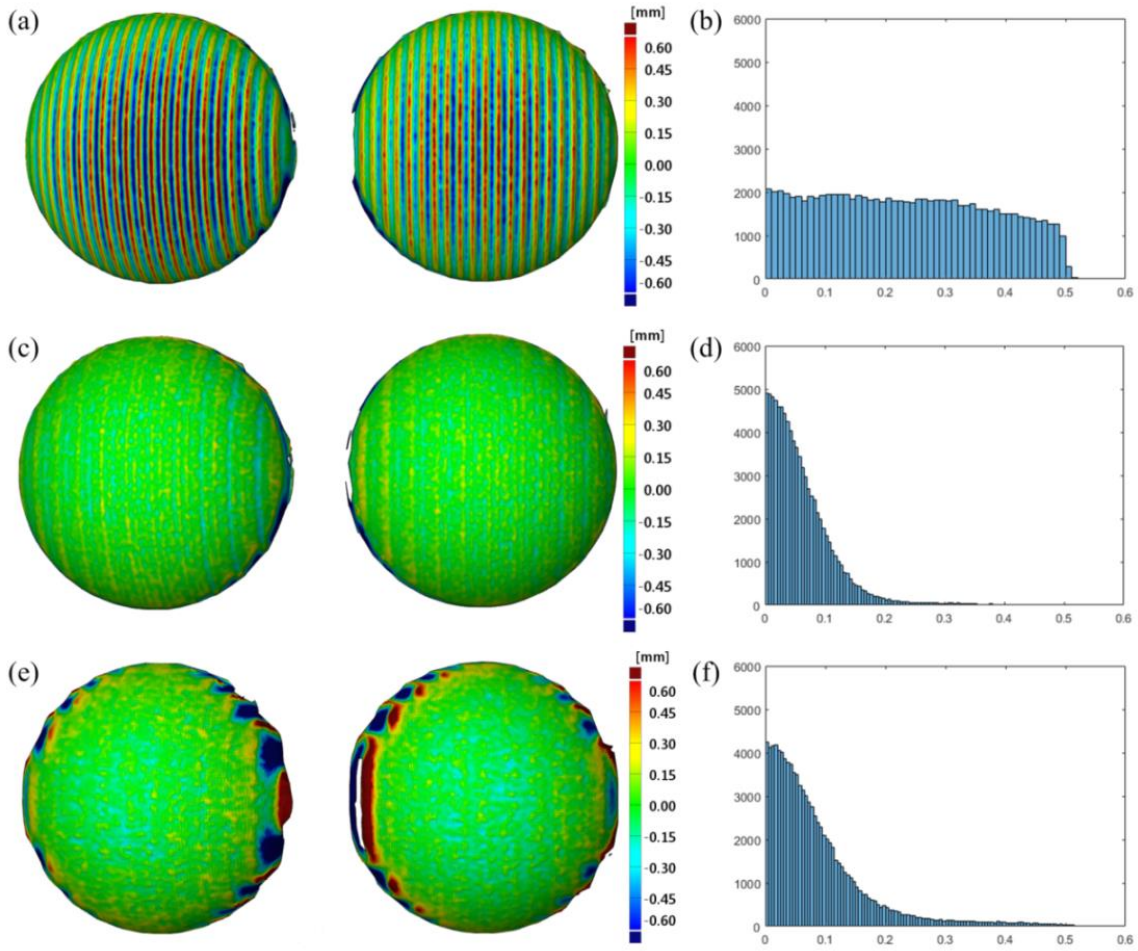

Figure 6.9. Errors in 3D measurement of a moving double-hemisphere object using: (a) standard 4-step PSP method, (c) new motion-induced-error compensation method, (e) single-image FTP method; and measurement error distribution (number of points versus error (mm) for the three methods: (b) standard 4-step PSP, (d) error compensation, and (f) single-image FTP.

Table 6.1. Measurement results for the standard PSP method, new motion-induced-error compensation method, and single-image FTP method.

	Standard PSP	New method	Single-image FTP
Radii of two spheres (mm)	[50.745, 50.689]	[50.765, 50.714]	[50.666, 50.689]
Distance between sphere centres (mm)	120.063	120.040	120.037
RMS error (mm)	[0.274, 0.272]	[0.088, 0.081]	[0.124, 0.124]
Sphere-fitting SD (mm)	[0.143, 0.139]	[0.060, 0.056]	[0.088, 0.086]

6.2.3 Real-Time Measurement

To verify the performance of the new motion-induced-error compensation method for real-time applications, real-time measurements were performed on a desktop computer with a NVIDIA GeForce GTX1080ti graphic card and an Intel i7-3820 processor. Four standard 4-step PSP fringe patterns were pre-stored in the projector and then projected sequentially. System calibration and geometric parameters were pre-calculated and stored on the GPU before measurement. All computations were performed on the GPU. Pixel-wise computation permitted parallel computing to achieve real-time motion-induced-error compensation during surface-shape measurement.

A moving manikin head was measured by the system. The measurement, including 3D reconstruction of a point cloud using motion-induced-error compensation and display, was performed in real-time with image capture. The reconstructed point cloud was displayed using OpenGL, with colours blue to red representing near to far (Figure 6.10). The mean GPU runtime of a single 3D measurement with motion-induced-error compensation was approximately 25 ms. The display rate (including 3D construction, data transfer, and rendering) achieved approximately 30 fps (In Figure 6.10, the number shown in the bottom-left corner is the current frame rate in fps).

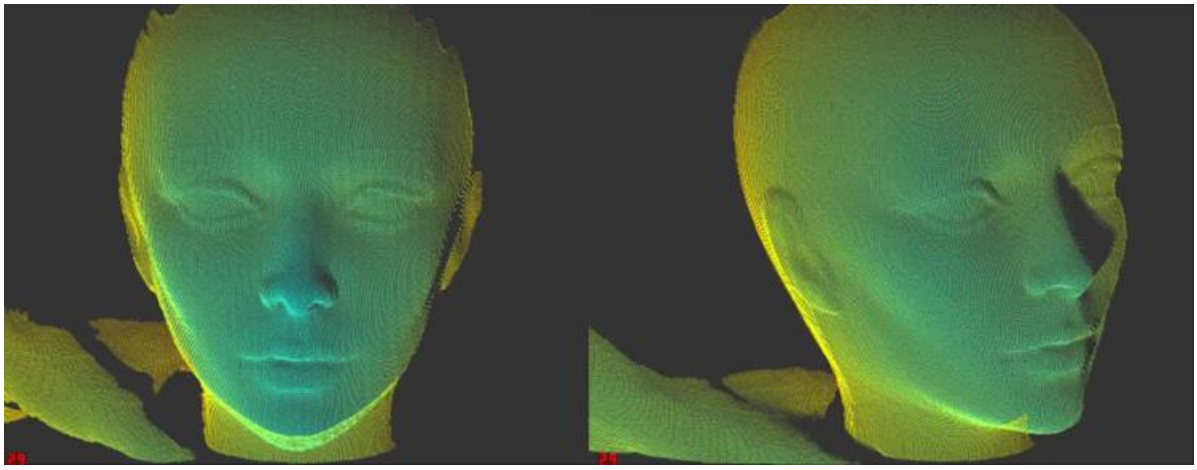

Figure 6.10. Real-time measurement result of a moving manikin head after motion-induced-error compensation.

A further measurement using real-time motion-induced-error compensation was performed on a deforming surface, a deflating balloon. The reconstructed 3D point cloud is displayed in Figure 6.11, with grayscale texture (Figure 6.11a) and with colours blue to red representing near to far (Figure 6.11b). The display rate slightly dropped to 25 fps, due to the additional rendering of the grayscale texture (Figure 6.11a). The measurement demonstrates that the error compensation method was effective even for real-time measurement with non-rigid body motion (non-uniform surface motion).

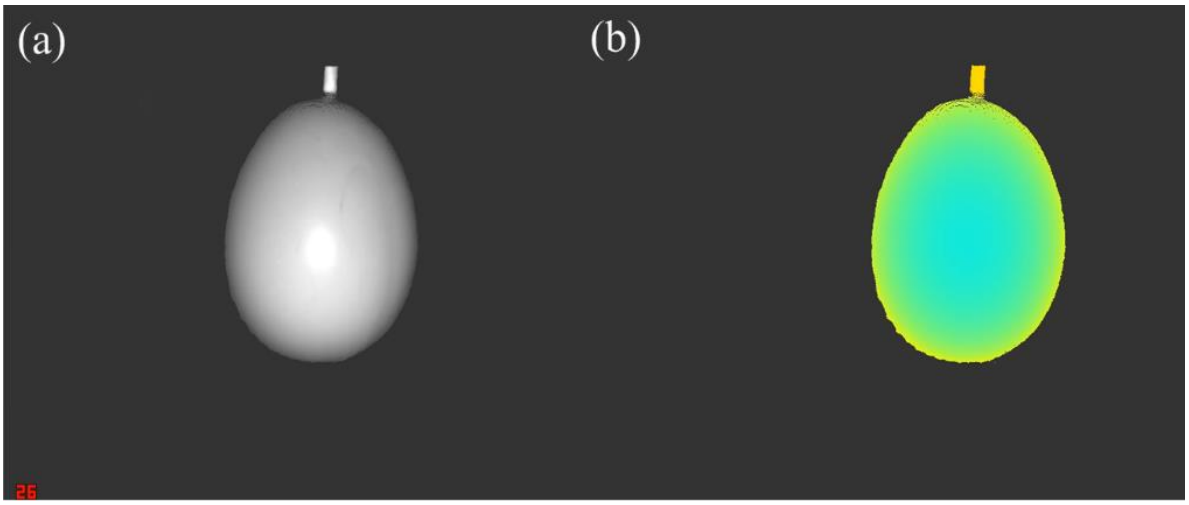

Figure 6.11. Real-time measurement result of a deflating balloon after motion-induced-error compensation: (a) with grayscale texture, and (b) with colours blue to red representing near to far.

The experimental results demonstrate the effectiveness of the new real-time motion-induced-error compensation method in 3D surface-shape measurement for objects with large depth variations and deforming surfaces.

6.3 Discussion

A new real-time motion-induced-error compensation method was developed for dynamic 3D surface-shape measurement. Three phase maps are computed over a multiple measurement sequence and the unknown phase shifts due to surface motion are estimated by calculating the differences between the computed phase maps. A phase map with reduced motion-

induced error is then computed while considering the estimated phase shift error. The method achieved higher measurement accuracy than the standard PSP and single-image FTP, reducing the motion artifact due to surface motion, while also handling measurement of surfaces with high depth variation. The motion-induced phase shift estimation and error compensation are performed pixel-wise, which enables parallel computing using a GPU to reduce the processing time for real-time measurement. Experiments demonstrated the ability of the method to reduce motion-induced error in real time, for shape measurement of surfaces with high depth variation, and moving and deforming surfaces. There is currently a limit to the speed of object motion or surface deformation that can be handled by the new method. Large motion-induced phase shift between successive captured images would cause motion-induced error that cannot be eliminated by error compensation. Future research may focus on real-time measurement of objects with fast motion, and non-constant acceleration.

Chapter 7
Contributions and Future Work

This chapter summarizes contributions of the thesis research and proposes future work. In this thesis, new techniques were developed to achieve high-accuracy, high-resolution, real-time 3D surface-shape measurement, using system geometry constraints. A method to compensate motion-induced phase error was developed for real-time 3D measurement.

7.1 Contributions

The main contributions of the research of this thesis are as follows:

1. Developed a new background and amplitude coded fringe pattern method using a single camera and single projector. The background and amplitude are combined as a codeword to identify the wrapped phase fringe order to partially unwrap the high-frequency phase map to a low frequency wrapped phase map. The low-frequency wrapped phase map is then directly used to reconstruct the surface based on system geometry constraints without using additional images. The application of background and amplitude code, and geometry constraints can uniquely determine the order of 48 phase periods; therefore, only four fringe patterns are required for one 3D measurement, and high frequency fringe patterns can be used to achieve high measurement accuracy.
2. Developed new background modulation fringe pattern methods for high-accuracy high-resolution real-time 3D surface-shape measurement:
    2.1. A four-image background modulation phase-shifting method was developed, where a simple background offset was added to denote each neighbouring odd and even phase period. The embedded background offset is independent of phase computation, and thus does not affect the accuracy of phase maps.
    2.2. A novel mathematical model that relates the fringe wavelength to system-geometry constraints was developed to determine the highest pattern frequency that allows only two corresponding-point candidates in the measurement volume for reliable

corresponding-point selection. Mathematical expressions of geometry-constraint parameters permit calculation of the parameters prior to measurement, thus permitting use of a stored LUT to reduce computational cost during the measurement.

2.3. An experimental system was developed consisting of two cameras and one DLP projector. A short left-camera-projector baseline was used to enable reliable corresponding-point selection without sacrificing fringe pattern frequency and the depth of the measurement volume. A new calibration method procedure was used to achieve accurate calibration of the two-camera single-projector experimental system, even with a short left-camera-projector baseline. Experiments demonstrated the ability of the method to perform full-field static 3D shape measurement with high-accuracy, for a surface with geometric discontinuity, and for spatially isolated objects.

2.4. A background-modulated modified FTP method was developed, which reduced the required number of fringe patterns to two for 3D surface reconstruction. A continuous measurement framework was developed for real-time 3D measurement. A real-time 3D measurement system was developed, which achieved a 3D display rate of 50 fps. Experiments demonstrated the ability of the method to perform dynamic 3D surface-shape measurement on moving and deforming surfaces.

3. A new real-time motion-induced-error compensation method was developed for the 4-step PSP method:

3.1. An approximation model of motion-induced phase error was developed, which showed the mathematical relation between the phase error, phase, and motion-induced phase shifts.

3.2. Non-iterative and pixel-wise estimation of the phase-shift due to surface motion was performed without the assumption of homogeneous motion across the surface. The

non-iterative method permits motion-induced-error compensation in real-time 3D measurement.

3.3. The motion-induced-error compensation method was applied on the developed real-time 3D measurement system using standard $\pi/2$ phase-shifted fringe patterns. The use of a very short baseline between the left camera and projector minimized the number of candidate positions in the measurement volume to a single candidate; thus, there is no need to embed additional information in the fringe patterns. Experiments demonstrated the ability of the method to reduce motion-induced error in real time, for shape measurement of surfaces with high depth variation, and moving and deforming surfaces.

Publications derived from this work are:

1. X. Liu and J. Kofman, "Background and amplitude encoded fringe patterns for 3D surface-shape measurement," Opt. Lasers Eng. **94**, 63-69 (2017).
2. X. Liu and J. Kofman, "High-frequency background modulation fringe patterns based on a fringe-wavelength geometry-constraint model for 3D surface-shape measurement," Opt. Express **25**(14), 16618-16628 (2017).
3. X. Liu and J. Kofman, "Real-time 3D surface-shape measurement using background-modulated modified Fourier transform profilometry with geometry-constraint," Opt. Lasers Eng. **115**, 217-224 (2019).
4. X. Liu, T. Tao, Y. Wan, and J. Kofman, "Real-time motion-induced-error compensation in 3D surface-shape measurement." Opt. Express **27**(18), 25265-25279 (2019).

Conferences:

1. X. Liu and J. Kofman, "Real-time 3D measurement using background-modulated modified Fourier transform profilometry," in *19th International Symposium on Optomechatronic Technology (ISOT)* (2018), pp. 124-125. (Invited talk)

2. J. Kofman and X. Liu, "Innovations in structured light methods and optical metrology," in *Optical Technology and Measurement for Industrial Applications*, *Optics and Photonics International Congress* (SPIE, 2019), pp. 31-32. (Invited talk)

7.2 Limitations and Future Work

1. For the techniques developed in this research using two cameras and one projector, the background intensity of the fringe patterns was modified to provide additional information for reliable selection of the corresponding point. The background intensity modification reduces the SNR of the phase-shifted patterns and requires four images to extract the embedded background pattern. Although applying a very short left-camera-projector baseline can further reduce the number of candidates in the measurement volume to one, the projector calibration becomes more error-prone, and the correspondence search is more sensitive to the calibration errors of the projector.

   Recommended future work would be to:

   - Develop new techniques using more system geometry constraints, which do not require additional information embedded in the fringe patterns, and which allow larger depth of measurement volume while still achieving reliable correspondence determination.

2. Motion-induced error still exists after applying the developed motion-induced error compensation method, if the object moves or deforms at a higher speed. The approximations in the developed methods do not hold for large motion-induced phase shift between successive captured images.

   Recommended future work would be to:

   - Use 6-bit or 7-bit fringe patterns rather than the current 8-bit patterns, to achieve faster fringe projection speed; thus, the motion-induced phase shift could be reduced.
   - Develop new methods to provide better estimation of motion-induced phase shifts and optimize the GPU program code to require only a few iterations (two or three

iterations) to further improve the accuracy of the estimated motion-induced phase shifts and the accuracy of the computed phase, while keeping a display rate of 25 fps.

3. Another problem with current 3D shape measurement methods is the requirement to use active lighting which might not be suitable for some applications, such as measuring human faces or in situations where visible light projection is not appropriate or desired. To extend 3D surface-shape measurement techniques to these applications and conditions, use of infrared (IR) light for pattern projection instead of visible light may potentially be a solution. A new active 3D surface-shape measurement technique using only non-visible light is still desirable and needed for high-accuracy real-time 3D measurement applications.

References

1. G. Sansoni and F. Docchio, "Three-dimensional optical measurements and reverse engineering for automotive applications," Robot. Comput. Integr. Manuf. **20**(5), 359–367 (2004).
2. K. Zhong, Z. Li, X. Zhou, Y. Li, Y. Shi, and C. Wang, "Enhanced phase measurement profilometry for industrial 3D inspection automation," Int. J. Adv. Manuf. Technol. **76**, 1563–1574 (2014).
3. M. Markovic, S. Dosen, C. Cipriani, D. Popovic, and D. Farina, "Stereovision and augmented reality for closed-loop control of grasping in hand prostheses," J. Neural Eng. **11**(4), 046001 (2014).
4. A. J. Das, T. A. Valdez, J. A. Vargas, P. Saksupapchon, P. Rachapudi, Z. Ge, J. C. Estrada, and R. Raskar, "Volume estimation of tonsil phantoms using an oral camera with 3D imaging," Biomed. Opt. Express **7**(4), 1445–1457 (2016).
5. J. A. Beraldin, M. Picard, S. F. El-hakim, G. Godin, V. Valzano, and A. Bandiera, "Combining 3D technologies for cultural heritage interpretation and entertainment," Proc. SPIE, Videometrics VIII **5665**, 108–118 (2005).
6. A. Geiger, M. Roser, and R. Urtasun, "Efficient large-scale stereo matching," in *Asian Conference on Computer Vision* (2010), pp. 25–38.
7. R. Usamentiaga, J. Molleda, and D. F. García, "Fast and robust laser stripe extraction for 3D reconstruction in industrial environments," Mach. Vis. Appl. **23**(1), 179–196 (2012).
8. S. Son, H. Park, and K. H. Lee, "Automated laser scanning system for reverse engineering and inspection," Int. J. Mach. Tools Manuf. **42**(8), 889–897 (2002).
9. J. Kofman and K. Borribanbunpotkat, "Hand-held 3D scanner for surface-shape measurement without sensor pose tracking or surface markers," Virtual Phys. Prototyp. **9**(2), 81–95 (2014).
10. C. Rocchini, P. Cignoni, C. Montani, P. Pingi, and R. Scopigno, "A low cost 3D scanner based on structured light," Comput. Graph. Forum **20**(3), 299–308 (2001).
11. J. Geng, "Structured-light 3D surface imaging: a tutorial," Adv. Opt. Photonics **3**, 128–160 (2011).
12. Y. Wang and S. Zhang, "Comparison of the squared binary, sinusoidal pulse width modulation, and optimal pulse width modulation methods for three-dimensional shape measurement with projector defocusing," Appl. Opt. **51**(7), 861–72 (2012).
13. J. Yao, Y. Tang, and J. Chen, "Three-dimensional shape measurement with an arbitrarily arranged projection moiré system," Opt. Lett. **41**(4), 717 (2016).
14. P. Smith Neto and G. C. Coelho, "The Shadow Moiré method using the phase shifting

technique and digital image processing: computational implementation and application to the 3D-reconstruction of a buckled plate," J. Brazilian Soc. Mech. Sci. **22**(3), 399–409 (2000).

15. F. Mohammadi and J. Kofman, "Single-frame digital phase-shifting 3D shape measurement using pixel-wise moiré-wavelength refinement," Opt. Lasers Eng. **78**, 196–204 (2016).
16. F. Mohammadi and J. Kofman, "Improved grid-noise removal in single-frame digital moiré 3D shape measurement," Opt. Lasers Eng. **86**, 143–155 (2016).
17. F. Mohammadi and J. Kofman, "Multi-wavelength digital-phase-shifting moiré based on moiré wavelength," Appl. Sci. **9**(9), 1917 (2019).
18. C. Waddington and J. Kofman, "Modified sinusoidal fringe-pattern projection for variable illuminance in phase-shifting three-dimensional surface-shape metrology," Opt. Eng. **53**(8), 084109–9 (2014).
19. P. Jia, J. Kofman, and C. English, "Two-step triangular-pattern phase-shifting method for three-dimensional object-shape measurement," Opt. Eng. **46**(8), 083201 (2007).
20. G. Rajshekhar and P. Rastogi, "Fringe analysis: Premise and perspectives," Opt. Lasers Eng. **50**(8), iii–x (2012).
21. M. Takeda and K. Mutoh, "Fourier transform profilometry for the automatic measurement of 3-D object shapes," Appl. Opt. **22**(24), 3977–3982 (1983).
22. F. Da and F. Dong, "Windowed Fourier transform profilometry based on improved S-transform," Opt. Lett. **37**(17), 3561 (2012).
23. Q. Kemao, "Applications of windowed Fourier fringe analysis in optical measurement: A review," Opt. Lasers Eng. **66**, 67–73 (2015).
24. L. R. Watkins, "Review of fringe pattern phase recovery using the 1-D and 2-D continuous wavelet transforms," Opt. Lasers Eng. **50**(8), 1015–1022 (2012).
25. C. Jiang, S. Jia, J. Dong, Q. Lian, and D. Li, "Multi-frequency fringe projection profilometry based on wavelet transform," Opt. Express **24**(11), 11323–11333 (2016).
26. J. Li, X. Su, and L. Guo, "Improved Fourier transform profilometry for the automatic measurement of three-dimensional object shapes," Opt. Eng. **29**(12), 1439–1444 (1990).
27. S. Zhang, "Phase unwrapping error reduction framework for a multiple-wavelength phase-shifting algorithm," Opt. Eng. **48**(10), 105601 (2009).
28. P. S. Huang, S. Zhang, and F.-P. Chiang, "Trapezoidal phase-shifting method for three-dimensional shape measurement," Opt. Eng. **44**(12), 123601 (2005).
29. P. Jia, J. Kofman, and C. English, "Intensity-ratio error compensation for triangular-pattern phase-shifting profilometry," J. Opt. Soc. Am. A **24**(10), 3150 (2007).
30. K. Liu, Y. Wang, D. L. Lau, Q. Hao, and L. G. Hassebrook, "Gamma model and its

analysis for phase measuring profilometry," J. Opt. Soc. Am. A **27**(3), 553–62 (2010).

31. Q. Zhang, X. Su, L. Xiang, and X. Sun, "3-D shape measurement based on complementary Gray-code light," Opt. Lasers Eng. **50**(4), 574–579 (2012).

32. A. Asundi and Z. Wensen, "Fast phase-unwrapping algorithm based on a gray-scale mask and flood fill," Appl. Opt. **37**(23), 5416–5420 (1998).

33. Y. Xu, S. Jia, Q. Bao, H. Chen, and J. Yang, "Recovery of absolute height from wrapped phase maps for fringe projection profilometry," Opt. Express **22**(14), 16819–16828 (2014).

34. J. Meneses, D. Amaya, and Z. Valderrama, "3D reconstruction of complicated objects by gray code method," in *5th Iberoamerican Meeting on Optics and 8th Latin American Meeting on Optics, Lasers, and Their Applications* (2004), **5622**, pp. 1316–1321.

35. C. Reich, R. Ritter, and J. Thesing, "White light heterodyne principle for 3D-measurement," Lasers Opt. Manuf. III **3100**, 236–244 (1997).

36. Y. Ding, J. Xi, Y. Yu, W. Cheng, S. Wang, and J. F. Chicharo, "Frequency selection in absolute phase maps recovery with two frequency projection fringes," Opt. Express **20**(12), 13238 (2012).

37. J. Long, J. Xi, M. Zhu, W. Cheng, R. Cheng, Z. Li, and Y. Shi, "Absolute phase map recovery of two fringe patterns with flexible selection of fringe wavelengths," Appl. Opt. **53**(9), 1794 (2014).

38. J. Song, D. L. Lau, Y.-S. Ho, and K. Liu, "Automatic look-up table based real-time phase unwrapping for phase measuring profilometry and optimal reference frequency selection," Opt. Express **27**(9), 13357 (2019).

39. K. Zhong, Z. Li, Y. Shi, C. Wang, and Y. Lei, "Fast phase measurement profilometry for arbitrary shape objects without phase unwrapping," Opt. Lasers Eng. **51**(11), 1213–1222 (2013).

40. C. Zuo, L. Huang, M. Zhang, Q. Chen, and A. Asundi, "Temporal phase unwrapping algorithms for fringe projection profilometry: A comparative review," Opt. Lasers Eng. **85**, 84–103 (2016).

41. H. Zhao, Y. Xu, H. Jiang, X. Diao, C. Liu, and M. Xing, "Real-time 3D shape measurement by fringe projection and GPU parallel computing," in *Tenth International Symposium on Precision Engineering Measurements and Instrumentation* (2019), **11053**, p. 148.

42. N. Pears, Y. Liu, and P. Bunting, *3D Imaging, Analysis and Applications* (Springer, 2012).

43. Y. Zhang, Z. Xiong, and F. Wu, "Unambiguous 3D measurement from speckle-embedded fringe," Appl. Opt. **52**(32), 7797–805 (2013).

44. S. Gai, F. Da, and X. Dai, "Novel 3D measurement system based on speckle and fringe pattern projection," Opt. Express **24**(16), 17686–17697 (2016).

45. T. Tao, Q. Chen, J. Da, S. Feng, Y. Hu, and C. Zuo, "Real-time 3-D shape measurement with composite phase-shifting fringes and multi-view system," Opt. Express **24**(18), 20253–20269 (2016).

46. W. Hwu, *GPU Computing Gems* (Morgan Kaufmann, 2012).

47. S. Van der Jeught and J. J. J. Dirckx, "Real-time structured light profilometry: a review," Opt. Lasers Eng. **87**, 18–31 (2016).

48. W.-S. Zhou and X.-Y. Su, "A direct mapping algorithm for phase-measuring profilometry," J. Mod. Opt. **41**(1), 89–94 (1994).

49. P. Jia, J. Kofman, and C. English, "Comparison of linear and nonlinear calibration methods for phase-measuring profilometry," Opt. Eng. **46**(4), 043601 (2007).

50. Z. Zhang, C. E. Towers, and D. P. Towers, "Uneven fringe projection for efficient calibration in high-resolution 3D shape metrology," Appl. Opt. **46**(24), 6113–6119 (2007).

51. Q. Hu, P. S. Huang, Q. Fu, and F.-P. Chiang, "Calibration of a three-dimensional shape measurement system," Opt. Eng. **42**(2), 487 (2003).

52. S. Zhang and P. S. Huang, "Novel method for structured light system calibration," Opt. Eng. **45**(8), 083601 (2006).

53. J. Heikkila and O. Silven, "A four-step camera calibration procedure with implicit image correction," in *Proceedings of IEEE Computer Society Conference on Computer Vision and Pattern Recognition* (1997), pp. 1106–1112.

54. M. A. A. Sid-Ahmed and M. T. Boraie, "Dual camera calibration for 3-D machine vision metrology," IEEE Trans. Instrum. Meas. **39**(3), 512–516 (1990).

55. Z. Zhang, "Flexible camera calibration by viewing a plane from unknown orientations," in *Proceedings of the Seventh IEEE International Conference on Computer Vision* (IEEE, 1999), pp. 666–673.

56. M. Bevilacqua, G. Di Leo, M. Landi, C. Liguori, V. Paciello, A. Paolillo, and A. Pietrosanto, "A flexible stereo calibration for a structured-light profilometer," in *IEEE International Conference on Industrial Technology* (2013), pp. 1026–1031.

57. C. Bräuer-Burchardt, P. Kühmstedt, and G. Notni, "Code minimization for fringe projection based 3D stereo sensors by calibration improvement," in *The 38th Annual Workshop of the Austrian Association for Pattern Recognition* (2014), pp. 1–8.

58. M. Vo, Z. Wang, T. Hoang, and D. Nguyen, "Flexible calibration technique for fringe-projection-based three-dimensional imaging," Opt. Lett. **35**(15), 3192–3194 (2010).

59. W. Zhang, W. Li, L. Yu, H. Luo, H. Zhao, and H. Xia, "Sub-pixel projector calibration method for fringe projection profilometry," Opt. Express **25**(16), 19158 (2017).

60. J. Zhu, X. Su, Z. You, and Y. Liu, "Temporal-spatial encoding binary fringes toward three-dimensional shape measurement without projector nonlinearity," Opt. Eng. **54**(5), 054108 (2015).

61. R. J. Valkenburg and A. M. McIvor, "Accurate 3D measurement using a structured light system," Image Vis. Comput. **16**(2), 99–110 (1998).

62. R. Porras-Aguilar, K. Falaggis, and R. Ramos-Garcia, "Optimum projection pattern generation for grey-level coded structured light illumination systems," Opt. Lasers Eng. **91**, 242–256 (2017).

63. S. Gai and F. Da, "Fringe image analysis based on the amplitude modulation method," Opt. Express **18**(10), 10704–10719 (2010).

64. Y. Wang and S. Zhang, "Novel phase-coding method for absolute phase retrieval," Opt. Lett. **37**(11), 2067–2069 (2012).

65. Y. Xing, C. Quan, and C. J. Tay, "A modified phase-coding method for absolute phase retrieval," Opt. Lasers Eng. **87**, 97–102 (2016).

66. D. Zheng and F. Da, "Phase coding method for absolute phase retrieval with a large number of codewords," Opt. Express **20**(22), 24139–50 (2012).

67. S. Heist, A. Mann, P. Kühmstedt, P. Schreiber, and G. Notni, "Array projection of aperiodic sinusoidal fringes for high-speed three-dimensional shape measurement," Opt. Eng. **53**(11), 112208 (2014).

68. W. Lohry, V. Chen, and S. Zhang, "Absolute three-dimensional shape measurement using coded fringe patterns without phase unwrapping or projector calibration," Opt. Express **22**(2), 1287–1301 (2014).

69. W. Su, C. Kuo, and F. Kao, "Three-dimensional trace measurements for fast-moving objects using binary-encoded fringe projection techniques," Appl. Opt. **53**(24), 5283–5289 (2014).

70. Y. Long, S. Wang, W. Wu, X. Yang, G. Jeon, and K. Liu, "Hybrid coding strategy for SNR improvement in 3-step phase measuring profilometry," in *2015 IEEE China Summit and International Conference on Signal and Information Processing (ChinaSIP)* (2015), pp. 500–504.

71. C. Guan, L. G. Hassebrook, and D. L. Lau, "Composite structured light pattern for three-dimensional video," Opt. Express **11**(5), 406–417 (2003).

72. C. A. García-Isáis and N. A. Ochoa, "One shot profilometry using a composite fringe pattern," Opt. Lasers Eng. **53**, 25–30 (2014).

73. K. Peng, Y. Cao, Y. Wu, C. Chen, and Y. Wan, "A dual-frequency online PMP method with phase-shifting parallel to moving direction of measured object," Opt. Commun. **383**, 491–499 (2017).

74. W.-H. Su and S.-Y. Chen, "One shot projected fringe profilometry using a 2D fringe-

encoded pattern," in *Photonic Fiber and Crystal Devices: Advances in Materials and Innovations in Device Applications XII* (2018), **10755**, p. 38.

75. C. Zuo, Q. Chen, G. Gu, S. Feng, and F. Feng, "High-speed three-dimensional profilometry for multiply objects with complex shapes," Opt. Express **20**(17), 19493 (2012).

76. S. Zhang, "Composite phase-shifting algorithm for absolute phase measurement," Opt. Lasers Eng. **50**(11), 1538–1541 (2012).

77. J. L. Flores, J. A. Ferrari, G. García Torales, R. Legarda-Saenz, and A. Silva, "Color-fringe pattern profilometry using a generalized phase-shifting algorithm," Appl. Opt. **54**(30), 8827 (2015).

78. H. J. Chen, J. Zhang, D. J. Lv, and J. Fang, "3-D shape measurement by composite pattern projection and hybrid processing," Opt. Express **15**(19), 12318–12330 (2007).

79. H. Zou, X. Zhou, H. Zhao, T. Yang, H. Du, F. Gu, and Z. Zhao, "Color fringe-projected technique for measuring dynamic objects based on bidimensional empirical mode decomposition," Appl. Opt. **51**(16), 3622–3630 (2012).

80. L. Rao and F. Da, "Neural network based color decoupling technique for color fringe profilometry," Opt. Laser Technol. **70**, 17–25 (2015).

81. K. Song, S. Hu, X. Wen, and Y. Yan, "Fast 3D shape measurement using Fourier transform profilometry without phase unwrapping," Opt. Lasers Eng. **84**, 74–81 (2016).

82. E.-H. Kim, J. Hahn, H. Kim, and B. Lee, "Profilometry without phase unwrapping using multi-frequency and four-step phase-shift sinusoidal fringe projection," Opt. Express **17**(10), 7818–30 (2009).

83. L. Yong, "A correspondence finding method based on space conversion in 3D shape measurement using fringe projection," Opt. Express **23**(11), 14188 (2015).

84. Y. An, J.-S. Hyun, and S. Zhang, "Pixel-wise absolute phase unwrapping using geometric constraints of structured light system," Opt. Express **24**(16), 18445–18459 (2016).

85. C. Jiang, B. Li, and S. Zhang, "Pixel-by-pixel absolute phase retrieval using three phase-shifted fringe patterns without markers," Opt. Lasers Eng. **91**, 232–241 (2017).

86. J. Dai, Y. An, and S. Zhang, "Absolute three-dimensional shape measurement with a known object," Opt. Express **25**(9), 10384 (2017).

87. T. Tao, Q. Chen, S. Feng, Y. Hu, J. Da, and C. Zuo, "High-precision real-time 3D shape measurement using a bi-frequency scheme and multi-view system," Appl. Opt. **56**(13), 3646–3653 (2017).

88. X. Yang, C. Zeng, J. Luo, Y. Lei, B. Tao, and X. Chen, "Absolute phase retrieval using one coded pattern and geometric constraints of fringe projection system," Appl.

Sci. **8**(12), 2673 (2018).

89. T. Tao, Q. Chen, S. Feng, Y. Hu, M. Zhang, and C. Zuo, "High-precision real-time 3D shape measurement based on a quad-camera system," J. Opt. **20**, 014009 (2018).

90. T. Tao, Q. Chen, S. Feng, J. Qian, Y. Hu, L. Huang, and C. Zuo, "High-speed real-time 3D shape measurement based on adaptive depth constraint," Opt. Express **26**(17), 22440 (2018).

91. C. Bräuer-Burchardt, M. Möller, C. Munkelt, M. Heinze, P. Kühmstedt, and G. Notni, "On the accuracy of point correspondence methods in three-dimensional measurement systems using fringe projection," Opt. Eng. **52**(6), 063601 (2013).

92. C. Bräuer-Burchardt, P. Kühmstedt, and G. Notni, "Phase unwrapping using geometric constraints for high-speed fringe projection based 3D measurements," in *Modeling Aspects in Optical Metrology IV* (2013), **8789**, p. 878906.

93. C. Bräuer-Burchardt, A. Breitbarth, P. Kühmstedt, and G. Notni, "High-speed three-dimensional measurements with a fringe projection-based optical sensor," Opt. Eng. **53**(11), 112213 (2014).

94. C. Zuo, T. Tao, S. Feng, L. Huang, A. Asundi, and Q. Chen, "Micro Fourier transform profilometry (μFTP): 3D shape measurement at 10,000 frames per second," Opt. Lasers Eng. **102**, 70–91 (2018).

95. S. Heist, P. Lutzke, I. Schmidt, P. Dietrich, P. Kühmstedt, A. Tünnermann, and G. Notni, "High-speed three-dimensional shape measurement using GOBO projection," Opt. Lasers Eng. **87**, 90–96 (2016).

96. J.-S. Hyun and S. Zhang, "High-speed 3D surface measurement with mechanical projector," in *Dimensional Optical Metrology and Inspection for Practical Applications VI* (2017), p. 1022004.

97. J.-S. Hyun, B. Li, and S. Zhang, "High-speed high-accuracy three-dimensional shape measurement using digital binary defocusing method versus sinusoidal method," Opt. Eng. **56**(7), 074102 (2017).

98. J. Dai, B. Li, and S. Zhang, "High-quality fringe pattern generation using binary pattern optimization through symmetry and periodicity," Opt. Lasers Eng. **52**(1), 195–200 (2014).

99. S. Zhang and S.-T. Yau, "High-speed three-dimensional shape measurement system using a modified two-plus-one phase-shifting algorithm," Opt. Eng. **46**(11), 113603 (2007).

100. H. Nguyen, D. Nguyen, Z. Wang, H. Kieu, and M. Le, "Real-time, high-accuracy 3D imaging and shape measurement," Appl. Opt. **54**(1), A9 (2014).

101. M. van de Giessen, J. P. Angelo, and S. Gioux, "Real-time, profile-corrected single snapshot imaging of optical properties," Biomed. Opt. Express **6**(10), 4051 (2015).

102. F. Lu, C. Wu, and J. Yang, "High-speed 3D shape measurement using Fourier transform and stereo vision," J. Eur. Opt. Soc. Publ. **14**(1), 22 (2018).

103. K. Liu, Y. Wang, D. L. Lau, Q. Hao, and L. G. Hassebrook, "Dual-frequency pattern scheme for high-speed 3-D shape measurement," Opt. Express **18**(5), 5229–5244 (2010).

104. H. Yun, B. Li, and S. Zhang, "Pixel-by-pixel absolute three-dimensional shape measurement with modified Fourier transform profilometry," Appl. Opt. **56**(5), 1472–1480 (2017).

105. L. Lu, J. Xi, Y. Yu, and Q. Guo, "New approach to improve the accuracy of 3-D shape measurement of moving object using phase shifting profilometry," Opt. Express **21**(25), 30610 (2013).

106. L. Lu, J. Xi, Y. Yu, and Q. Guo, "New approach to improve the performance of fringe pattern profilometry using multiple triangular patterns for the measurement of objects in motion," Opt. Eng. **53**(11), 112211 (2014).

107. L. Lu, Y. Ding, Y. Luan, Y. Yin, Q. Liu, and J. Xi, "Automated approach for the surface profile measurement of moving objects based on PSP," Opt. Express **25**(25), 32120 (2017).

108. D. L. Lau, K. Liu, and L. G. Hassebrook, "Real-time three-dimensional shape measurement of moving objects without edge errors by time-synchronized structured illumination," Opt. Lett. **35**(14), 2487 (2010).

109. S. Feng, C. Zuo, T. Tao, Y. Hu, M. Zhang, Q. Chen, and G. Gu, "Robust dynamic 3-D measurements with motion-compensated phase-shifting profilometry," Opt. Lasers Eng. **103**, 127–138 (2018).

110. P. Cong, Z. Xiong, Y. Zhang, S. Zhao, and F. Wu, "Accurate dynamic 3D sensing with Fourier-assisted phase shifting," IEEE J. Sel. Top. Signal Process. **9**(3), 396–408 (2015).

111. J. Qian, T. Tao, S. Feng, Q. Chen, and C. Zuo, "Motion-artifact-free dynamic 3D shape measurement with hybrid Fourier-transform phase-shifting profilometry," Opt. Express **27**(3), 2713 (2019).

112. Y. Wang, Z. Liu, C. Jiang, and S. Zhang, "Motion induced phase error reduction using a Hilbert transform," Opt. Express **26**(26), 34224 (2018).

113. H. Chen, Y. Yin, Z. Cai, W. Xu, X. Liu, X. Meng, and X. Peng, "Suppression of the nonlinear phase error in phase shifting profilometry: considering non-smooth reflectivity and fractional period," Opt. Express **26**(10), 13489 (2018).

114. Z. Liu, P. C. Zibley, and S. Zhang, "Motion-induced error compensation for phase shifting profilometry," Opt. Express **26**(10), 12632 (2018).

115. L. Lu, Y. Yin, Z. Su, X. Ren, Y. Luan, and J. Xi, "General model for phase shifting profilometry with an object in motion," Appl. Opt. **57**(36), 10364 (2018).

116. Z. Li, "Accurate calibration method for a structured light system," Opt. Eng. **47**(5), 053604 (2008).

117. C. Waddington and J. Kofman, "Camera-independent saturation avoidance in measuring high-reflectivity-variation surfaces using pixel-wise composed images from projected patterns of different maximum gray level," Opt. Commun. **333**, 32–37 (2014).

118. S. Zhang and S.-T. Yau, "High dynamic range scanning technique," Opt. Eng. **48**(3), 033604 (2009).

119. C. Waddington and J. Kofman, "Modified sinusoidal fringe-pattern projection for variable illuminance in phase-shifting three-dimensional surface-shape metrology," Opt. Eng. **53**(8), 084109 (2014).

120. D. Li and J. Kofman, "Adaptive fringe-pattern projection for image saturation avoidance in 3D surface-shape measurement," Opt. Express **22**(8), 9887 (2014).

121. P. Viola and M. J. Jones, "Robust real-time object detection," Int. J. Comput. Vis. **57**(2), 137–154 (2001).

122. S. Zhang, X. Li, and S.-T. Yau, "Multilevel quality-guided phase unwrapping algorithm for real-time three-dimensional shape reconstruction," Appl. Opt. **46**(1), 50–57 (2007).

Appendix A

Derivation of the Equation of the Projector Epipolar Line and Computation of Epipolar-Line Parameters

This appendix details the derivation of the equation of the projector epipolar line (Eq. (4.11)) and computation of the epipolar-line parameters. The projection of any 3D world point coordinates (X^w, Y^w, Z^w) to the projector normalized image plane can be computed by Eq. (4.9). The epipolar line on the projector image plane is a straight line, therefore the equation of the epipolar line can be obtained by computing the coordinates of two points on the epipolar line. Taking two points (X_1^w, Y_1^w, Z_1^w) and (X_2^w, Y_2^w, Z_2^w), where $Z_1^w = 0$ and $Z_2^w = z$, by inserting the coordinates into Eq. (4.9), the projections on the projector normalized image plane can be written as:

$$\begin{bmatrix} x_{n1}^p \\ y_{n1}^p \end{bmatrix} = \begin{bmatrix} \dfrac{p_0}{s_0} \\ \dfrac{q_0}{s_0} \end{bmatrix}, \tag{A.1}$$

$$\begin{bmatrix} x_{n2}^p \\ y_{n2}^p \end{bmatrix} = \begin{bmatrix} \dfrac{p_1 z + p_0}{s_1 z + s_0} \\ \dfrac{q_1 z + q_0}{s_1 z + s_0} \end{bmatrix}, \tag{A.2}$$

where parameters p_0, p_1, q_0, q_1, s_0, s_1 are described in Eq. (4.10). The projections (x_{n1}^p, y_{n1}^p) and (x_{n2}^p, y_{n2}^p) are located on the epipolar line. The equation of the epipolar line can be written as:

$$y_n^p = m^p x_n^p + c^p, \tag{A.3}$$

where m^p and c^p can be computed as:

$$m^p = \frac{y_{n2}^p - y_{n1}^p}{x_{n2}^p - x_{n1}^p} = \frac{(q_1 z + q_0) s_0 - (s_1 z + s_0) q_0}{(p_1 z + p_0) s_0 - (s_1 z + s_0) p_0} = \frac{q_1 s_0 - q_0 s_1}{p_1 s_0 - p_0 s_1}, \tag{A.4}$$

$$c^p = y_{n1}^p - m^p x_{n1}^p = \frac{p_1 q_0 - p_0 q_1}{p_1 s_0 - p_0 s_1}. \tag{A.5}$$

Thus, the equation of the projector epipolar line can be expressed by Eq. (4.11).

In practice, the projector-image pixel coordinates (u^p, v^p) are used for the corresponding-point search on the epipolar line. (u^p, v^p) can be computed from (x_n^p, y_n^p) using Eq. (4.12). Therefore, the equation of the epipolar line can be rewritten as:

$$v^p = \breve{m}^p u^p + \breve{c}^p, \tag{A.6}$$

where:

$$\breve{m}^p = \left(\frac{f_v^p}{f_u^p} \right) \left(\frac{q_1 s_0 - q_0 s_1}{p_1 s_0 - p_0 s_1} \right), \tag{A.7}$$

$$\breve{c}^p = \left(\frac{f_v^p}{f_u^p} \right) \left[\frac{(p_1 q_0 - p_0 q_1) f_u^p + (q_0 s_1 - q_1 s_0) u_0^p}{p_1 s_0 - p_0 s_1} \right] + v_0^p. \tag{A.8}$$

The parameters $\breve{m}^p$, $\breve{c}^p$ can be pre-calculated for each line of sight before measurement and saved in a LUT. Similarly, the parameters of the right-camera epipolar line can be pre-calculated and saved.

Appendix B
Derivation of Motion-Induced Phase Error

This appendix details the derivation of the motion-induced phase error. The wrapped phase $\phi'(x, y)$ computed by the standard 4-step phase-shifting method can be expressed by Eq. (6.8). Inserting the intensities of the 4-step phase-shifted fringe images considering object motion (Eq. (6.7)) into Eq. (6.8) gives:

$$\begin{aligned}\phi'(x,y) &= \tan^{-1}\left[\frac{\cos\left(\phi-\pi/2-\varepsilon_2/2\right)-\cos\left(\phi-3\pi/2+\varepsilon_2/2+\varepsilon_3\right)}{\cos\left(\phi-\varepsilon_2/2-\varepsilon_1\right)-\cos\left(\phi-\pi+\varepsilon_2/2\right)}\right] \\ &= \tan^{-1}\left[\frac{\sin\left(\phi-\varepsilon_2/2\right)+\sin\left(\phi+\varepsilon_2/2+\varepsilon_3\right)}{\cos\left(\phi-\varepsilon_2/2-\varepsilon_1\right)+\cos\left(\phi+\varepsilon_2/2\right)}\right].\end{aligned} \tag{B.1}$$

For a very small phase-shift error ε, $\sin(\varepsilon) \approx \varepsilon$ and $\cos(\varepsilon) \approx 1$. The following approximation can be made:

$$\sin\left(\phi-\frac{\varepsilon_2}{2}\right) \approx \sin\phi-\frac{\varepsilon_2}{2}\cos\phi\,, \tag{B.2}$$

$$\sin\left(\phi+\frac{\varepsilon_2}{2}+\varepsilon_3\right) \approx \sin\phi+\left(\frac{\varepsilon_2}{2}+\varepsilon_3\right)\cos\phi\,, \tag{B.3}$$

$$\cos\left(\phi-\frac{\varepsilon_2}{2}-\varepsilon_1\right) \approx \cos\phi+\left(\frac{\varepsilon_2}{2}+\varepsilon_1\right)\sin\phi\,, \tag{B.4}$$

$$\cos\left(\phi+\frac{\varepsilon_2}{2}\right) \approx \cos\phi-\frac{\varepsilon_2}{2}\sin\phi\,. \tag{B.5}$$

Thus, Eq. (B.1) can be approximated as:

$$\phi'(x,y) \approx \tan^{-1}\left[\frac{2\sin\phi+\varepsilon_3\cos\phi}{2\cos\phi+\varepsilon_1\sin\phi}\right]. \tag{B.6}$$

The following equations can be derived:

$$\tan\phi'\tan\phi = \frac{2\sin^2\phi + \varepsilon_3 \sin\phi\cos\phi}{2\cos^2\phi + \varepsilon_1 \sin\phi\cos\phi}, \tag{B.7}$$

$$\tan\Delta\phi = \tan\left(\phi' - \phi\right) = \frac{\tan\phi' - \tan\phi}{1 + \tan\phi'\tan\phi} = \frac{\varepsilon_3\cos^2\phi - \varepsilon_1\sin^2\phi}{2 + \left(\varepsilon_1 + \varepsilon_3\right)\sin\phi\cos\phi}. \tag{B.8}$$

Thus, the motion-induced phase error $\Delta\phi$ can be expressed as:

$$\Delta\phi = \tan^{-1}\left[\frac{\varepsilon_3\cos^2\phi - \varepsilon_1\sin^2\phi}{2 + \left(\varepsilon_1 + \varepsilon_3\right)\sin\phi\cos\phi}\right]. \tag{B.9}$$

The motion-induced phase error $\Delta\phi$ can be considered as a function of phase-shift errors ε_1 and ε_3, $f(\varepsilon_1, \varepsilon_3)$. Using the first two terms of the Taylor series expansion of $f(\varepsilon_1, \varepsilon_3)$ centreed at $\varepsilon_1 = 0$, $\varepsilon_3 = 0$ to approximate $\Delta\phi$ gives the following expression:

$$\begin{aligned}\Delta\phi &\approx f\left(0,0\right) + \left[\varepsilon_1\frac{\partial f\left(0,0\right)}{\partial\varepsilon_1} + \varepsilon_3\frac{\partial f\left(0,0\right)}{\partial\varepsilon_3}\right] \\ &= -\frac{\varepsilon_1}{2}\sin^2\phi + \frac{\varepsilon_3}{2}\cos^2\phi \\ &= \frac{\varepsilon_3 - \varepsilon_1}{4} + \frac{\varepsilon_3 + \varepsilon_1}{4}\cos 2\phi.\end{aligned} \tag{B.10}$$